

DYNAMICS OF RIVER-SEDIMENT DELIVERY AND TURBIDITY CURRENT
FLOW OBSERVED IN LILLOOET LAKE, BRITISH COLUMBIA

A Thesis

Submitted to the Faculty of Graduate Studies and Research

In Partial Fulfillment of the Requirements

For the Degree of

Special Case Master of Science

in

Geography

University of Regina

By

Duncan Shayne MacDonald

Regina, Saskatchewan

April, 2019

Copyright 2019: D.S. MacDonald

UNIVERSITY OF REGINA
FACULTY OF GRADUATE STUDIES AND RESEARCH
SUPERVISORY AND EXAMINING COMMITTEE

Duncan Shayne MacDonald, candidate for the degree of Special Case Master of Science in Geography, has presented a thesis titled, ***Dynamics of River-Sediment Delivery and Turbidity Current Flow Observed in Lillooet Lake, British Columbia***, in an oral examination held on April 11, 2019. The following committee members have found the thesis acceptable in form and content, and that the candidate demonstrated satisfactory knowledge of the subject material.

External Examiner:	*Dr. Michael Märker, University of Pavia
Supervisor:	Dr. Kyle Hodder, Department of Geography and Environmental Studies
Committee Member:	Dr. Ulrike Hardenbicker, Department of Geography and Environmental Studies
Committee Member:	Dr. Maria Velez-Caicedo, Department of Geology
Chair of Defense:	Dr. Mark Vanderwel, Department of Biology

*via SKYPE



Lillooet-Green River delta, December 1968. Source: R. Gilbert, 1973. Original source: BCFS Photo 17140.



Lillooet-Green River delta, June 2015. Source: Google Earth Pro V. 7.3.2.5491. [June 07, 2015]. Lillooet-Green River delta.

Abstract

A study linking sediment-discharge dynamics and lake-bottom properties to plunging river flow was undertaken at Lillooet Lake, British Columbia. This study was initiated to understand the dynamics of turbidity currents that plunge off the front of the Lillooet-Green River delta and how those factors have an influence on turbidity current development. Understanding how turbidity currents behave is important to understanding the sedimentary budget and hydrology of lakes and reservoirs. To achieve the objectives of understanding how sediment-discharge dynamics and lake-bottom properties influence the development of turbidity currents in Lillooet Lake, field monitoring was undertaken for 10 days in July 2015. Field monitoring consisted of monitoring river stage (discharge), river temperature, and suspended sediment concentration as well as monitoring lake currents using an aDcp and a moored lake-temperature array. Water profiles were taken along the front of the delta. Changes to the subaqueous delta were monitored using single-beam sonar and the surface of the delta was monitored using an Unmanned Aerial Vehicle.

During this study, record-low discharge and lake levels were encountered which had a detrimental effect on monitoring flow properties. The resultant analysis provided several key observations based on the data collected during this study, given these conditions. (1) The fluvial sediment-discharge relationship had negative hysteresis, possibly due to the decoupled nature of the sources of sediment and meltwater in Lillooet-Green River. (2) The lower boundary of turbidity current showed pulsating velocity through time, thought to be the result of shearing at the boundary between the current and ambient lake water. (3) A benthic trough was observed in front of the plunge

line lobe that is believed to be a path for preferential flow as well as an eroded surface from turbidity currents originating from Lillooet-Green River delta.

The findings indicate that even at low-flows the sediment laden water plunging off the Lillooet-Green River delta can produce interflows and underflows described as turbidity currents. Plunging water appears to be more dynamic than has previously been shown which is illustrated by the gradient of water velocity and changes to the delta slopes of Lillooet-Green River delta.

Acknowledgements

Financial support for this research was provided by the National Sciences and Engineering Research Council of Canada, the Faculty of Graduate Studies and Research, and the Department of Geography and Environmental Studies, University of Regina.

I would like to express my appreciation for everyone who helped me get to this point. I would like to thank Dr. Kyle Hodder, my supervisor and mentor who provided countless hours of support in the field, the lab, and in the office to compile this thesis. I greatly appreciate his guidance and patience in working through this project. I would also like to thank Bob Nodge, my field and laboratory assistant. Without his ingenuity and resilience this project would not have been possible. I would also like to express my gratitude to my defence committee, including Dr. Ulrike Hardenbicker, Dr. Maria Velez, and Professor Michael Maerker.

Most importantly, I would like to thank my family and friends who have been incredibly supportive of me through this process and helped guide me through every step of the way. I would especially like to thank my fiancé, Mandy, who has provided an amazing amount of love and support throughout the thesis writing process. Without her continued encouragement and support I would not have got as far as I have.

Table of Contents

Abstract	i
Acknowledgements	iii
Table of Contents	iv
List of Figures	viii
List of Tables	xv
List of Symbols	xvi
List of Equations	xviii
1 Introduction	1
2 Literature Review	5
2.1 Fluvial hydrology	5
2.1.1 Hydrometeorology	5
2.1.2 Flow regime	7
2.2 Sediment transport.....	10
2.2.1 Suspended sediment	10
2.2.2 Diurnal Hysteresis.....	12
2.2.3 Mechanics of sediment transport.....	14
2.3 River deltas.....	16
2.3.1 Delta erosion and aggradation.....	18
2.4 Lacustrine processes.....	19
2.4.1 Thermal stratification	19
2.4.2 The Coriolis Force.....	22
2.5 Turbidity currents.....	23
2.5.1 Classification of turbidity currents.....	23
2.5.1 Examples of turbidity currents	25

2.5.2	Plunging inflow	26
2.5.3	Flow characteristics.....	29
2.5.4	Turbidity current flow velocity and travel lengths	31
2.5.5	Influence of Coriolis on turbidity currents	34
2.5.6	Flow interactions with the bed	34
2.5.7	Measurements and parameterization	36
2.6	Conclusions	38
3	Study area	40
3.1	Upper-Lillooet Basin.....	41
3.2	Lillooet Glacier	44
3.3	Slopes processes.....	44
3.3.1	2010 Mount Meager landslide	46
3.4	Lillooet River	47
3.4.1	Lillooet River hydrology.....	47
3.4.2	Lillooet River suspended and dissolved sediment	49
3.5	Lillooet-Green River Delta.....	50
3.6	Lillooet Lake	53
3.6.1	Lillooet Lake morphometry	53
3.6.2	Hydrometric lake levels	54
3.6.3	Lillooet Lake thermal stratification.....	55
3.6.4	Character of sediment in Lillooet Lake.....	58
4	Methodology.....	60
4.1	Meteorology	63
4.2	River stage and suspended sediment.....	63
4.2.1	LISST desktop analysis.....	66
4.3	Delta front monitoring.....	67

4.3.1	Water temperature moorings.....	68
4.3.2	Acoustic Doppler Current Profiler.....	68
4.3.3	Water column profiles.....	70
4.3.4	Bathymetric data.....	73
4.4	UAV surveys.....	73
5	Results.....	76
5.1	River hydrology and suspended sediment.....	76
5.1.1	Flow regime.....	76
5.1.2	Hydrometeorology.....	79
5.1.3	Suspended sediment concentration and grain size.....	81
5.2	Deltaic dynamics.....	85
5.2.1	Plunge line.....	85
5.2.2	Bathymetry dynamics.....	91
5.3	Lacustrine monitoring.....	94
5.3.1	Lillooet Lake Level.....	94
5.3.2	Lake temperature moorings.....	95
5.3.3	Spatio-temporal flow patterns.....	103
5.3.4	Water column properties.....	114
5.3.5	Froude number calculations.....	120
6	Discussion.....	122
6.1	Relationship between flow velocity and sediment concentration transportation 122	
6.2	Changes to the Lillooet-Green River delta.....	126
6.3	Lake currents.....	129
6.4	Process connections.....	132
7	Conclusions.....	135

7.1	Recommendation for future work	137
8	Literature Cited.....	140

List of Figures

- Figure 1: The daily hydrograph for a typical glacial meltwater stream. As the melt season progresses the amplitude of daily peaks in melting increases as well as the total daily melting that occurs between May and July. Reproduced with permission from John Wiley and Sons under license number 4553240912392 on 20-Mar-2019 from Figure 4.10 on page 98 in Bennett and Glasser (2009): *Glacial Geology: Ice Sheets and Landforms*, 2nd Edition.9
- Figure 2: Clockwise hysteresis in a plot of suspended sediment concentration (SSC; here expressed as turbidity) and discharge (U). Clockwise hysteresis indicates that the peak SSC occurs before the peak U. Reproduced with permission from Elsevier under license number 4553240794473 on 20-Mar-2019 from Figure 6 on page 118 in Lawler et al. (2006): *Science of The Total Environment*, Volume 360.14
- Figure 3: Sediment transport modes. Reproduced with permission from John Wiley and Sons under license number 4553240635112 on 20-Mar-2019 from Figure 6.10 on page 121 in Leeder (2011): *Sedimentology and Sedimentary Basins: From Turbulence to Tectonics*, 2nd Edition.16
- Figure 4: Sedimentary facies of a Gilbert-type delta. The topset is flat lying, separated by a sudden change of slope also known as a brinkpoint. The foreset is composed of steeper sloped sedimentary beds often developed from suspension fall-out and avalanching of material off the topset. The toeset is separated by another break in slope and forms a much flatter plain. Reproduced with permission from John Wiley and Sons under license number 4553240452683 on 20-Mar-2019 from Figure 1 on page 292 in Kleinhans (2005): *Sedimentology*, Volume 52.18
- Figure 5: Theoretical plot showing the thermal stratification of a lake. The figure shows three strata including the uppermost epilimnion, the transitional metalimnion, and the bottom-most hypolimnion.20
- Figure 6: Diagram showing the stages of turbidity current development. The turbidity current moves from open water flow in a river channel to a plunge point where the slope break occurs. The flow plunges below the surface at this point and move down the slope as an undercurrent. Reproduced with permission from Geological Society of America under their special “fair-use” license agreement from Figure 2 on page 1068 in Lamb and Mohrig (2009): *Geology*, Volume 37.27
- Figure 7: Location map of Lillooet Lake basin. The map shows the location of the three largest tributaries to Lillooet Lake including Lillooet River, Green River, and Birkenhead River. The map also shows the location of Lillooet Glacier. The inset map shows the location of Lillooet Lake in context of the province of British Columbia.44

- Figure 8: Peak flow for Lillooet River from 1914-2016. Black lines represent reported peak flow. Grey lines are the maximum annual flow for years where no peak flow is reported. [data source: station 08MG005, Water Survey of Canada, 2015]48
- Figure 9: Recurrence series of annual instantaneous peak discharge events on Lillooet River. Data is from 1914-2016. [data source: station 08MG005, Water Survey of Canada, 2015]48
- Figure 10: Map of Lillooet River, Delta, and Lake mapped from Landsat 8 OLI imagery dated 01-August-2015. The bathymetric contours are digitized from BC Ministry of Environment bathymetric map of Lillooet Lake (c. 1987). The difference in the Landsat 8 shoreline and the shoreline from the contour map shows the delta progradation that has occurred in the 28 years between 1987-2015.....52
- Figure 11: Lillooet Lake water levels recorded from 1971 to 2016 reported by the Water Survey of Canada gauge 08MG020. Panel (a) shows the daily lake level from 1971-2016. Panel (b) shows the duration curve for daily water levels. The median water level in the lake is 25.63 metres, shown by the dotted line. Water levels are recorded to an assumed datum and have not been referenced to a geodetic datum.55
- Figure 12: Panel (a): SSC in Lillooet River compared to (b) lake water temperature and (c) lake transmissivity measured in the lake 1 km from the delta. Reproduced with permission from Canadian Science Publishing under license number 4553230551874 on 20-Mar-2019 from Figure 6 on page 1702 in Gilbert (1975): Canadian Journal of Earth Sciences, Volume 12.....57
- Figure 13: Flow chart showing equipment deployments in Lillooet Lake during the 2015 field campaign. Field data was collected for 9 days from 22-July to 31-July-2015. Due to the remoteness of the field site and small inflatable boat only a limited amount of equipment could be deployed or retrieved each day.61
- Figure 14: Map showing the fixed equipment deployments at the Lillooet-Green River delta. The Buoys and aDcp were moored at the bottom of the lake with anchors and attached to floats at the surface for retrieval. The background mapping was done manually from Landsat OLI imagery from 01-August-2015 (© USGS).....62
- Figure 15: An example of the SSC - Turbidity rating curves used to evaluate the processing of water samples taken during this study. Panel (a) shows instantaneous turbidity measurements compared to level-1 processed water. Panel (b) shows 10-minute averaged turbidity measurements compared to level-1 processed water. Panel (c) shows instantaneous turbidity measurements compared to level-2 processed water. Panel (d) shows 10-minute averaged turbidity measurements compared to level-1 processed water. Panel (e) shows instantaneous turbidity measurements compared to level-3 processed water. Panel (f) shows 10-minute averaged turbidity measurements compared to level-1 processed water. The samples that were diluted and submerged in a sonic bath

[level-2 processing, panels (c) and (d)] showed the best relationship to turbidity measurements.....	66
Figure 16: Deployment diagram of the setup of the aDcp mounted on the Sea Spider platform. Each bin records a 2-metre high column of water above the aDcp. The total field-of-view of the 10 bins on the aDcp is 1 to 21 metres above the lake bed.	70
Figure 17: Location for water profiles that were collected on July 29 and July 30, 2015.	72
Figure 18: Study areas for remotely sensed data used in this study area. These datasets include UAV imagery and bathymetric transects in the area immediately offshore the delta.	75
Figure 19: Water Survey of Canada hydrographs of Lillooet River (08MG005). Panel (a) shows the mean, maximum, and minimum daily flows over calendar years 1914-2016. There is significant variation in flow data, especially in the fall months because of infrequent Pacific storms. Panel (b) shows the frequency of which months report the greatest amount of annual peak flow events per calendar year. July is by far the month with the most peak flow values, followed distantly by June and August. Panel (c) shows the daily hydrograph for 2015. In this hydrograph there is significant variability observed, with the peak flow occurring in September. The period between July 21 to August 31 is a large dip in flow activity compared to earlier that summer and the large storm peaks that exist in September and October. Panel (d) shows the average daily discharge from 1914-2016 with the range of observed flows (191402916) around it. The daily discharge values from 22-31 of July 2015 are at the bottom edge of the range box. Flow on 27-July-2015 is the lowest flow reported for that calendar day in the period of 1914-2016.....	77
Figure 20: Meteorological variables affecting runoff. Air temperature, solar radiation, and discharge all have very similar wavelengths but different phases of diurnal peaks. This trend is expected as air temperature and solar radiation are contributors to runoff of Lillooet River. The timing of each peak is slightly different with solar radiation peaking first, air temperature peaking after that then discharge peaking early in the AM as a response to those other variables. Precipitation was recorded for three days; however very little precipitation was recorded, and it appeared to have almost no impact on the response of the hydrograph.....	80
Figure 21: Field photographs showing the amount of haze in caused by the forest fires located higher up in the valley. The photo in the left panel was taken on July 29 and is looking upstream of Lillooet River from the delta. The mountains in the background are shrouded with haze, resulting from forest fires in the region. The right panel was taken on July 30 and is looking down Lillooet Lake from Lillooet River delta. Haze is evident in the distance.	81

- Figure 22: Timeseries of SSC and mean particle size. Mean particle size is shown as well. Mean particle size is plotted on a log-scale and does not appear to follow the same diurnal pattern as SSC. The gap in the middle of the data on July 27-28 is due to changing the batteries on both the water sampler and turbidity probe.82
- Figure 23: Hysteresis loops of SSC and river height. The top panel (a) shows the time series of SSC and river height in their joint period of record. Each curve exhibits a characteristic diurnal pattern. The bottom panel shows the hysteresis loops from July 28-29 (b) and July 29-30 (c). Both curves have a counter clockwise loop, indicating negative hysteresis.84
- Figure 24: The left pane shows SSC vs mean particle size. There is a slight decreasing trend in mean particle size as SSC increases. This is obscured at the lower end of SSC where a large range of particle size values exist (n=48). The right pane shows particle density vs. mean particle size. There is a slight trend that as particle size is increasing, so too is particle density (n=7).85
- Figure 25: Oblique aerial image of the plunge line and lobe (July 28). The incoming river water is at the bottom of the image. The incoming river water plunges below the surface of the lake at the location of the plunge line. This line is the boundary between incoming river water and ambient lake water. K-H instabilities were observed to form on the north side of the inflowing river water indicating shear stresses at the flow boundary between the two water masses.....88
- Figure 26: Landsat 8 image showing plunge line on Lillooet-Green River delta (August 1, 2015). The black line is the rough location of the plunge line mapped from the Landsat 8 imagery. Point A shows the lobe that formed on the NE end of the plunge line.....89
- Figure 27: Migration of the channel bank at Lillooet Lake. The shorelines were mapped from either UAV imagery, by a Garmin 62S GPS, or else by Landsat 8 imagery. The changes to the position of the shoreline are not equal across the length of the shoreline and more erosion is observed at the lakeward edge. The benthic channel positions were taken from the bathymetric surveys that were collected over multiple days in front of the Lillooet-Green River delta. The position and orientation of the apparent benthic channel appear to shift throughout the period of observation.....90
- Figure 28: Map showing the locations of the bathymetric Cross-sections A-A' and B-B'. The black points along each cross section represent 50 metre distances along those cross sections. In the background mapping, the plunge line appears at 100 metres along Cross-section A-A' and 160 metres along Cross-section B-B'93
- Figure 29: Bathymetric cross sections take at the front of the Lillooet-Green River delta. Cross-section A-A' (panel a) extends from the mouth of the river out into the lake 200 metres in a southeast direction. The depth increases from 0.8 metres to 29 metres. Cross-section B-B' (panel b) extends from the mouth of the river into the

lake 250 metres in an east direction. The depth increases from 0.8 metres to 53 metres.....	94
Figure 30: Water Survey of Canada lake level summary data from 22-July to 01-August (WSC gauge 08MG020). The black line represents the lake level data from 2015, while the grey box is the range of lake level data from the period of record (1971-2016). The dark grey line is the average lake level date for each date. Lake level during this period was very low, resulting in a greater exposure of deltaic sediments.....	95
Figure 31: Lake temperature moorings (shown in black) located at the front of Lillooet-Green River delta. Data was averaged over 15-minute period. From left to right are buoy 1, buoy 2, buoy 3 and from top to bottom are the top, middle, bottom sensors (e.g. top left sensor is Buoy 1, Top sensor, bottom right sensor is Buoy 3, Bottom sensor). Lake temperature (, as measured from the nine sensors does not appear to respond to river temperature. This indicates there is not a substantial relationship between any of these sensors and the measured river temperature (shown in red).	96
Figure 32: Wavelet transform using the Morlet wavelet on the lake-temperature sensors (Top 1-3, Middle 1-3, Bottom 1-3). Across all sensors there is 24-hour scale shared variance. This indicates that all the temperature sensors are responding, in part, to diurnal changes in water temperature.....	102
Figure 33: Current velocity measured by a bottom-mounted aDcp in Lillooet Lake. The aDcp was mounted in 31 metres of water and measured water to a height of 20 metres above the lake bed. Each of the 10 cells measured current direction and velocity in 2 metre bins. A review of the data shows that the aDcp captured the bottom edge of inflowing river currents.	105
Figure 34: Current direction measured by a bottom-mounted aDcp in Lillooet Lake. The aDcp was mounted in 31 metres of water and measured water to a height of 20 metres above the lake bed. Each of the 10 cells measured current direction and velocity in 2 metre bins. After reviewing the data, it appears as though the aDcp captured the bottom edge of inflowing river currents. The orange shades show currents that are being directed from the front of the Lillooet-Green River delta. Blue and green currents are directed from down-lake, indicating the presence of counter-currents.	106
Figure 35: Velocity statistics from the 10 cells in the aDcp. The trend is for current velocity to increase with increasing distance from the bed. The bar is the range between the upper and lower quartiles, with the black line being the median current velocity. The outer bars represent the lowest and highest flow events recorded in those cells.....	107
Figure 36: aDcp, river stage, and SSC timeseries. For plotting purposes, all data is averaged per 10 minutes.	109

- Figure 37: ADcp data from 28-July-2015. Panel (a) shows current velocity of all 10 cells on a hot-cold colour ramp. Panel (b) shows current direction data for all 10 cells by 16-point compass direction. Panel (c) shows the velocity profile of Cell 10 (18.55-20.5 m). The large peak in current velocity beginning at 03:15am is the largest current velocity measured during the period of record. Peaks in current velocity tend to occur at 3-minute intervals. Most peaks last only 1 minute, although the larger peaks were recorded up to 3 minutes in duration. The large peaks in current velocity appear to extend down in the water column.110
- Figure 38: ADcp data from 28-July-2015. The top plot shows current velocity of all 10 cells on a hot-cold colour ramp. The currents at the very top of graph appear to extend down into the water column, some last for several minutes, and this current appears to billow possibly due to turbulence at the interface. The middle plot shows current direction data for all 10 cells by 16-point compass direction. The bottom plot shows the velocity profile of Cell 10 (18.55-20.5 m). Cell peaks appear to occur every 3-4 minutes regularly. The large velocity peak on the bottom plot at 23:35 lasts for 10 minutes before falling again.111
- Figure 39: Wavelet analysis of the aDcp cell 10 data. The top graph shows the Morlet wavelet transformation and the bottom graph shows the DOG-2 wavelet transformation. Both graphs show the time series (minutes) along the bottom X-axis and the logarithmic-scale (base 2) on the y-axis. The data show that from a time-scale of $2^{8.5}$ to $2^{10.5}$ minutes there is global periodicity in the data along the entire time series. At smaller time-scales 2^1 to 2^7 there is periodicity that is observed at certain times throughout the data.....113
- Figure 40: Map showing the location of water profiles collected using a castable CTD. Profiles A-I were collected on July 29. Profiles J-M were collected on July 30. An interflow was observed at profiles J-L and an underflow was observed at profile M.118
- Figure 41: Water profiles from July 29. Profiles A-I are shown. The casts at these locations show no evidence of an intruding underflow or intercurrent entering Lillooet Lake from the delta. The abrupt change observed at 30 metres depth appears to show the stratification of Lillooet Lake, with the warmer metalimnion above and much colder, denser hypolimnion below.....119
- Figure 42: Water profiles from July 30. Profiles J-M shown. These casts appear to show the intrusion of an interflow (J-L) and an underflow (M) entering Lillooet Lake. This flow is characterized by a much higher SSC. The specific conductance and temperature profiles of these flows do not show significant difference from the surrounding ambient water which already have a very low specific conductance and cool temperature profile.120
- Figure 43: Water profiles from July 29. Profiles N-Q shown. These profiles were taken much further away from the delta than previously reported profiles in much deeper water. The casts show the stratification of Lillooet Lake with a thin

hypolimnion at the surface, a 30-metre thick metalimnion and cold, dense
hypolimnion that extends to the bottom of the lake.....120

List of Tables

Table 1: Maximum suspended sediment concentrations (SSC _{max}) of alpine, glacial rivers of Western Canada. The range of reported SSC values is reported as mg l ⁻¹ of sediment mass to ambient fluid volume. SSC is reported as maximum observed SSC within each study.	11
Table 2: Physical characteristics of Lillooet Lake based on BC MOE bathymetric map (1987).....	53
Table 3: Migration of the channel delta bank. The amount of change measured below is the difference between the location of the lakeward end of the mapped shoreline between the first date and the second date listed below. Cumulatively between July 16 and August 9, 2015 a total of 156 metres of lateral migration was observed.	89
Table 4: Correlation matrix between lake temperature sensors deployed into Lillooet Lake. The Top sensors and Bottom 2 sensor show poor correlation to the remaining sensors. Bolded and shaded values depict correlations greater than r=0.7.	97
Table 5: Water profile properties in front of Lillooet delta. Froude number subscripts refer to corresponding flow velocities in centimeters per second. Flow at higher velocities are supercritical at all water profile locations but with lower velocity (F ^{6.8}) flow is just barely subcritical indicating a transition to a depositional environment.	121

List of Symbols

Symbol	Description of term	Units
C	Sediment volume concentration	$\mu\text{l l}^{-1}$
C_c	Threshold concentration	ml l^{-1}
d	Turbidity current flow thickness	m
F	Froude number	\sim
f	Coriolis frequency	rad s^{-1}
f_b	Darcy-Weisbach friction coefficient, bottom boundary	\sim
F_{dp}	Froude number at plunge point	\sim
f_i	Darcy-Weisbach friction coefficient, top boundary	\sim
g	Acceleration due to gravity	m s^{-2}
g'	Buoyancy reduced gravitational acceleration	m s^{-2}
h	Height (or depth) of water	m
HI	Hysteresis Index	\sim
h_p	Critical depth for plunging current	m
k	Coefficient for hysteresis index	\sim
K_{1-4}	Coefficients for defining Salinity	\sim
L	Coriolis length scale	km
L_F	Latent heat of fusion	J kg^{-1}
M	Melt rate	kg s^{-1}
M_i	Annual glacier ice melt	mm a^{-1}
M_s	Annual snowmelt	mm a^{-1}
P_a	Atmospheric pressure	N m^{-2}
P_r	Absolute pressure	N m^{-2}
P_s	Annual precipitation	mm a^{-1}
P_s	Submerged pressure	N m^{-2}
Q_E	Latent heat flux	W m^{-2}
Q_G	Ground heat flux	W m^{-2}
Q_H	Sensible heat flux	W m^{-2}
Q_L	Net longwave radiation	W m^{-2}
Q_M	Energy consumed by melting	W m^{-2}
q_p	Discharge at the plunge point	$\text{m}^3 \text{s}^{-1}$
Q_R	Sensible heat supplied by precipitation	W m^{-2}

Q_s	Net shortwave radiation	W m^{-2}
R	Submerged specific density of sediments	kg m^{-3}
RH_{max}	Maximum river height in single peak hydrograph	m
RH_{mid}	Midpoint of river height in single peak hydrograph	m
RH_{min}	Minimum river height in single peak hydrograph	m
R_i	Richardson number	~
R_o	Rossby Number	~
S	Slope	°
S_a	Salinity	PSU
S_c	Specific conductance	$\mu\text{S cm}^{-1}$
SSC	Mass suspended sediment concentration	mg l^{-1}
SSC_{ft}	SSC of the falling limb	mg l^{-1}
SSC_{max}	Maximum suspended sediment concentration	mg l^{-1}
SSC_{rt}	SSC of the rising limb	mg l^{-1}
T	Temperature	°C
u_f	Current velocity	$\text{m}^3 \text{s}^{-1}$
U	River discharge	$\text{m}^3 \text{s}^{-1}$
\bar{U}	Depth average current velocity	$\text{m}^3 \text{s}^{-1}$
z_f	Depth of current	m
δm	Change in mass	kg
δt	Change in time (annum)	a
$\delta\rho$	Excess density of turbidity current over the ambient fluid	kg m^{-3}
θ	Latitude	°
ρ_a	Density of ambient lake water	kg m^{-3}
ρ_f	Bulk density of turbidity current flow	kg m^{-3}
ρ_s	Density of sediment	kg m^{-3}
ρ_w	Density of freshwater meltwater	kg m^{-3}
τ_b	Shear stress, bottom boundary	N m^{-2}
τ_i	Shear stress, top boundary	N m^{-2}
Ω	Earth's rotation rate	rad s^{-1}

List of Equations

Equation	Eqn. No.
Glacier mass balance	(1)
Energy balance equation	(2)
Energy available for melting	(3)
Melt rate of glacial ice	(4)
Richardson Number	(5)
Rosby Number	(6)
Coriolis Frequency	(7)
Threshold concentration of suspended sediment for plunging river water	(8)
Submerged specific density of sediment	(9)
Threshold depth for plunging	(10)
Excess density of turbidity current	(11)
Froude number of a submerged turbidity current	(12)
Buoyancy reduced gravitational acceleration	(13)
Mean flow velocity of turbidity current	(14)
Shear stress at the bottom interface of an underflowing turbidity current	(15)
Shear stress at the top interface of an underflow/interflowing turbidity current	(16)
Bulk density of turbidity current	(17)
Depth of water calculated from pressure	(18)
Submerged pressure calculated from absolute pressure	(19)
Midpoint of river height in a single peak hydrograph	(20)
Hysteresis Index (clockwise)	(21)
Hysteresis Index (counter-clockwise)	(22)
Bulk density of water	(23)
Practical Salinity Scale	(24)

1 Introduction

Turbidity currents are a relatively well documented natural process in both limnology and oceanography. Since their discovery by François-Alphonse Forel in 1885, many researchers around the world have investigated them from both a sedimentological perspective and from a hydrologic perspective (Lambert and Giovanoli, 1988; Normark and Dickson, 1976; De Cesare et al., 2006). Due to their episodic nature and relative inaccessibility to direct human observation, turbidity currents have often been studied in laboratories by conducting flume experiments where flows may be more easily parameterized than in nature. It is from these laboratory experiments that much of the governing equations regarding turbidity current flow and sediment transportation have been developed. By design, the laboratory setting focuses on turbidity currents under controlled conditions and field monitoring of turbidity currents can therefore add valuable knowledge to our understanding of the way turbidity currents behave in the natural world.

Turbidity currents are a type of density current. Density currents are currents which flow as a result of excess density from the surrounding water. Excess density can be derived from differentials in temperature, presence of dissolved solids, or from suspended sediments. Turbidity currents derive their excess density primarily from an excess of suspended sediments. They fall into a class of density currents known as suspension currents (Simpson, 1997). Suspension currents loft or suspend sediment particles within them which causes an increase in fluid density in the current relative to the surrounding fluid. Examples of other suspension currents include powder snow avalanches or flowing materials from volcanic eruptions (Simpson, 1997). Mixing of the density current with

the ambient fluid will erode the density differential and eventually result in loss of excess density. Turbidity currents have been observed in many different environments such as lakes, reservoirs, and oceans (Kneller and Buckee, 2000). There are several different mechanisms that initiate turbidity currents including the inflow of river water with a high sediment load, underwater avalanches caused by earthquakes or eruptions, or over-steepening of unconsolidated sediments on a subaqueous slope (Mulder and Alexander, 2001).

Turbidity currents have been most studied and are best understood in the marine context. In these environments they are considerably larger in size and velocity than their freshwater counterparts. Marine turbidity currents have been identified as a major geomorphic mechanism of sediment flux to submarine fans (Mulder and Alexander, 2001). Their geological deposits are called turbidites and form sedimentary beds that can yield hydrocarbon reservoirs (Mulder and Alexander, 2001). Turbidity currents that develop in freshwater, or lacustrine environments, have been studied much less than those currents in oceans but can be easier to study in-situ (Weirich, 1985; Crookshanks, 2008). This is because lacustrine turbidity currents have much less energy and tend to flow at lower velocities and with less entrained sediment than those in the oceans. Consequently, the magnitude of associated deposits is much less. In the lacustrine setting it is much easier for inflowing water to entrain enough suspended sediment to plunge below the surface of ambient lake water than it is in the marine setting. This is primarily due to the decreased density differential between the two fresh-water masses. However, there still needs to be a suitable density differential between these two masses of water to avoid mixing with ambient lake water.

Since turbidity currents require an abundance of suspended sediment to generate excess density, selection of a field site at which to study turbidity currents that has a large supply of source sediment is important. For this reason, the study of lacustrine turbidity currents often occurs in alpine, glacier-fed systems in which there is seasonally abundant sediment, flow power, and stream capacity to entrain and transport large amounts of sediment into receiving ambient water. Within Western Canada, there are many candidate basins that meet this criterion. In several basins, including Lillooet basin in British Columbia and Slims River basin in Yukon, turbidity currents are a well-documented phenomenon (Gilbert, 1975, Crookshanks, 2008). In these environments, turbidity currents have been shown to occur daily during periods of high-summer flows. Turbidity currents can persist for months if the river flow and corresponding sediment concentration are great enough and sustained over a long period of time.

The mechanisms and linkages between inflowing river water and turbidity current dynamics are not straight forward. Within the literature, several researchers have identified velocity pulsations associated with the passage of turbidity current flow (Best et al., 2005; Lambert et al., 1976; Normark and Dickson, 1976). Velocity pulsations have been observed and reported on for decades within the turbidity current literature, but in many circumstances the explanation in one setting does not account for the variables observed in another setting. Best et al. (2005) found that when turbidity currents on Lillooet Lake plunged beneath the lake surface the plunge line shifted laterally and this causes “a distinct temporal velocity pulsing at any one point” (Best, et al., 2005). This pulsing occurred with a regular periodicity of 3-12 minutes. The current shifting has gained little attention by other such studies of turbidity currents.

Located in the southern Coastal Mountains of British Columbia, Lillooet Lake has been extensively studied and turbidity currents are a well-documented phenomenon. Past studies of turbidity currents in Lillooet Lake have shown that these currents can be formed by the incoming river water of Lillooet River and flow initiates at the front of the Lillooet-Green River delta. To expand on the extensive body of work that has been done on Lillooet Lake and to try and better understand the connections between incoming river water and turbidity currents within the lake, this study aims to study turbidity currents and the processes that are responsible for them. The objectives of this research are meant to help understand the properties and flow-dynamics of these turbidity currents that are produced by incoming river flow. The research objectives are:

- | | |
|---|---|
| To document the relationship between suspended sediment and discharge rates in Lillooet-Green River. | 1 |
| To document the variability of flow properties of turbidity currents in Lillooet lake. | 2 |
| To understand how bathymetric properties of turbidity currents are influenced by or influence the passage of turbidity currents at the front of Lillooet-Green River delta. | 3 |

By setting out to answer these research objectives laid out by this study, it will help to expand on the body of knowledge that current exists on lacustrine turbidity currents as well as the hydrology and sedimentology of Lillooet Lake and fill in gaps within the literature on these processes. Past studies have tended to lack either temporal-scale or spatial-scale necessary to capture these processes in Lillooet Lake and combined with in-river monitoring, this study addresses the linkages between suspended sediment and discharge as well as turbidity current flow properties in Lillooet Lake.

2 Literature Review

The following literature review seeks to help understand the three research objectives posed in Chapter 1, which form the basis for conducting this work. These research objectives explore the dynamics and mechanisms that deliver water and sediment derived from the river to depths within the Lillooet Lake basin. In order to understand these objectives and to gain a fuller appreciation for the processes which govern them, the entire drainage system, from upstream glaciers to the characteristics of downstream lakes, must be understood. The following sections describe the processes and mechanisms that drive turbid river flow to plunge below the surface of a lake.

The following literature review is divided into seven sections. Each section describes the processes at work which deliver sediment and meltwater into downstream receiving basins where that meltwater may plunge below the surface of the lake. These sections are arranged in such a way as they describe the processes in order, beginning with the orogeny of meltwater from a glacier and ending with the physical characteristics of lakes.

2.1 Fluvial hydrology

2.1.1 Hydrometeorology

In alpine, glacial environments, such as the focus of this study, summer river flow is often governed by glacier melt. The amount of melt a glacier undergoes is controlled by that glacier's mass balance. Glacier melt represents the largest loss of mass to a glacier within the annual mass balance (Cuffey and Paterson, 2010). Mass balance is the difference between the losses and gains to a glacier's ice mass (Bennett and Glasser, 2009) and can be described as:

$$\frac{\delta_m}{\delta_t} = P_s - M_s - M_i \quad (1)$$

Where δ_m/δ_t is the change in mass of the glacier over time, P_s is the annual precipitation, M_s is the annual snowmelt occurring on the glacier, and M_i is the annual glacier ice melt (Comeau et al. 2009). The mass balance of a glacier is typically governed by the surficial energy balance (Hock 2005). The surficial energy balance is the largest input of energy to a melting glacier, although there are subsurface processes that can affect melting. These subsurface processes include the geothermal heat flux, surficial melt draining within and beneath the glacier, heat exchange from within the glacier and the atmosphere, and frictional heat generated by glacial flow. Each of these processes can induce melting (Benn and Evans, 1998; Bennet and Glasser, 2009; Cuffey and Patterson, 2010). However, the influence of these factors on subsurface melting is generally considered weak. While the impacts of surface melting can be measured in metres per year the impacts of subsurface melting are more commonly measured in millimetres per year (Bennet and Glasser, 2009). Therefore, it is reasonable to think of surficial melt as being the main loss when balancing the mass balance equation.

The surficial melting of a glacier can be described by the energy balance equation and is expressed as

$$Q_L + Q_S + Q_H + Q_E + Q_G + Q_R + Q_M = 0 \quad (2)$$

Where Q_L is the net longwave radiation, Q_S is the net shortwave radiation, Q_H is the sensible heat flux, Q_E is the latent heat flux, Q_G is the ground heat flux, Q_R is the sensible heat supplied by precipitation, and Q_M is the energy consumed by melting (Hock, 2005). We can set the term Q_M equal to all other terms because all surplus energy used to raise the surface of the ice above 0°C can be assumed to be used immediately for

melting ice (Hock, 2005). We can also set Q_G and Q_R equal to zero and omit these terms as they are negligible compared to the others (Ben and Evans, 1998 and Hock, 2005).

This results in the following equation to account for the energy required to melt a glacier:

$$Q_M = Q_L + Q_S + Q_H + Q_E \quad (3)$$

The melt rate of a glacier can then be calculated with the following equation:

$$M = Q_M / \rho_W L_F \quad (4)$$

Where Q_M is the energy required to melt a glacier, ρ_W is the density of water, and L_F is the latent heat of fusion (Hock, 2005). Net radiation is the dominant factor controlling glacier melt, especially at higher elevations due to a reduced turbulent flux associated with the vertical lapse rate of air temperature and vapour pressure with elevation (Bhutiyani, 2000; Hock, 2005). The main consequence then is that latent heat (Q_E) and sensible heat (Q_H) are less important to the process of melting glacial ice than net radiation. The importance of net radiation on glacier melting can also be shown from the large diurnal swing in melt rates of a glacier from a peak during the day to very little or no melting at night (Figure 1; Bennet and Glasser, 2009).

2.1.2 Flow regime

Glacially-derived rivers in mountainous environments tend to have flow regimes where snow melts precedes glacier ice melt. This can result in either a single or a two-peak hydrograph in which spring-snowmelt runoff is superseded by peak flow generated by glacier melt, with the latter responding to summer energy supply at a time by which snowpack has largely melted (French and Slaymaker, 1993; Eaton and Moore, 2010). The peak(s) on the hydrograph may be joined to show one large summer peak or they may be separated and show two peaks in the summer melt season. Glacial meltwater

flows into drainage networks which carries sediment downstream. Production of meltwater can vary with energy supply, at both diurnal and seasonal scales (Figure 1; Bogen, 1996; Bennett and Glasser, 2009). Diurnal variation is such that daytime heating and radiative effects produce more meltwater during the day than at night (Bennett and Glasser, 2009). Because of this, the idealized daily hydrograph of meltwater at the ice margin will peak in the afternoon and be at its lowest in the early morning (Bennett and Glasser, 2009). This timing corresponds to when the drainage network within the glacier has reached its maximum efficiency and when daytime heating and the radiation balance are at their peak (Bennett and Glasser, 2009).

The daily hydrograph can also change throughout the season to reflect the increased efficiency in the internal glacial drainage network, which is seen by an amplification of the daily peaks as summer progresses (Figure 1). The annual hydrograph for an alpine, glacial stream can have one or two peaks. This may depend on the elevation range within the drainage basin and the amount of glacier cover present (Eaton and Moore, 2010). If a stream hydrograph shows a single peak in annual flow, that single peak tends to capture both high flows associated with early summer snow-melt and later summer glacier melt. (Eaton and Moore, 2010). If a stream has two peaks, then there is an early summer peak attributed to snow melt and a later peak in the summer that is attributed to glacier melt (Gilbert, 1973; Bennett and Glasser, 2009).

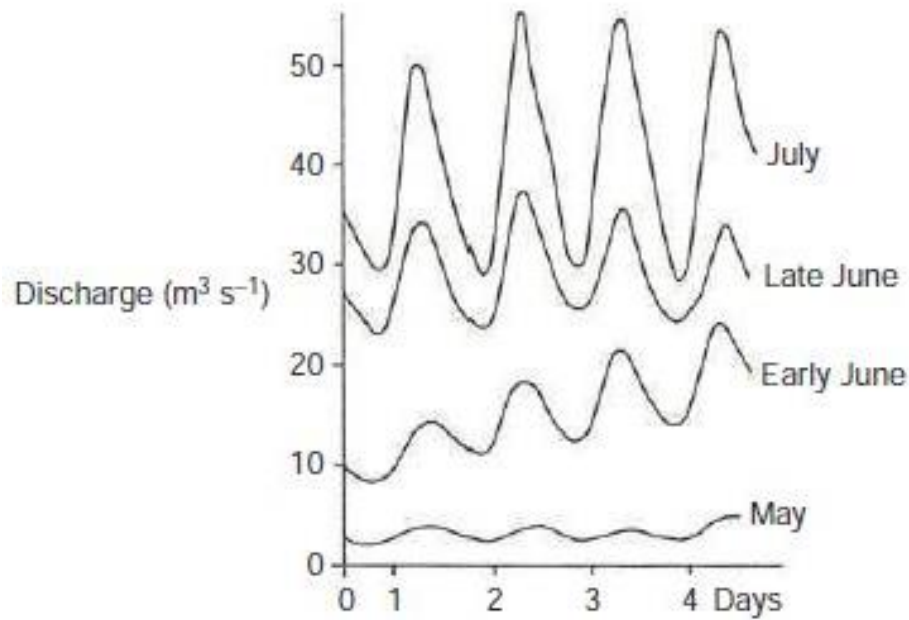


Figure 1: The daily hydrograph for a typical glacial meltwater stream. As the melt season progresses the amplitude of daily peaks in melting increases as well as the total daily melting that occurs between May and July. Reproduced with permission from John Wiley and Sons under license number 4553240912392 on 20-Mar-2019 from Figure 4.10 on page 98 in Bennett and Glasser (2009): *Glacial Geology: Ice Sheets and Landforms*, 2nd Edition.

As melting of the glacier is initiated each day, a new peak is generated on the hydrograph. Although the peak melt tends to be in the afternoon, peak flow at any given river gauge will lag with distance downstream due to the travel time in the drainage network. The travel time, referred to as lag time, can be several minutes to hours depending on the length of the channel between meltwater source and the gauge as well as the flow velocity of water. If the lag time is sufficiently long, the peak may take several hours to days to reach downstream. Estimation of lag time may be made from comparing multiple hydrograph peaks or using hydrologic or hydraulic routing models (Bedient and Huber, 2002).

2.2 Sediment transport

2.2.1 Suspended sediment

Alpine, glacial rivers can transport large volumes of sediment within their reaches. This is due to both the large amount of sediment supply available for mobilization and the high slopes that are present. The suspended sediment in stream flow is a function of the sediment supply and energy conditions (e.g. sediment is stored at low flow and transported at high flow; Bhutiyani, 2000; Bača, 2008). Suspended sediment concentration in meltwater is highly variable at both short-term and seasonal time-scales and can vary with availability of sediment within the subglacial system (Collins, 1979; Bogen, 1996). Sediment may come directly from glaciers or indirectly from proglacial sediments, debris flows, landslides, soil creep, sediment runoff from anthropogenic impacts, and/or bank erosion (Jordan and Slaymaker, 1991; Mao and Carrillo, 2017).

Past studies of alpine, glacial rivers in Western Canada have shown very large differences in mass suspended sediment concentration (SSC; Table 1). The largest discharge events are not always coincident with the largest magnitudes of SSC (Smith, 1978; Willis, 1996; Sawada and Johnson, 2000). On the Slims River in the Yukon, the largest SSC event did not correlate to discharge data but was an outlier (Sawada and Johnson, 2000). In the same study, the authors noted similar discharge magnitudes between years can be associated with SSC that vary up to three times in magnitude. In another study examining the paleoenvironmental record of Lillooet Lake, the authors showed that the largest sediment accumulations in the paleoenvironmental record did not correspond with historic floods but rather was linked with other processes such as landslides or basal changes to the upstream glaciers (Heideman et al., 2015). In another

alpine, glacial setting in Norway, the authors attributed sudden flushes of suspended sediment in the channel to hydraulic changes beneath the glacier, which resulted in a weak (linear) relationship between SSC and discharge (Willis, 1996). In their study of Hector Lake in Alberta, Smith (1978) also recognized that the SSC-discharge relationship can break down with outlier values of SSC. In a study in Norway, the authors found that sediment yield was significantly smaller than expected and that changes in the basal meltwater channel network that may occur over several years may be responsible for large changes in the availability of sediment (Bogen, 1996). Precipitation can have an adverse effect on the SSC-discharge relationship by causing an increase in fluvial discharge without a uniform increase in SSC, especially when the sediment sources are subglacially derived (Collins, 1979). Other meteorological factors can adversely impact this relationship by controlling rates of meltwater production without sediment concentration showing a direct response (e.g. cloud cover or low air temperatures; Collins, 1979).

Table 1: Maximum suspended sediment concentrations (SSC_{max}) of alpine, glacial rivers of Western Canada. The range of reported SSC values is reported as mg l⁻¹ of sediment mass to ambient fluid volume. SSC is reported as maximum observed SSC within each study.

Location of study	Authors(s)	SSC_{max} (mg l⁻¹)
Balfour Stream, AB	Smith et al. (1980)	768
Bow Outwash, AB	Smith et al. (1980)	1,193
Lillooet River (above Silt Lake), BC	Schiefer and Gilbert (2008)	400
Lillooet River (near Lillooet Lake), BC	Gilbert (1975)	3,000
Meltwater from Athabasca Glacier	Gilbert (1981)	2,500
Peyto Creek, AB	Smith et al. (1980)	2,156
Peyto Creek, AB	Chikita (1996)	5,500
Slims River, YK	Sawada and Johnson (2000)	11,900
Slims River, YK	Crookshanks and Gilbert (2008)	5,000
Surprise Creek, BC	Gilbert (2004)	1,425
Unnamed Creek, BC	Weirich (1985)	~700

2.2.2 Diurnal Hysteresis

Suspended sediment concentration has been shown to be weakly dependent on discharge in previous studies (Collins, 1979; Baca, 2008; Crookshanks, 2008). Hysteresis of the SSC- discharge relationship helps explain some of this variability. If two variables, plotted on a time-series have a similar pattern but are nonsynchronous in their timing, then the pattern is hysteretic (Landers et al., 2013). The SSC-discharge relationship is determined by the sediment supply and transport capacity of discharge. In the case of the SSC-discharge relationship, if the SSC peak leads the discharge peak then the hysteresis is clockwise (positive) and can be seen in a plot of SSC-discharge (Figure 2). Conversely, if the SSC peak lags the discharge peak, the relationship is counter-clockwise (negative). The SSC-discharge relationship can also be non-hysteretic. Hysteresis in the discharge-SSC relationship has often been studied as a way of interpreting the source and availability of sediment supply (Landers et al., 2013; Mao and Carrillo, 2017). Most studies (seemingly regardless of setting) tend to observe clockwise hysteresis (Bača, 2008) although there is evidence of both clockwise and counter-clockwise hysteresis in the literature (Mao and Carrillo, 2017 and Crookshanks, 2008).

Previous studies have sought answers to explain the hysteretic relationships between SSC-discharge. One common explanation for clockwise hysteresis is that during low flow events sediment is deposited in-stream. Sediment is then remobilized during the rising limb of high flow events (Bača 2008; Collins, 1979; Landers et al., 2013; Lawler, 2006; Mao and Carrillo, 2017). Another possible explanation for clockwise hysteresis is the sediment supply becomes limited on the receding limb of peak flow (Landers et al., 2013). The timing of baseflow (groundwater) on the receding limb diluting the

concentration of sediment within the flow may be another possible cause for lack of sediment supply (Bača 2008).

Counter-clockwise hysteresis may indicate a greater flux of sediment from tributaries during the receding limb of peak flow, upstream bank failures during the receding limb, greater distance of the sediment source, or sediment depletion within the channel (Lawler, 2006; Bača, 2008; Landers et al., 2013; Mao and Carrillo, 2017).

In alpine, glacier-fed channels, clockwise hysteresis appears to be more dominant than counter-clockwise hysteresis (Willis 1996, Sawada and Johnson, 2000, Collins, 1979; Bhutiyani, 2000; Bača, 2008), however counter-clockwise hysteresis has been observed to dominate some glacial environments (Crookshanks, 2008). Mao and Carrillo (2017) report both clockwise and counter-clockwise hysteresis, with clockwise hysteresis being reported more for the snowmelt season and counter-clockwise hysteresis dominating the glacier melt season in the Estero Morales basin, a glacier-fed river in the Chilean Andes. Sawada and Johnson (2000) reported both clockwise and counter-clockwise hysteresis on Slims River, Yukon; however, clockwise hysteresis dominated the trend and was most frequent during periods of higher glacial melt (Sawada and Johnson 2000). Bhutiyani (2000) saw clockwise hysteresis in glacial meltwater in the Himalayas. Collins (1979) saw both clockwise and counter-clockwise hysteresis in glacial meltwater from Gornergletscher Glacier located in Switzerland. In non-glaciated environments both clockwise and counter-clockwise hysteresis has been observed to occur (Walling and Webb, 1982; Klein, 1984; Lawler 2006; Landers et al., 2013).

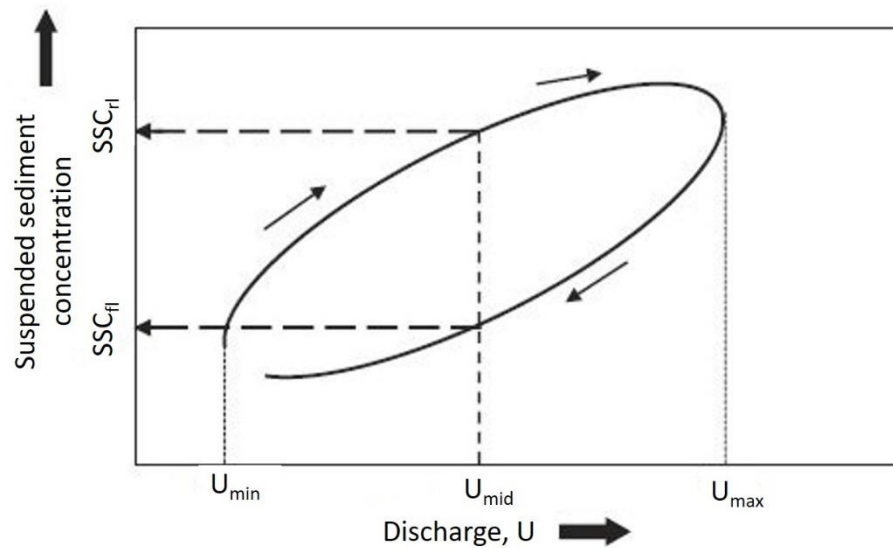


Figure 2: Clockwise hysteresis in a plot of suspended sediment concentration (SSC; here expressed as turbidity) and discharge (U). Clockwise hysteresis indicates that the peak SSC occurs before the peak U. Reproduced with permission from Elsevier under license number 4553240794473 on 20-Mar-2019 from Figure 6 on page 118 in Lawler et al. (2006): *Science of The Total Environment*, Volume 360.

Grain-size properties can also be hysteretic when compared to discharge. In unglaciated basins both types of hysteresis have been observed. Walling (2000) reported coarser sediments on the rising limb of the hydrograph and finer grains on the falling limbs in the Humber and Tweed basins in England. Landers and Sturm (2013) saw the opposite effect, which was decreasing particle sizes on the rising limb and increasing particle sizes on the falling limb in their study on the Yellow River, near Atlanta, Georgia, USA. They attributed this to finer grained particles being supply limited by transportation and larger grain particles being capacity limited by transportation.

2.2.3 Mechanics of sediment transport

There are three transport paths that sediment particles in motion in water can take: rolling, saltation, or suspension (Figure 3). Sediment rolling (or sliding) describes

transport in which sediment has continuous contact with the bed. Saltation describes transport in which sediment particle leaves the bed at a high angle ($>45^\circ$) attaining a height of only a few grain diameters before descending back to the bed at a much lower angle ($>10^\circ$). Suspension describes transport in which grains move upward with advective bursts and downwards with sweeps (Leeder, 2011). Suspension requires vertical turbulent forces to exceed the force of gravity acting on a particle (Leeder, 2011). Leeder (2011) uses these paths to differentiate three sediment transport loads: bedload (rolling and saltating transport), suspended load (suspension transport), and washload which describes the fine, 'clay-grade' particles kept in long-term suspension (suspension transport). The largest amount of sediment by volume is transported as suspended load within turbulent flow in which eddies transfer momentum and mass throughout the flow keeping sediment particles aloft (Leeder, 2011).

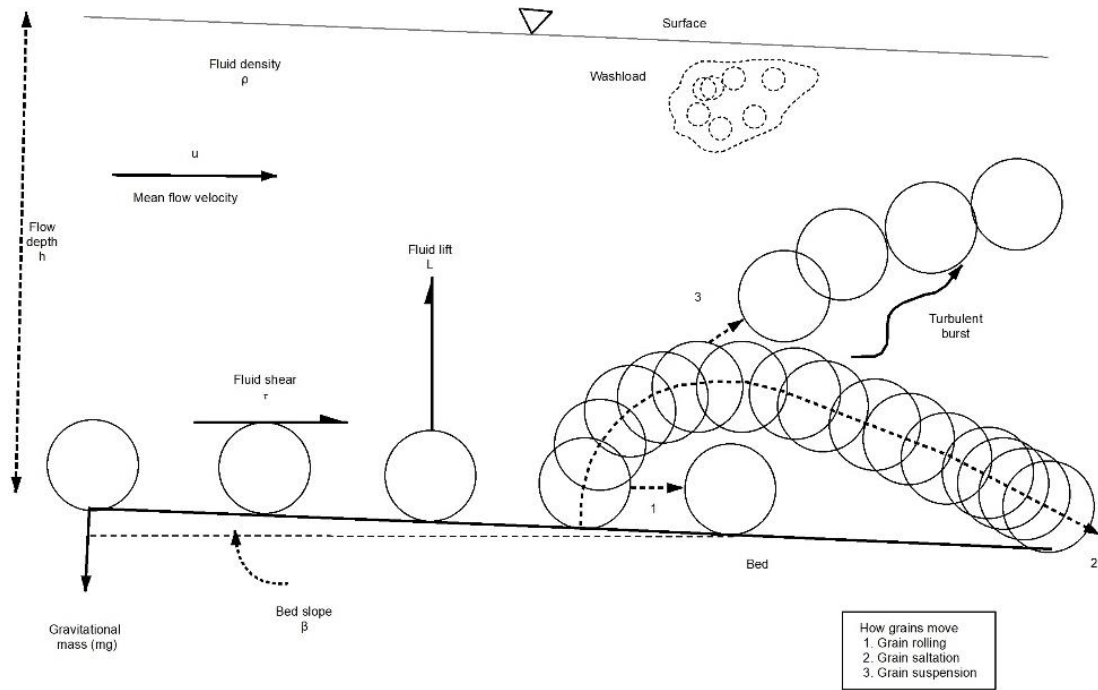


Figure 3: Sediment transport modes. Reproduced with permission from John Wiley and Sons under license number 4553240635112 on 20-Mar-2019 from Figure 6.10 on page 121 in Leeder (2011): Sedimentology and Sedimentary Basins: From Turbulence to Tectonics, 2nd Edition.

2.3 River deltas

A river delta is formed at the terminus of river inflow into standing water. Such standing water can be a lake, reservoir, slower moving river, or the ocean (Leeder, 2011). At this location, the higher-energy river water is slowed down by a decrease in channel slope and increased friction with ambient water which results in deposition of sediment at this interface. These sediments cause the delta to prograde (advance) basinward. When the river water enters a basin (e.g. lake) it is slowed down by the friction between the faster moving river water and more ambient receiving water. This reduction in flow further causes coarser-grained sediments to fall out of suspension and finer-grained sediments can continue in suspension further into the lake.

The shape and nature of deltas are controlled by many factors including: climate, fluvial discharge, sediment load, subsidence of the lake/sea floor, and river-mouth processes (e.g. tides and waves; Allaby, 2008). Deltas-forms can be classified according to variations in their transport patterns and one classification divides them into three categories: (1) river-dominated, (2) wave-dominated, (3) tide-dominated (Allaby, 2008). Deltas that are located between a river and receiving freshwater lake are often Gilbert-type deltas (Allaby, 2008). Gilbert-type deltas are river-dominated deltas that prograde into their receiving lake basin (Allaby, 2008). In alpine glacial environments, a Gilbert-type delta is the most common delta form. A Gilbert-type delta has three distinct sedimentary facies, separated by sharp contrasts in slope (Figure 4). The three sedimentary facies are the: (1) topset, (2) foreset, (3) bottomset (or “toeset”, Kleinhan, 2005; Allaby, 2008; Ferrer-Boix et al., 2015). The topset is generally thin and flat-lying (Allaby, 2008). The material of the topset is associated with fluvial transport processes (Ferrer-Boix, 2005). The foreset is the relatively steep face on a prograding delta where material from the topset can be deposited by gravity-driven mechanisms such as avalanching (Ferrer-Boix, 2015). Delta foresets often experience a downward coarsening of material, although upward coarsening has been documented in some environments (Ferrer-Boix et al., 2015). The toeset is located beneath the foreset and has a milder slope than the foreset. It is typically composed of finer-grained material that is deposited by suspension (Ferrer-Boix, 2015; Allaby, 2008). The slope of the topset is a response to external constraints (e.g. sediment supply, water depth, grain size) whereas the slope of the foreset is often near the submerged angle of repose for the material that it is made up

by (Ferrer-Boix, 2015). The foresets on Gilbert-type deltas exhibit significant changes of slope near-shore, reaching angles of 25° or more (Leeder, 2011).

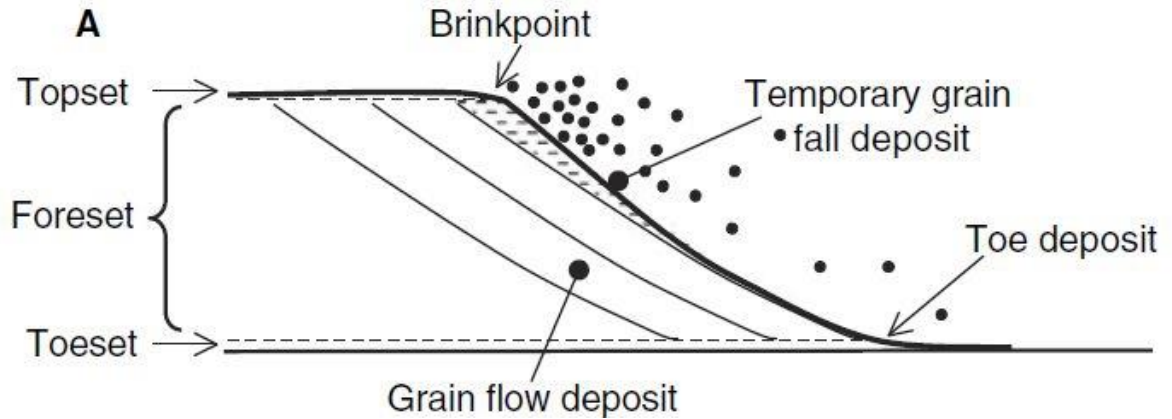


Figure 4: Sedimentary facies of a Gilbert-type delta. The topset is flat lying, separated by a sudden change of slope also known as a brinkpoint. The foreset is composed of steeper sloped sedimentary beds often developed from suspension fall-out and avalanching of material off the topset. The toeset is separated by another break in slope and forms a much flatter plain. Reproduced with permission from John Wiley and Sons under license number 4553240452683 on 20-Mar-2019 from Figure 1 on page 292 in Kleinhans (2005): *Sedimentology*, Volume 52.

2.3.1 Delta erosion and aggradation

In a classic Gilbert-type delta, foreset beds are commonly quite steep (10 to 25°) and can be controlled by the angle of repose of the sediment on it. At the top of the foreset a wedge may form, which is a result of bedload deposition. This wedge is much steeper than the average slope of the foreset and periodically collapses (Ferrer-Boix, 2015). Subaqueous delta slopes are highly unstable because of rapid sediment deposition. Sediment can be redistributed downslope by slides, slumps, debris flows, or turbidity currents (Leeder, 2011). Slope-failure-induced turbidity currents have been suspected by several authors, including those in Lake Geneva (Lambert, 1988), the 1929 Grand Bank turbidity current (Simpson, 1997), and in glacier-fed lakes like Lillooet lake (Gilbert 1975).

Given the generally high SSC in glacier-fed rivers, river deltas in these environments have been shown to be prograding, often quite rapidly (Gilbert, 1975; Slaymaker, 1991; Gilbert 2004, Crookshanks, 2008). The delta-progradation rate at Lillooet Lake is among the highest recorded in Western Canada, with only that of Slims River being higher (Slaymaker, 2017).

2.4 Lacustrine processes

2.4.1 Thermal stratification

Many glacier-fed lakes are seasonally stratified (Gilbert, 1975; Smith, 1978). Stratification typically begins in spring during a period known as spring turnover. Before this, during winter months, lakes are often isothermal. Isothermal lakes can circulate vertically due to forces from wind and water currents, facilitated by isothermal conditions and the weak or absent density stratification. Summer brings increased sensible heat transfer from the atmosphere and increased solar fluxes and associated solar heating (Wetzel, 2011), which warms the surface waters. As the temperature of the surface water is increased, its density decreases resulting in an increase in the relative thermal resistance to mixing with the colder waters below (Wetzel, 2011). The result is the thermal stratification of a lake. Figure 5 shows a classic example of lake stratification with each strata (layer) labeled. The uppermost layer, the epilimnion, is characterized as being warmer and consequently less dense than those layers below. The surface water, due to wind- and current-induced mixing is also the most turbulent layer. Below the epilimnion is the metalimnion, a transitional zone characterized by an abrupt change in temperature (Wetzel; 2011). The hypolimnion, found below the metalimnion, contains

water at the lowest temperature and correspondingly greatest density, near 4°C, in the water column (Wetzel, 2011).

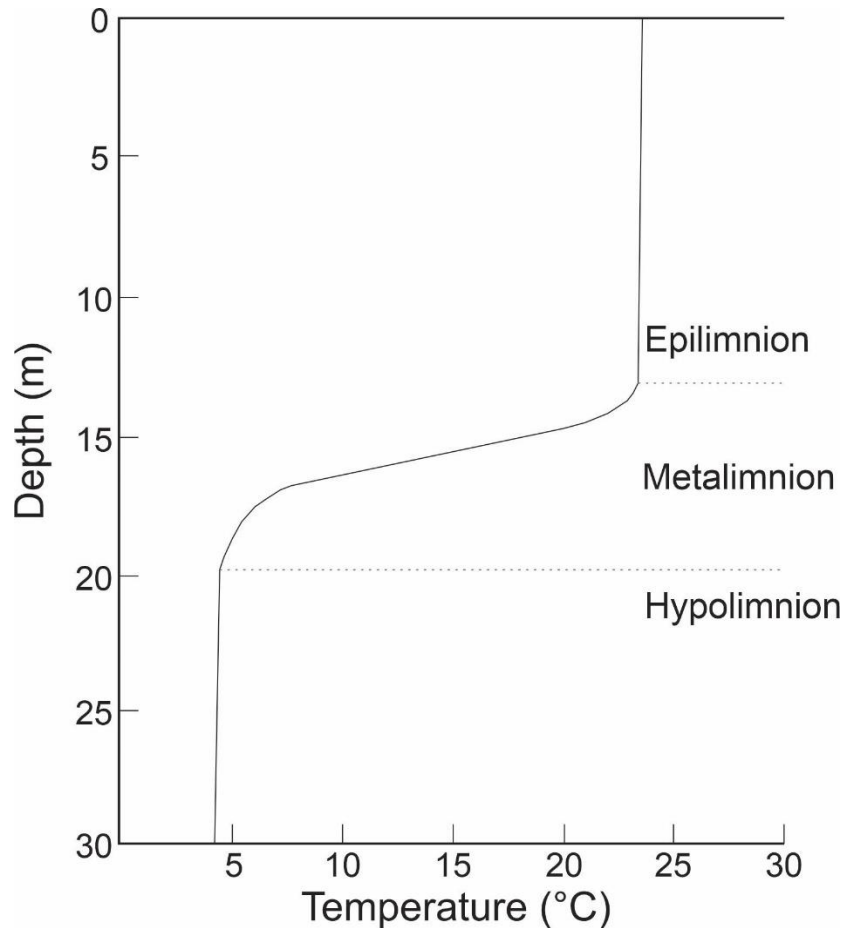


Figure 5: Theoretical plot showing the thermal stratification of a lake. The figure shows three strata including the uppermost epilimnion, the transitional metalimnion, and the bottom-most hypolimnion.

Stratification breaks down during autumn as the summer heat fades and, along with it, the resistance to mixing in water. Turbulent circulation begins to occur as the surface waters become cooler than the metalimnion layer below. Circulation continues to cool the epilimnion and thermal stratification breaks down when the lake becomes isothermal, known as fall turnover (Wetzel, 2011). Colder surface temperatures can eventually produce ice on the lake surface, and reverse stratification can occur in winter with temperature gradients at or below 0°C (at surface) and at or near 4°C at depth

(Wetzel, 2011). Reverse stratification during winter is weak compared to stratification that occurs during the summer season.

Holomictic lakes are those that are isothermal at least once per year whereas meromictic lakes have layers that never intermix (Lewis 1983). Lillooet Lake is an example of a monomictic or dimictic lake (Gilbert 1975); stratification regularly develops in the summer and breaks down in the fall (monomixis), but only in unusually cold winters does reverse stratification result in the lake being weakly stratified during these months (e.g. dimictic; Gilbert, 1975).

River inflow can disrupt the stratification of lakes. In Meziadin Lake, BC., it was found that the lake remained isothermal at the proximal (inflow) end, and weakly stratified at the distal end throughout the year of study (Gilbert, 2004). Meziadin Lake remained isothermal at the proximal end due to the inflow of river water disrupting the stratification process (Gilbert, 2004). In Lillooet Lake, Gilbert (1975) reported a temporarily high inflow from Lillooet River that caused a disruption to the hypolimnion. Warm interflowing and underflowing turbidity currents from Lillooet River mixed and flushed cold hypolimnion water away from this end of the lake. After several days, the thermal structure was re-established as river inflow returned to normal and cold water from the distal basin replenished the warmer turbid water (Gilbert, 1975).

At the interface between two lake strata turbulence can occur which causes mixing. This turbulent mixing happens at the interface of separate layers and can be caused by even minute differences in current velocity. Turbulence occurs because shear forces become greater than buoyant forces, resulting in the formation of eddies at the

boundary (Wetzel, 2011). The amount of turbulence at these boundaries (ratio of buoyant to shear forces) can be expressed by the Richardson number (R_i):

$$R_i = \frac{g(\delta\rho_f/\delta z_f)}{\rho_f(\delta u_f/\delta z_f)^2} \quad (5)$$

Where g is acceleration due to gravity (9.81 m/s^2), ρ_f is density of the current, u_f is velocity, z_f is depth (Wetzel, 2011). An R_i of 0.25 represents the boundary between stable and unstable flow at a shear zone (Wetzel, 2011). $R_i < 0.25$ results in turbulent transport that carries particles away from the direction of flow at right angles.

2.4.2 The Coriolis Force

The Coriolis Force is the apparent deflection right in the northern hemisphere and to the left in the southern hemisphere which is caused by the rotation of earth on its axis (Simpson, 1997). The Coriolis force, acting on a body, is proportional to the speed of the body and the angular velocity of earth (Simpson, 1997). A measurement of the Coriolis force is the Rossby number (Ro). The Rossby Number is a dimensionless number that describes the importance of inertial to rotating forces within a rotating flow (Simpson, 1997). The Rossby Number (Ro) can be defined as:

$$Ro = \frac{\bar{U}}{fL} \quad (6)$$

Where \bar{U} is the depth averaged current velocity, L is the length scale, f is the Coriolis frequency which can be described as:

$$f = 2\Omega\sin\theta \quad (7)$$

Where Ω is the Earth's rotation rate and θ is latitude (Wells, 2007). When $Ro \gg 1$ the effects of Coriolis are insignificant. As Ro approaches 1 the effects become more significant and as $Ro < 1$ the effects of rotation are the dominant force (Simpson, 1997).

The Coriolis force can influence lake currents and sedimentation patterns within lakes. The deflection right, in the northern hemisphere, is relative to the direction of the current, either by wind or inflowing river water. It has also been shown that in a stratified lake setting, higher density water collects on the left side, whereas less dense water collects on the right side (Wetzel, 2011). The effect of the earth's rotation can be neglected in rapid small-scale flows where $Ro \gg 1$ and becomes more significant when Ro approaches 1. When $Ro < 1$ the effects of rotation become dominant within the body of flow (Simpson, 1997).

2.5 Turbidity currents

2.5.1 Classification of turbidity currents

Turbidity currents are a type of density current that flows as a result of the density difference caused by the dispersed sediment entrained within the current and the ambient receiving water (Simpson, 1997; Allaby, 2008). The density differential causes the currents to plunge below the surface of the ambient water and flow as a cohesive current below the surface. By doing so, turbidity currents transport their entraining sediment and water into deeper regions of lakes, reservoirs, or oceans. Turbidity currents may be formed by either the unconstrained release of sediment from a slope or by the inflow of sediment-laden river water into ambient water (Lambert and Giovanoli, 1988). When river water plunges below the surface of ambient water it carries with it suspended sediment entrained in turbulence. Deposition of sediment from suspension will occur as the turbidity current velocity decreases.

Turbidity currents are generated by different mechanisms and have been classified accordingly. Turbidity currents that are generated by riverine inflow have been termed quasi-steady turbidity currents (Mulder and Alexander, 2001). They are termed quasi-steady because their source of flow, river inflow, can persist for several weeks to months at a time with little or no interruption to the current (Mulder and Alexander, 2001). Turbidity currents can also be surge or surge-like, a mechanism believed to be rare in comparison (Mulder and Alexander, 2001). Surge or surge-like turbidity currents are caused by rapid mass movements, such as with landslides or slumping (Kneller and Buckee, 2000). The Grand Banks (Newfoundland) turbidity current in 1929 was caused by an earthquake and estimated to have delivered as much as 100 km^3 of sediment into the deep ocean (Simpson, 1997). Surge-like turbidity currents can be caused by retrogressive failures of delta foreset beds (Mulder and Alexander, 2001). These failures are induced by flood conditions that mobilize the sediment at the delta front (Mulder and Alexander, 2001). As the delta front becomes over-steepened it fails, causing a collapse of sediment that can form a turbidity current to run out into the deeper basin.

Inflowing river water does not typically need a significant density differential to plunge below a lakes surface (Mulder and Alexander, 2001). In contrast, when river water enters a marine environment it typically requires a sediment concentration of about $36\text{-}44 \text{ g l}^{-1}$ for plunging flow to occur because of the much greater density of seawater relative to freshwater ($\sim 30 \text{ g l}^{-1}$; Mulder and Alexander, 2001; Boehrer and Schultze, 2008).

Turbidity currents are defined as having an upper sediment concentration of 9% by volume (Mulder and Alexander, 2001). A volume sediment concentration of 9%

corresponds to the Bagnold limit of turbulent suspension, where above 9% sediment concentration, fluid turbulence can no longer support the particles in the flow alone. By this classification, turbidity currents are maintained largely by the upward component of fluid turbulence (Mulder and Alexander, 2001). There is a limit to the competence of turbidity currents and they typically cannot transport coarse sand or gravel over long distances without the aid of gravity acting on a slope (Mulder and Alexander, 2001).

There are other types of density currents that entrain suspended sediment including concentrated density flows, debris flows, and mud flows (Mulder and Alexander, 2001). Excess density caused by sediment is also not the only type of density current. Plunging flow can also be initiated by the density differences caused by temperature or dissolved solids (Akiyama and Stefan, 1984; Simpson, 1997; Fer et al., 2001). This puts turbidity currents on a wide spectrum of density currents.

2.5.1 Examples of turbidity currents

Turbidity currents have been observed in different environments around the world. They have been known to occur in glacial lakes (Crookshanks and Gilbert, 2008), non-glacial lakes (Normark and Dickson, 1976), submarine fans (Chough and Hesse, 1976), marine fjords (Hay, 1987), and man-made reservoirs (Chikita, 1989). The focus of this study is on quasi-steady inflowing turbidity currents in glacial lakes. But for comparison, turbidity currents from other environments including marine environments will be discussed.

Turbidity currents may form as either interflows or underflows. An interflowing turbidity current is a current that flows between two water layers in a stratified water

column. An interflow can only form in stratified lakes (e.g. see discussion above) where the density of the turbidity current lies somewhere between the density of the hypolimnion and that of the epilimnion (Gilbert, 1981; Boehrer and Schultze, 2008; Wetzel, 2011). An underflowing turbidity current is a current that flows below the hypolimnion and travels along the bottom of the basin. Underflows may occur in both stratified or unstratified lakes, the only condition is their density is greater than that of the entire water column.

Lake sedimentation rates can show signs of turbidity current passage. In Silt Lake, Schiefer and Gilbert (2008) found sedimentation rates responded to changes in runoff, flood events, and intra-lake turbidity currents (Schiefer and Gilbert, 2008). Desloges (1994) found evidence of rhythmic lamination between runoff-generated turbidity currents and settling by suspension in three small alpine lakes of British Columbia. It was found that turbidity currents dominated early summer-time deposition rates and that late-summer to winter deposition was dominated by sediments settling from suspension (Desloges, 1994).

2.5.2 Plunging inflow

When the density of inflowing river water is greater than the density of ambient water, plunging of the inflowing water occurs (Akiyama and Stefan, 1984). Plunging occurs at a location known as the plunge line (or plunge point). The plunge line is the transition point from homogenous open channel flow to entrained flow (Figure 6; Akiyama and Stefan, 1984). At the plunge line inflowing river water pushes on the ambient water until a balance of forces is met. This is the position that inflowing river water sinks below the surface of ambient lake water (Akiyama and Stefan, 1984; Lee and

Yu, 1997). The plunge point on a steep slope ($S > 1:150$ or 0.38°) is a function of mixing with the surrounding water as well as the densimetric Froude number of the turbidity current (Akiyama and Stefan, 1984). At this location, mixing of river inflow and ambient water occurs (Akiyama and Stefan, 1984). This mixing causes a reduced density of the sediment plume. Mixing of a turbidity current can occur for two reasons. First, entrainment of ambient water due to instabilities at the interface between the current and ambient water. Second, at the plunge point due to abrupt changes in flow depth, which is most noticeable on a steep-sloped surface where flow becomes supercritical (Akiyama and Stefan, 1984). Plunging flow on a steep slope will become supercritical due to the acceleration due to gravity on the slope (Akiyama and Stefan, 1984).

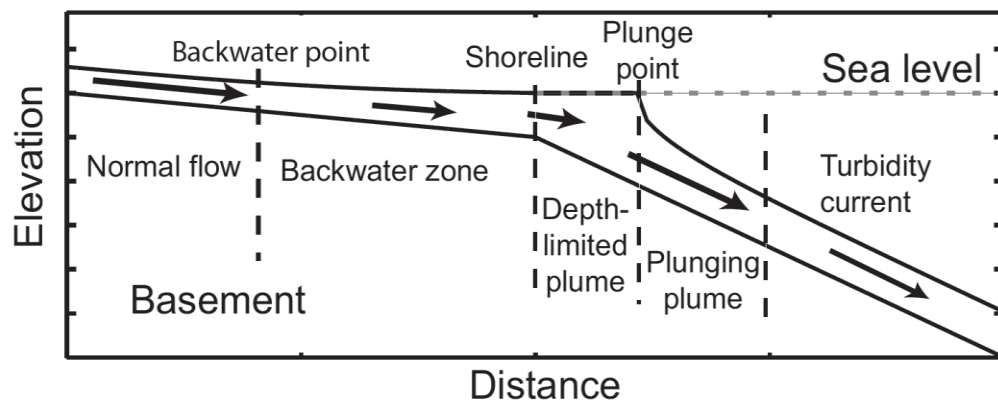


Figure 6: Diagram showing the stages of turbidity current development. The turbidity current moves from open water flow in a river channel to a plunge point where the slope break occurs. The flow plunges below the surface at this point and move down the slope as an undercurrent. Reproduced with permission from Geological Society of America under their special “fair-use” license agreement from Figure 2 on page 1068 in Lamb and Mohrig (2009): Geology, Volume 37.

For a river-generated sediment plume to plunge and form a turbidity current two conditions must be met (Lamb et al., 2010). The first is the concentration of sediment in the plume must exceed a threshold concentration in order to generate an excess of density

and the second is that the location of the plunge position must be deep enough for plunging to occur (Lamb et al., 2010). The threshold concentration C_c for plunging to occur may be calculated by:

$$C_c = \frac{1}{R} \left(\frac{\rho_a}{\rho_w} - 1 \right) \quad (8)$$

Where ρ_a is the density of the ambient fluid, ρ_w is the density of fresh water, and R is the submerged specific density of sediment (Lamb et al. 2010). The value of R can be obtained from the formula:

$$R = \frac{\rho_s - \rho_w}{\rho_w} \quad (9)$$

Where ρ_s is the density of sediments (Lamb et al. 2010). The second condition that must be met is that water must be deep enough for the flow to become unstable and begin to plunge. The necessary depth for plunging, h_p , may be found by the formula:

$$h_p = \left(\frac{q_p^2}{(\delta\rho/\rho_a)gF_{dp}^2} \right)^{1/3} \quad (10)$$

Where F_{dp} is the value of the unitless densimetric Froude number at the plunge point, q_p is the discharge at the plunge point, g is the acceleration due to gravity, and $\delta\rho$ is the excess density of the turbidity current over the density of the ambient water. The value of $\delta\rho$ is calculated as:

$$\delta\rho = \rho_w(1 + R) - \rho_a \quad (11)$$

Changes to either the sediment concentration or current velocity will result in changes to the position of the plunge point (Lamb et al. 2010). Where $F_{dp} = 0.5$ the flow can be expected to plunge (Calculation of the Froude number is shown below, Lamb et al., 2010). An increase in river discharge or a decrease in suspended sediment concentration will result in the position of the plunge line moving toward deeper water

(Lamb et al., 2010). Likewise, a decrease in river discharge and an increase in suspended sediment concentration will result in the position of the plunge line moving towards shallower waters.

2.5.3 Flow characteristics

At the interface of inflowing river water and ambient lake water, turbulent eddies are formed as ambient water is entrained into the inflowing river water (Lee and Yu, 1997). As turbidity currents continue to plunge, the interface of the flow with ambient water is subject to mixing. The mixing at these interfaces is attributed to Kelvin-Helmholtz (K-H) instabilities (Kneller, 2000). K-H instabilities are caused by shear forces acting at the boundary of two moving fluids. In the case of turbidity current flow, the turbidity current is moving through the ambient water. The K-H instabilities create vortices that help to entrain ambient fluid in the turbidity current and to detrain denser sediment laden water from the current (Kneller, 2000).

Quasi-steady currents may also have instabilities within them. These instabilities are caused by internal waves, eddies, and surges within the currents (Kneller, 2000). In the literature there have been many observations of unsteady flow characteristics or velocity pulsations within turbidity currents. Fluctuations of water turbidity and temperature have been observed on the Mississippi River Delta with a periodicity of 1 to 15 minutes, where the plume migrates both basinwards and landwards (Wiseman et al., 1976). Fer and Lemmin (2001) saw pulses of thermal currents in Lake Geneva caused by cold dense water plunging down a steep shelf. These currents with a periodicity of multiple hours were believed to be the result of long-period roll-waves. In the Katsurazawa Reservoir in Japan, unsteady, pulsing flow was observed, which the

researcher attributed to time variations of discharge, temperature, and sediment concentration from the inflowing water (Chikita, 1989). Other studies have theorized that pulsing turbidity currents may be caused by wave action, storms, tides, wind-driven circulations, unsteady river discharge, and slope failures (Best, et al., 2005). In Lillooet Lake, BC. Best et al. (2005), observed pulsing with a period of 3-12 minutes and the pulsing was observed throughout the entire body of flow. They believed that turbulence at boundary conditions and longer-period circulations cannot account for this observed phenomenon (Best et al., 2005). In Peyto Lake, Alberta, velocity pulses were observed with small minute-scale periods (Smith et al., 1980). Modelled flow in a flume box shows that the flow oscillates by 0.1 metres in the stream-wise direction with a period of 10's of seconds in response to continual mixing and collapsing of the plunge zone (Lamb et al., 2010). Still in other studies of turbidity currents velocity fluctuations were not observed (Crookshanks, 2008).

The Froude number (F) is a dimensionless number that describes the ratio of water velocity to the speed of a gravity wave (Allaby, 2008). When $F > 1$ the flow is supercritical, when $F < 1$ the flow is subcritical, and critical flow occurs when $F = 1$. The location of critical flow is important because when a flow decelerates that flow has lower competence and begins to lose suspended sediment (Mulder and Alexander, 2001). The transition point between supercritical and subcritical flow takes places at a hydraulic jump (Middleton, 1993). Hydraulic jumps occur at the boundary between two slopes and in lacustrine environment this tends to occur at the base of slopes (e.g. base of the delta foreset; Middleton, 1993). Determination of whether a flow is supercritical, subcritical, or

critical can be made by calculating the densimetric Froude number. The Froude number, F , may be calculated for a turbidity current by the equation:

$$F = \frac{\bar{U}}{\sqrt{g'd}} \quad (12)$$

Where \bar{U} is the depth averaged flow velocity, g' is the buoyancy reduced gravitational acceleration, and d is the flow thickness (Middleton, 1993). To obtain the buoyancy reduced gravitation acceleration:

$$g' = \frac{(\rho_f - \rho_a)}{\rho_a} g \quad (13)$$

Where ρ_f is the bulk density of the flow ρ_a is the density of the ambient fluid and g is acceleration due to gravity.

2.5.4 Turbidity current flow velocity and travel lengths

Turbidity currents generated in lakes have been shown to travel many kilometers from their source. A scaling up of the travel distance of a sediment particle before settling in the laboratory experiment by Lamb et al. (2010) showed that a discharge rate of $5 \text{ m}^3 \text{ s}^{-1}$ would produce an advection length of 7.5 km. Chikita et al. (1996) showed that turbidity currents generated from river inflow on Peyto Lake travelled several kilometers before ascending one side of a mid-lake sill and descending on the other side into the distal basin. Gilbert (1975) also identified sediment deposits left by underflowing turbidity currents in the distal portion of Lillooet Lake, over 10 km down-lake from the delta. An example of a marine setting, where the scale of turbidity currents is far greater than lacustrine settings, is the Grand Banks turbidity current, which is believed to have traveled for over 450 km (Simpson, 1997).

Turbidity current velocity in lakes can be low in comparison to turbidity current velocity in oceans. Velocity tends to decrease with time and distance from the source of the current (Mulder and Alexander, 2001). Marine turbidity currents have velocities on the order of $10^0 - 10^1 \text{ m s}^{-1}$ (Kneller and Buckee, 2000). In freshwater environments turbidity currents have been recorded at velocities much lower than this. In Lillooet Lake, Best et al. (2005) found turbidity current velocities reached up to 58 cm s^{-1} . Crookshanks and Gilbert (2008) found similar results in Kluane Lake, Yukon, where they observed maximum velocities to reach 60 cm s^{-1} .

It is also possible to theoretically estimate the flow velocity of turbidity currents. A simple hydraulic model, modified from the Chezy flow equation to calculate the depth-averaged mean velocity \bar{U} of turbidity currents is:

$$\bar{U} = \sqrt{\frac{8g'Sd}{f_b + f_i}} \quad (14)$$

Where S is the slope ($\sin \alpha$), d is the thickness of the current, f_b and f_i are Darcy-Weisbach friction coefficients for the lower and upper boundaries of the current, and g' is the buoyancy reduced gravitational acceleration. The Darcy-Weisbach friction coefficients may be found from the following relationships:

$$\tau_b = \frac{f_b \rho_f \bar{U}^2}{4} \quad (15)$$

$$\tau_i = \frac{f_i \rho_f \bar{U}^2}{4} \quad (16)$$

Where τ_b is the shear stress at the bottom interface of the flow and τ_i is the shear stress at the top interface of the flow (Middleton, 1993). Shear stresses for the bottom and top of flow is difficult because it requires assumptions of the friction factors where f_b is dependent on surface roughness at the bottom interface, f_i is dependent on mixing with

the above fluid (Middleton, 1993). Current velocity is then a function of the thickness of the current, slope of flow surface, and the shear forces acting at its boundaries.

Faster flows may be achieved as a result of high slopes or flows channeling within canyons (Mulder and Alexander, 2001). These flows may be supercritical. At some distance as the delta slopes decrease or sediment concentration decreases the flow will decelerate (Middleton, 1993; Mulder and Alexander, 2001). For quasi-steady turbidity currents with steady incoming flows the current may become steady, or critical with this deceleration (Middleton, 1993).

The volume of suspended sediment that is transported by rivers into lakes are quite low, relative to those entering marine environments, however, when inflowing fresh water flows into ambient fresh water a large density differential is not required for the current to plunge (Mulder and Alexander, 2001). In Kluane Lake, Crookshanks and Gilbert (2008) reported a maximum suspended sediment concentration (SSC) of 5 g l^{-1} , while typical concentrations were between 1 to 2 g l^{-1} . When the temperature and salinity of the incoming flow and ambient water are equal, the bulk density of the current is related to sediment volume concentration by the equation:

$$\rho_f = (\rho_s - \rho_a)C + \rho_a \quad (17)$$

Where ρ_f is the bulk density of the current, ρ_s is the density of the sediment grains, ρ_a is the density of the ambient fluid and C is the sediment volume concentration (Mulder and Alexander, 2001).

2.5.5 Influence of Coriolis on turbidity currents

The influence of the Coriolis force is described in detail above for lake currents. But the Coriolis force may also have an impact on turbidity currents. As described previously, the Coriolis force can be described by the Rossby Number. The Rossby Number describes the importance of inertial to rotating forces within a flowing fluid (Simpson, 1997).

For large-scale turbidity currents, the effects of Coriolis may be important. Wells (2007) showed that in marine environments, turbidity currents with runout lengths of 10's to 100's of kilometres can be influenced by Coriolis, and that has dictated the extent of the deposited turbidites. Gilbert (2004) found that higher density water within turbidity currents was directed to the right in Meziadin Lake, which the author attributed to the Coriolis force having an impact on smaller scale flows (Gilbert, 2004). Smith et al. (1980) identified Coriolis as the mechanism responsible for deflecting inflowing river plumes within the epilimnion towards the right relative to incoming flow on both Hector Lake and Bow Lake in Alberta.

2.5.6 Flow interactions with the bed

Turbidity currents are often considered a depositional process, but they can also be erosive. The erosive or depositional potential of a turbidity current is governed by the energy of the current, which as demonstrated above, is driven by flow velocity, sediment concentration, bed slope, and grain size of suspended sediments.

In the marine environment, turbidity currents leave deposits known as turbidites (Middleton, 1993). An idealized turbidite deposited by a surge-like turbidity current will

form a Bouma-Sequence (Mulder and Alexander, 2001). An idealized Bouma-Sequence has 5 divisions (A-E) listed from base to top (Leeder, 2011). The original Bouma-Sequence theory has been reworked and it is accepted that this theory no longer accounts for all the diversity that has been observed in different turbidite sedimentary deposits around the world (Middleton, 1993).

In lacustrine environments, turbidity currents often leave a noticeable depositional pattern. Where turbidity currents may dominate the accumulation of sediment in the summer, it is often small wash load-particles that dominate in the winter and shoulder seasons. This results in distinct rhythmic laminations observed in core deposits. These laminations are known as rhythmites and typically show a coupled sequence for deposits of a given year (Gilbert, 1975; Crookshanks and Gilbert 2008; Desloges, 1994).

In addition to transporting suspended sediment into the lake, turbidity currents are also capable of eroding sediments previously deposited within a lake (Middleton, 1993). Quasi-steady turbidity currents plunging into a lake have been observed to erode the bed near their plunge line (Chikita, 1989). In Lake Walensee, Sweden, the area immediately adjacent of the Linth Canal delta shows the presence of new, abandoned, and infilled channels within the bottom sediments indicating that the turbidity currents entering Lake Walensee have erosive potential (Lambert, 1976). Lambert (1988) observed that in Lake Geneva, a subaqueous slump occurred and damaged his anchored moorings. This turbidity current would undoubtedly have the potential to erode sediment if it can damage a cable mooring.

2.5.7 Measurements and parameterization

Most field studies of turbidity currents will deploy equipment that can study many different parameters that govern and affect turbidity currents. Measurements that are recorded tend to come from many different streams of data including meteorological data, hydrological data, sediment data, as well as physical properties of the lake including water temperature, specific conductivity, dissolved oxygen, lake depth, and pH.

Boehrer and Schultze (2008) maintain that meteorological variables should be considered for any investigation into the physical processes of a lake. In keeping with this, many studies do consider meteorological variables. Air temperature and wind speed/direction data are two commonly used variables when studying turbidity currents. Gilbert and Butler (2004) showed that air temperature had the most important influence on discharge rates for Meziadin Lake, which in turn led to higher rates of sediment input. Chikita et al. (1996) deployed a meteorological station at Peyto Lake (Alberta) and they showed that wind driven circulations in the lake remobilized turbidity currents into the distal lake basin (Chikita et al. 1996).

River discharge measurements are also used to study the effects and timing of turbidity currents (Ross and Gilbert, 1999; Crookshanks and Gilbert, 2008). Mulder and Alexander (2001) maintain that most of the sediment is transported during major flood events because of the relationship between SSC and discharge. Lamb and Mohrig (2009) tried to show a relationship between turbidity current deposits and river-flood dynamics from a theoretical 1-D flow model. They found that the relationship between turbidites and river discharge could be correlated, uncorrelated, or anti-correlated depending on

factors affecting incoming flow such as flow velocity and sediment concentration (Lamb and Mohrig, 2009).

Other lake currents should be taken into consideration when observing turbidity currents since these other currents can influence turbidity currents in the way they interact with them. Chikita et al. (1996) showed that wind driven currents could reactivate turbidity currents. The depth averaged velocity equation for a turbidity current (presented above) uses a Darcy-Weisbach friction coefficient for the friction with overlying water. Parameterization of the properties of the ambient lake water is important to understanding the dynamics of turbidity currents. Lake currents have been monitored in the literature using a variety of instruments including acoustic Doppler current profilers' (aDcp) (Best et al., 2005 and Kostachuk, 2005) or point-source current meters that measure both current direction and velocity (Chikita et al., 1996; Crookshanks and Gilbert, 2008; Normark and Dickson, 1976).

Suspended sediment is an important parameter to measure within a turbidity current. The suspended sediment within a turbidity current is the main factor which drives its density differential from the surrounding ambient water. Other components that can have an impact on driving density differentials include temperature and salinity. Suspended sediment is often monitored within the lake (Weirich, 1985) but can also be monitored in-stream (Lambert and Giovanoli, 1988). Suspended sediment monitoring is time consuming; therefore, many studies have used turbidity or transmissivity measurements as a proxy for suspended sediment (Gilbert, 1973; Crookshanks, 2008; Weirich, 1985). A limited number of suspended sediment data points can be collected and then related to a continuous data stream of turbidity/transmissivity measurements

(Walling and Webb, 1981). Johnson (1992) casts doubt on the quality of the SSC-turbidity relationship because other factors may be responsible for changes in turbidity other than suspended sediment. Gippel (1989) explains that variations in sediment properties, organic acids, sediment concentration, air bubbles, and turbulence can occur which will degrade the relationship between SSC and turbidity.

Water temperature is also commonly used to study turbidity currents. Water temperature influences the density of water (Boehrer and Schultze, 2008). Water is at its maximum density at 4°C and changes to the water density can cause a lake to become thermally stratified (Boehrer and Schultze, 2008). It is common that incoming river water has a different temperature from ambient lake. In a turbidity current, the incoming lake water does not mix readily with the ambient water, and the two water columns will maintain separate temperature profiles therefore, water temperature is a key measurement in the study of turbidity currents. Lambert and Giovanoli (1988) found turbidity currents to be warmer than the ambient lake water, while Schiefer and Gilbert (2008) found them to be cooler than lake water, Crookshanks and Gilbert (2008) found that turbidity currents could be either warmer or cooler depending on the diurnal temperature fluxes of the incoming river water. This variability in the contrast of temperature between river water and lake water helps to explain the importance of sediment concentration in turbidity currents.

2.6 Conclusions

Understanding turbidity currents in the natural environment is important for several reasons. Turbidity currents are the main mechanism for delivering coarse sediment further out into deeper water (Gilbert, 1975; Weirich, 1985; Crookshanks,

2008). This has the implication for infilling of lakes and reservoirs with sediment.

Turbidity currents contribute large amounts of sediment to the geological record and their deposited sediment has been used to infer past paleoflood events. In large, dynamic settings such as in the ocean, turbidity currents can be destructive by destroying submarine cables in marine environments.

Turbidity currents are highly dynamic and complex. They are driven by the differences in density between the ambient fluid and entraining fluid and may occur as interflows, if the lake is stratified, or underflows, whether the lake is stratified or unstratified. Their genesis may be from incoming river water, from sudden slumps, or other events that provide a large flush of sediment into ambient water.

Turbidity currents are challenging to sample because they can often occur in (1) remote locations and (2) in an underwater environment that requires one or more remote-sensing techniques for sampling. Notwithstanding the challenges inherent in field sampling of turbidity currents, these measurements can provide a valuable view into the natural forces at work in lacustrine environments. Many past studies have focused on laboratory studies of turbidity currents, but Francalanci et al. (2013) note that laboratory data tends to be oversimplified and can produce unrealistic results. Therefore, field studies that can adequately address the variability of turbidity currents and their interactions with their environment around them are very important to furthering our understanding of this complex process.

3 Study area

Lillooet Lake [50° 18'N, 122° 36'W] is located within the southern Coastal Mountains of British Columbia. Lillooet Lake is approximately 100 km northeast of Vancouver, BC., and situated very near the Village of Pemberton (Figure 7). It was chosen as the site for this field research for several reasons:

- Turbidity currents are known to occur in Lillooet Lake. 1
- The Lillooet River basin, in many cases including Lillooet Lake, has been the site of extensive field research campaigns that inform this work since the 1970's, with research foci that include glaciology, slope processes, river hydrology, and the limnology and sedimentology of Lillooet Lake. 2
- Lillooet Lake is readily accessible by car and by boat, whereas many other glacier-fed lakes in Western Canada are not. 3
- Lillooet Lake is located close to the City of Vancouver, where parts for field equipment can be easily obtained. 4

To help understand the research objectives (Chapter 1) the interconnections of the Lillooet River-Lake system need to be explored. Much like Chapter 2, Chapter 3 explores, in detail, the watershed-wide processes that interact to deliver water and sediment into a lake. This chapter explores these in context of Lillooet Lake by way of Lillooet-Green River delta. The follow sections document the characteristics of the Lillooet Basin from the high alpine glaciers to the observed properties of Lillooet Lake with a focus on water flow and sediment in the Lillooet-Green River as this has been the focus of most past research and this river represents by far the greatest source of flow and sediment into Lillooet Lake (Gilbert, 1975).

3.1 Upper-Lillooet Basin

The Upper-Lillooet basin which feeds Lillooet Lake, is primarily fed by three large rivers and their respective tributaries (Figure 7). These rivers are the Lillooet River, Green River, and Birkenhead River. Their gross catchment area is approximately 3,580 km² of which approximately 3,150 km² is drained by Lillooet and Green Rivers (Figure 7; Gilbert, 1975; Jordan and Slaymaker, 1991). The Green River begins in its headwaters at Green Lake, near the Resort Village of Whistler, BC. It flows into the Lillooet River (becoming the Lillooet-Green River cf. Gilbert, 1975; Barrett, 2014) and forms an alluvial fan east of the Village of Pemberton. The third largest river, the Birkenhead River, has an approximate drainage area of 430 km². This river is fed from the Birkenhead Lake near the communities of Birken, Devine, and D'Arcy, BC.

The hydroclimatology of the Lillooet Valley is influenced by a rain-shadow effect from the Pacific Ocean. Atmospheric circulation most commonly brings precipitation from the Southwest and the Lillooet Valley is aligned NW-SE and most coastal precipitation does not make it over the orographic high (Slaymaker et al., 2017). Average winter snow depths of 2-3 metres are common at mid-elevation sites in the Upper-Lillooet basin (Friele, 2004).

Lillooet Lake sits at an elevation of approximately 195 m above sea level and the upper catchment rises to over 3,000 metres in the upper alpine zones (Gilbert et al., 2006). As of 2005, 459 km² of the catchment was covered by glaciers, which is reduced from 519 km² in 1985 (Slaymaker et al., 2017). Glacier cover accounted for approximately 13% of the total basin area in 2005. The single largest glacier in the catchment is Lillooet Glacier (Schiefer and Gilbert, 2008). The snout of Lillooet Glacier

is at an elevation of approximately 950 m, and like most glaciers in this catchment and Western Canada it is receding (Gilbert, 1975; Schiefer et al., 2006).

Below Lillooet Lake, the Lower Lillooet River drains into the Little Lillooet Lake, then Harrison Lake, before finally joining the Fraser River and discharging into the Pacific Ocean on the Fraser River Delta (Slaymaker et al., 2017).

Lillooet River flows for over 100 km from Lillooet Glacier, changing from a braided and cobble-bedded stream in its upper reaches to a single-thread, sand bedded channel towards Lillooet Lake (Weatherly and Jakob, 2014). There are no major glacio-fluvial terraces that have formed along Lillooet River and thin layers of colluvium and morainal veneer have formed in places overtop of the bedrock. The bedrock of the Lillooet basin is comprised mainly of steep-sloped Mesozoic Era granitic and metamorphic rocks (Heideman, 2013; Weatherly and Jakob, 2014; Slaymaker, 2017). During the Cenozoic Era, uplift occurred throughout the basin which led to cycles of fluvial canyon down-cutting (Slaymaker 2017). Later, during the Pleistocene Epoch, the Lillooet River valley was widened and deepened by glacial action (Slaymaker, 2017). Embedded in the upper headwaters of the Lillooet River valley is a large Pleistocene-Epoch volcanic complex, known as the Mount Meager Volcanic Complex (MMVC; Heideman, 2013; Weatherly and Jakob, 2014). This volcanic complex occupies 2% of the area of the Lillooet River basin (Heideman, 2013).

Vegetation in the Lillooet River basin is diverse and represents a typically coastal-mountain environment. Coastal-mountain heather dominates the highest elevations in the basin while Mountain Hemlock occurs mainly at mid-elevations. On north facing slopes

Engelmann Spruce and Interior Douglas Fir occur, in locations where more arid conditions persist (Slaymaker, 2017).

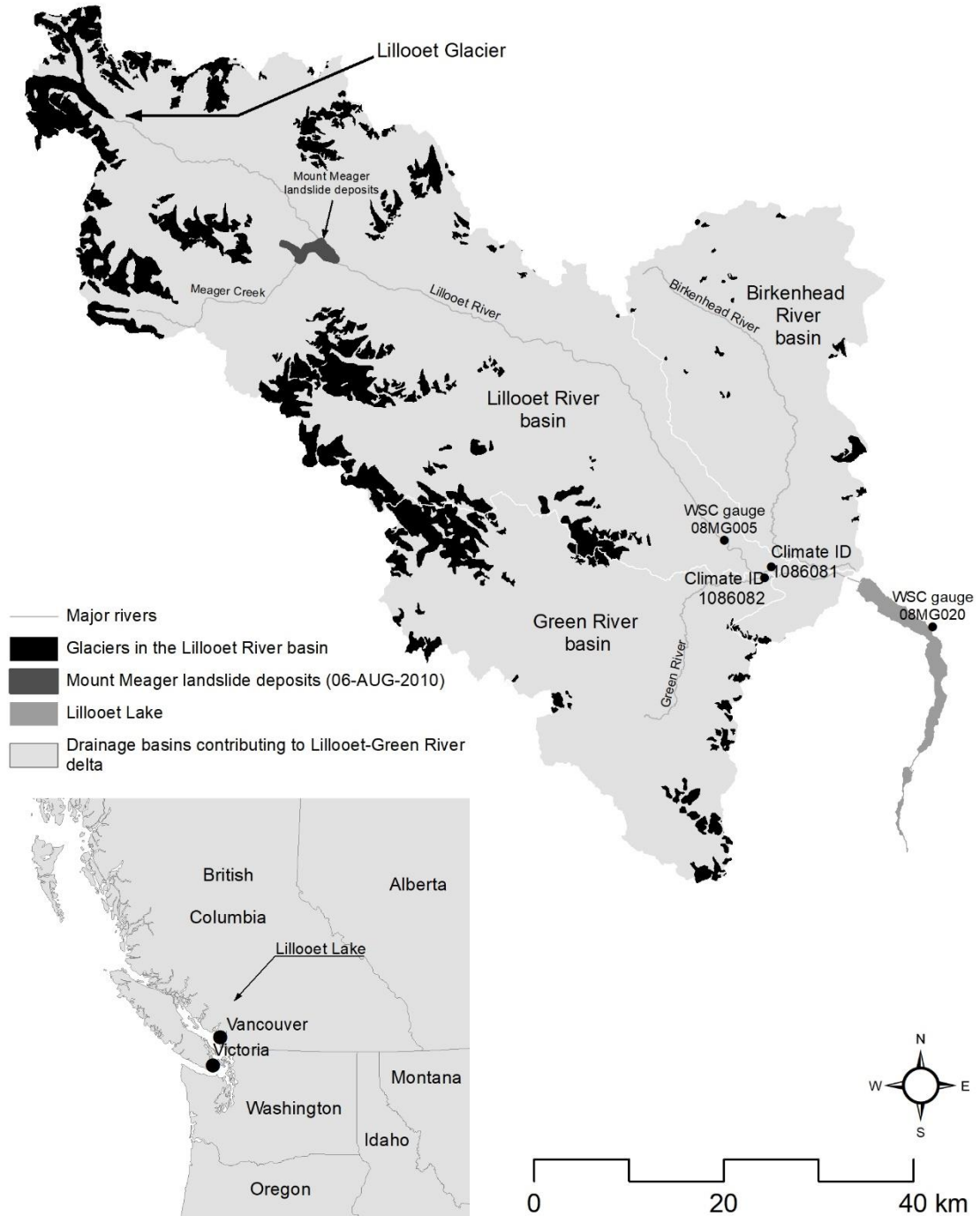


Figure 7: Location map of Lillooet Lake basin. The map shows the location of the three largest tributaries to Lillooet Lake including Lillooet River, Green River, and Birkenhead River. The map also shows the location of Lillooet Glacier. The inset map shows the location of Lillooet Lake in context of the province of British Columbia.

3.2 Lillooet Glacier

Lillooet Glacier is the largest of the valley glaciers in the Lillooet River basin (Slaymaker et al., 2017). Lillooet Glacier is responsible for the most runoff and sediment production of any of the glaciers (Slaymaker et al., 2017; Barrett and Hodder, 2018). Lillooet Glacier first drains into Silt Lake then eventually into Lillooet Lake (Schiefer and Gilbert, 2008; Barrett and Hodder, 2018). Silt Lake was formed sometime during the retreat of Lillooet Glacier between 1947-1973 and acts as a sediment trap for glacial runoff (Slaymaker et al., 2017). Silt Lake is observed to have decreased in area from 0.75 km² to 0.45 km² since 1973 due to outwash progradation into the lake from Lillooet Glacier (Slaymaker et al. 2017).

The retreat of the glacier has exposed unstable lateral moraines and glacial forefields that can be reworked by fluvial and hillslope processes, thus providing ever-increasing amounts of sediment for mobilization as the glaciers continue to retreat (Slaymaker et al., 2017).

3.3 Slopes processes

Debris flows are the dominant sediment transfer mechanism linking upland sediment sources to river channels in Lillooet River basin (Slaymaker et al. 2017). The Mount Meager Volcanic Complex is a very significant source of loose colluvium that is available for transport.

Since the increased retreat of glacial ice from the Neoglacial maximum (200-400 ybp), there has been a large increase in poorly consolidated colluvium and volcanic talus slopes that have become exposed thereby providing a huge source of sediment that is available to be mobilized (Bovis, 2000; Slaymaker et al., 2017).

Hillslope processes that act on these sediments are believed to be the major contributor to sediment in the Lillooet River. According to Slaymaker (2017), sediment from the MMVC dominates the supply of coarse clastic sediment to Lillooet River and is primarily responsible for progradation of the Lillooet-Green River delta as Lillooet River and its tributaries transport this sediment from the hillslopes to Lillooet Lake.

Historically there have been many examples of large slope movements, especially in the MMVC. These examples have been observed in both historic times and by an examination of the paleoenvironmental record. Since around 1940, it is estimated that there were at least six separate events that caused a temporary impoundment of Meager Creek, not including the 1998 and 2010 events (Bovis, 2000). Four dates (1295, 1493, 1511, and 1611) in the lake-varve record of Lillooet Lake are believed to show large-scale landslide events. Eight other anomalously thick, prehistoric varves are likely linked to large discharge events possibly associated with the MMVC (Heideman et al., 2015). In the paleoenvironmental record, a 4,400-year-old landslide from Pylon Peak in the MMVC produced a debris field that extended nearly to the site of present-day Pemberton in the Lillooet River Valley (Friele, 2004).

The MMVC is drained by Meager Creek, which flows into Lillooet River. Because Meager Creek is the preferred flow path from these large movements and slides,

it has a disproportionally high sediment load relative to its drainage area and flow (Bovis 2000; Friele, 2004).

3.3.1 2010 Mount Meager landslide

On August 6, 2010, the largest historic landslide in Canada occurred. The landslide occurred on Mount Meager in the Lillooet River basin (Guthrie et al., 2012). The accumulation of the deposits from this slide is shown in Figure 7. The landslide resulted in a debris flow carrying an estimated $48.5 \times 10^6 \text{ m}^3$ of material into the Meager Creek and Lillooet River valleys (Guthrie et al., 2012). When the landslide occurred it completely dammed Meager Creek and partially dammed the Lillooet River for 19 hours (Guthrie et al., 2012). The dam is estimated to have impounded $2.9 \times 10^6 \text{ m}^3$ of water (Guthrie et al., 2012). When Meager Creek was finally able to cut through the deposited sediment it sent a large pulse of water into the Lillooet River. This event created a flood wave that increased discharge by several hundred cubic meters per second and lasted over seven hours (Guthrie et al., 2012). The temporary dam was breached slowly enough that the resulting flood wave did not cause any damage to downstream communities (Heideman, 2013).

Since the Mount Meager landslide in 2010, it has been estimated that a significant source of sediment in the Lillooet River system are derived from Mount Meager deposits (Guthrie et al., 2012).

3.4 Lillooet River

3.4.1 Lillooet River hydrology

Lillooet River has been observed to have one peak (Eaton and Moore, 2010) or two peaks in the annual flow hydrograph (Gilbert 1973). The first peak is the nival peak, primarily associated with snowmelt in early summer. The second peak is attributed to glacial melt, which occurs later in summer. In late July and early August, glacier and snow melt reach their peak in the Lillooet river basin (Friele 2004). Lillooet River basin is also susceptible to strong autumn storms (Gilbert, 1975; Friele, 2004; Gilbert, 2006). These summer storms are responsible for producing large, prolonged rainfall events (Friele, 2004). It was during one of these storms in 2003 that the hydrometric gauge on Lillooet River recorded its record peak-flow event (Figure 9).

Most discharge into Lillooet Lake is glacially-sourced (Desloges and Gilbert, 1994; Jordan and Slaymaker 1991). Lillooet River is the main source of water, as well as sediment, entering Lillooet Lake at the delta, accounting for 86% of water inflow and 98% of suspended sediment (Gilbert, 1975).

Discharge on Lillooet River is measured by the Water Survey of Canada (WSC) stream gauge located north of the Village of Pemberton (Figure 7). The gauge (08MG005) has been active since 1914 and gaps include 1919 to 1922 and 1996. Maximum annual discharge in Lillooet River from 1914 to 2015 is shown in Figure 8. The recurrence series of annual maxima of peak daily discharge in Lillooet River is shown in Figure 9. Mean annual discharge of Lillooet River is $127.5 \text{ m}^3\text{s}^{-1}$. Lillooet River

exhibits a typical glacial river flow regime (Gilbert et al., 2006), with a peak flow in late July due to glacial melt.

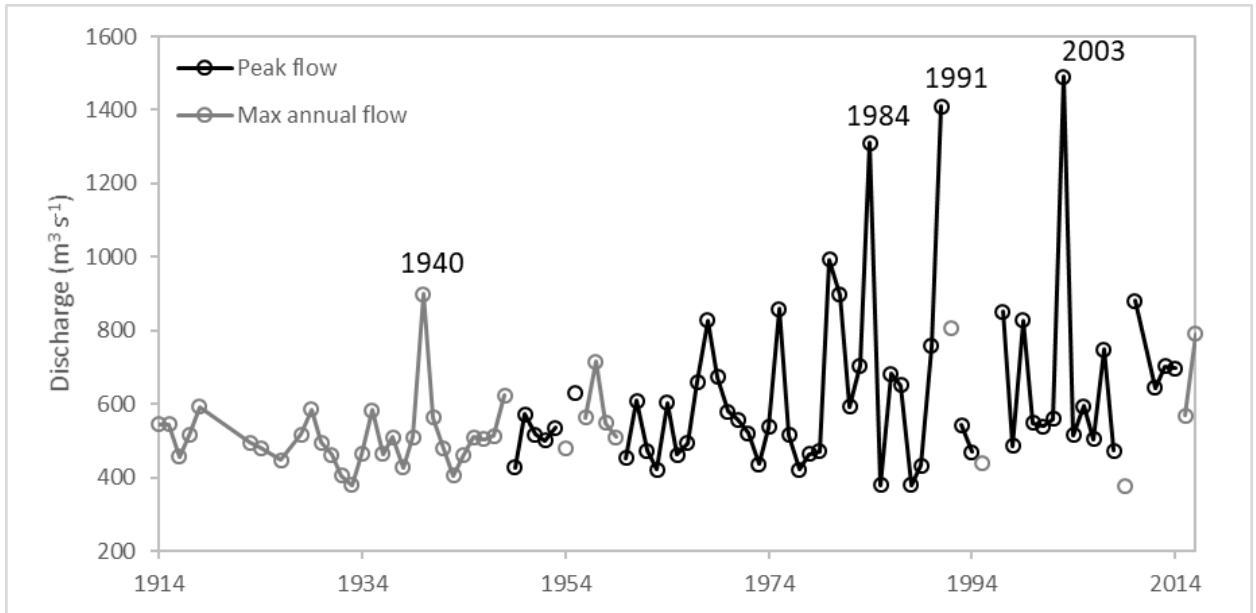


Figure 8: Peak flow for Lillooet River from 1914-2016. Black lines represent reported peak flow. Grey lines are the maximum annual flow for years where no peak flow is reported. [data source: station 08MG005, Water Survey of Canada, 2015]

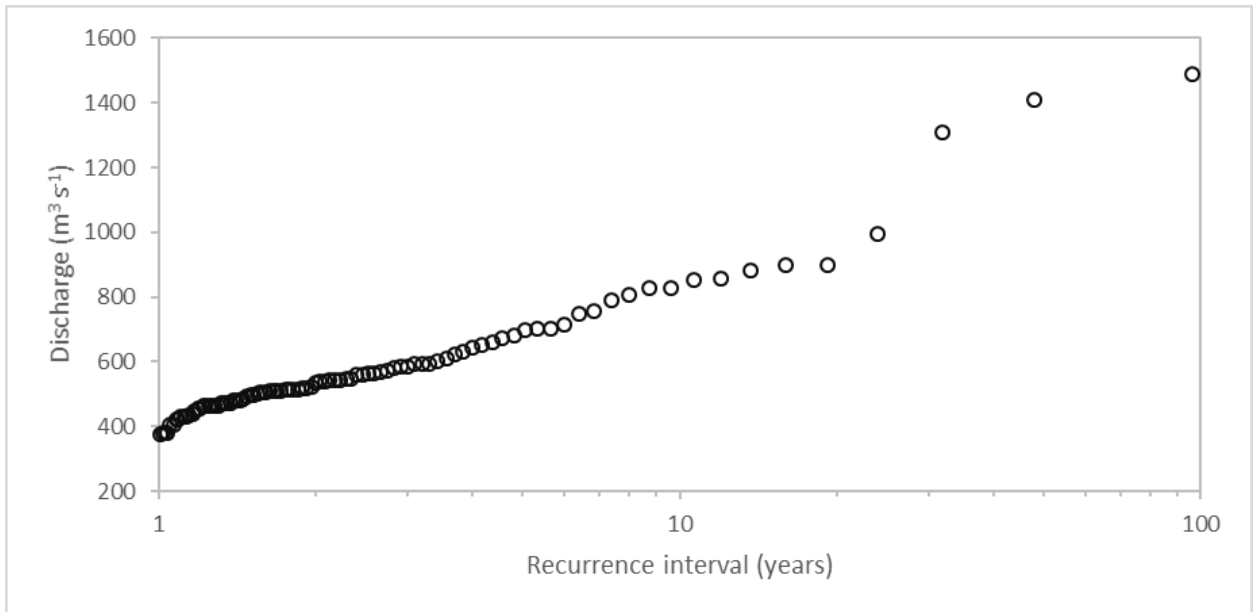


Figure 9: Recurrence series of annual instantaneous peak discharge events on Lillooet River. Data is from 1914-2016. [data source: station 08MG005, Water Survey of Canada, 2015]

The main trunk of Lillooet River is approximately 110 km from the edge of the delta to the snout of the Lillooet Glacier (2010 imagery). Approximately 77 km upstream of the delta is the MMVC, site of the 2010 Mount Meager landslide and at this location, Meager Creek enters the Lillooet River as a tributary.

The Lillooet River drains through a large variety of landscape and slope conditions. In its headwaters the river is highly braided. The slopes of the upper river channel are approximately 0.008 m m^{-1} and the channel bed is highly cobbled (Weatherly and Jakob, 2014). The slope of the lower river channel near Lillooet Lake is approximately 0.0005 m m^{-1} and the sediment environment is sand-bedded (Weatherly and Jakob, 2014). The Lillooet River valley forms a large alluvial floodplain that is 1.2 to 2 km wide in its lowest reaches (Weatherly and Jakob, 2014). Within this floodplain there is agricultural and forestry activity (Slaymaker et al., 2017). The river in this area is confined to a single channel and begins to meander, being broadly bound by the valley walls (Weatherly and Jakob, 2014). The Lillooet River maintains this characteristic meander and low slope profile until it discharges into Lillooet Lake.

3.4.2 Lillooet River suspended and dissolved sediment

As was previously mentioned, Lillooet River is responsible for the largest amount of suspended sediment that is transported into Lillooet Lake (Gilbert, 1975). SSC in Lillooet River was measured by Gilbert (1973) to be as high as $3,000 \text{ mg l}^{-1}$. River-bottom sediment samples show mean grain size ranging from $430 \text{ }\mu\text{m}$ to $2630 \text{ }\mu\text{m}$ (0.43-2.63 mm) and probably represent bedload (Gilbert, 1975).

Although the largest source of sediment entering Lillooet Lake is from Lillooet River, the origin of sediment in Lillooet River is not always clear. This is because of the competing geomorphic processes that release sediment in the Lillooet River valley above Lillooet Lake. Early studies by Gilbert (1973, 1975) concluded that Lillooet Glacier is the dominant source of sediment in Lillooet River but more recent studies by Jordan and Slaymaker (1991) and Slaymaker et al. (2017) have suggested that the MMVC and hillslope processes are likely responsible for most of the sediment in Lillooet River. Since the 2010 Mount Meager slide, it is also believed that the downcutting of these freshly laid deposits has been a major source of sediment into Lillooet Lake (Guthrie et al., 2012).

Dissolved sediments are also present in Lillooet River. From the literature, it appears that dissolved sediment in the Lillooet basin is quite low in comparison to other drainage basins. Conductivity measured in Silt Lake by Schiefer and Gilbert (2008) was only $20 \mu\text{S cm}^{-1}$. They attributed the low conductivity values to the geology within the drainage system. Crookshanks (2008) compares the conductivity of Kluane Lake to Lillooet Lake in her thesis (Crookshanks, 2008). In it she describes the conductivity of Lillooet Lake to be in the order of $35\text{-}75 \mu\text{S cm}^{-1}$ whereas Kluane Lake is $240\text{-}270 \mu\text{S cm}^{-1}$ (Crookshanks, 2008).

3.5 Lillooet-Green River Delta

The Lillooet-Green River delta is a large flat delta that extends into Lillooet Lake (Figure 10). Gilbert (1973) reported that since 1948 the delta front has been advancing $21\text{-}30 \text{ m year}^{-1}$ and that prior to 1948 mean advance was approximately $7\text{-}8 \text{ m year}^{-1}$. Based on an assessment of the Landsat image archive available from the United States Geological Survey (USGS) it appears that the delta front has advanced by approximately

650 metres between 1973 (Landsat 1 MSS) and 2015 (Landsat 8 OLI). This rate represents an advance of approximately 16 m yr⁻¹.

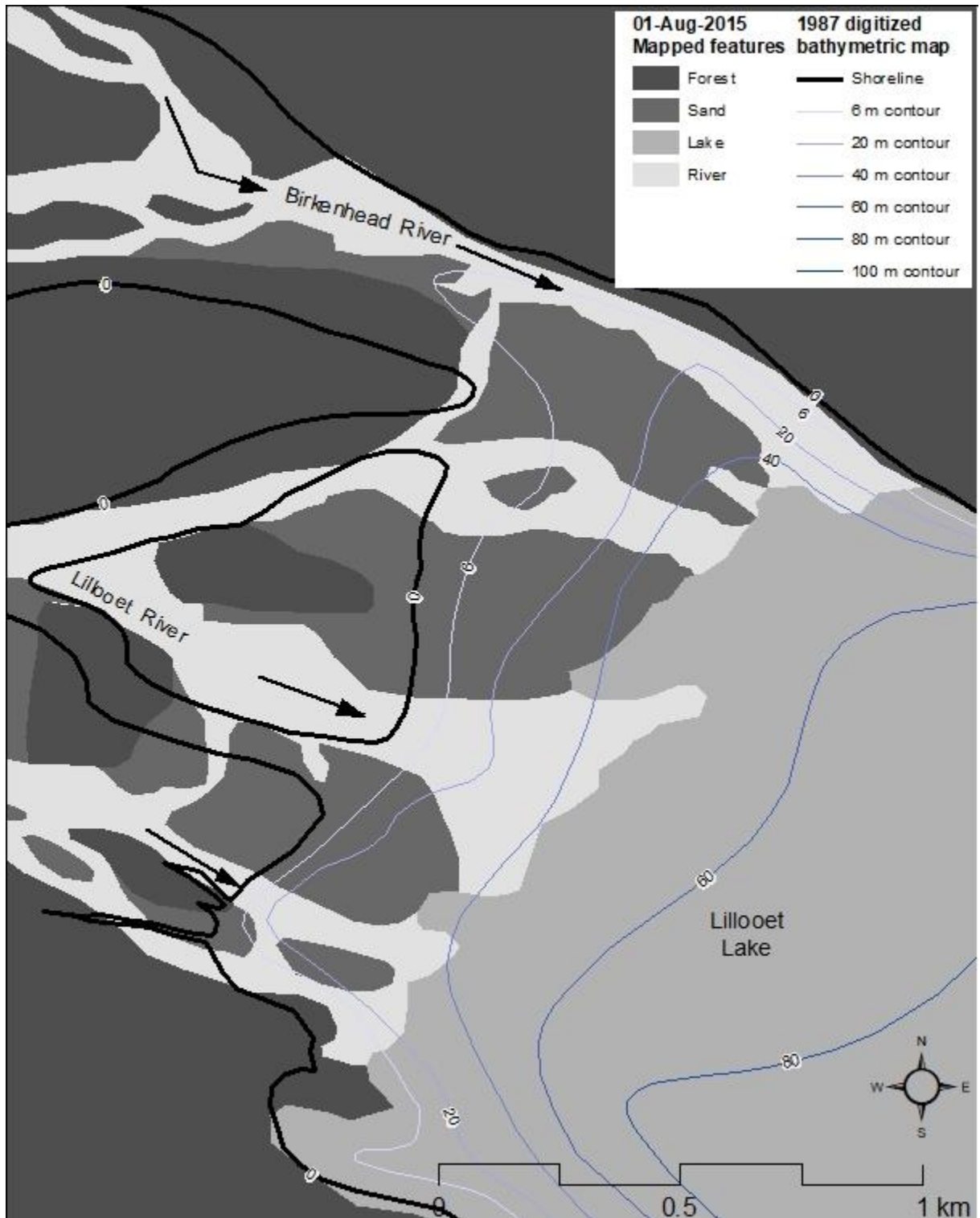


Figure 10: Map of Lillooet River, Delta, and Lake mapped from Landsat 8 OLI imagery dated 01-August-2015. The bathymetric contours are digitized from BC Ministry of Environment bathymetric map of Lillooet Lake (c. 1987). The difference in the Landsat 8 shoreline and the shoreline from the contour map shows the delta progradation that has occurred in the 28 years between 1987-2015.

Gilbert (1975) describes Lillooet-Green River delta as having classical foreset beds that extend to 8 metres depth, where the slope decreases from 8° on the foreset beds to 2° at the much flatter toeset. The surface (or topset) of the delta consists of rapidly shifting channels and sand bars. When the level of Lillooet Lake is high, backwater effects on the delta allows sediment to accumulate, which is conversely flushed away when lake levels drop (Gilbert, 1973). During low flow periods when the sand is exposed, and channels become incised, Gilbert (1973) describes that the lateral erosion of the channel banks is rapid.

Coarse-grained sediments have been observed to be deposited on the top of the delta slope as bedload. This accumulation on the delta topset results in sporadic slope failure, sending relatively large quantities of sediment out into Lillooet Lake (Gilbert, 1973).

Large mounds have been reported on foreset and toeset beds of Lillooet-Green River delta (Gilbert, 1973, 1975). These mounds are reported from 16 to 120 metres depth extending off the delta (Gilbert, 1973). Below 90 metres depth, where the bed slopes decrease to $1-2^\circ$, the mounds are observed to be larger than those above and appeared to be buried by more recently deposited sediments (Gilbert, 1973). These mounds are believed to be the product of past slumps that have occurred on the delta slopes and are the remnants of their deposits laying on the bed (Gilbert 1973). Sub-

lacustrine channels have also been reported by the sub-bottom survey of Lillooet Lake (Gilbert, 1973).

3.6 Lillooet Lake

3.6.1 Lillooet Lake morphometry

Lillooet Lake receives discharge from Lillooet-Green River, Birkenhead River, and their respective drainage areas. The lake measures approximately 22 km along the thalweg of the valley and drains via the Lower Lillooet River. Lillooet Lake was artificially lowered in 1946 by 2.5 metres which was achieved by dredging the outlet of Lillooet Lake for upstream flood protection (Heideman, 2015).

British Columbia Ministry of Environment, Fisheries Branch (BC MOE) conducted a bathymetric survey on Lillooet Lake in 1987. Morphometric statistics were compiled by the BC MOE for Lillooet Lake and are summarized in Table 2 (BC MOE, 1987) and isobaths were digitized (partially visible in Figure 10).

Table 2: Physical characteristics of Lillooet Lake based on BC MOE bathymetric map (1987)

Summary of Lillooet Lake characteristics	
Statistics at time of survey (as compiled by BC MOE)	
Lake elevation at time of survey (m)	195
Surface area (m ²)	30,440,000
Volume (m ³)	2.x10 ⁹
Mean depth (m)	75.6
Max depth (m)	128
Perimeter of shoreline (m)	52,200

Gilbert (1975) sounded the lake bottom and reported a maximum depth of 137 m. This is slightly deeper than that reported by BC MOE (1987) but still in line with the general depth trend of the lake. In addition to the major tributaries that deliver water and sediment to the main delta front there are several tributaries that enter Lillooet Lake and

deliver smaller amounts of water and sediment to the lake. Many of these tributaries are quite small and can be identified by alluvial fans that have been developed in valley crests along the banks of the lake.

The lake basin is divided into two distinct sub-basins, a proximal basin and a distal basin. The proximal basin extends from the delta to approximately where Lizzie Creek enters the lake. At this location the depth of the basin decreases from 128 m to 40 m. This is located 15 km from the front of the delta. The distal basin begins at this point and increases in depth to approximately 105 m, 19 km from the delta front. The distal basin extends all the way to the outflow of Lillooet Lake.

3.6.2 Hydrometric lake levels

The Water Survey of Canada operates a gauge (08MG020) on Lillooet Lake to monitor lake level. The gauge has been present on Lillooet Lake since 1971 (gap: 1996) and has monitored lake levels on a near-continuous basis since. Lake level recorded by this gauge is based on an assumed datum that has never been corrected to geodetic control (L. Campo, WSC technician, personal communication, 30-July-2018). Lillooet Lake was lowered by 2.5 metres from its natural level in 1946, before the hydrometric records start. Therefore, there is no period of hydrometric record that captures the pre-disturbed level of Lillooet Lake. Figure 11 shows the daily hydrograph and duration curve for Lillooet Lake (08MG020) from the hydrometric record (1971-2016). Levels fluctuate by as much as 5.6 metres on Lillooet Lake (Figure 11).

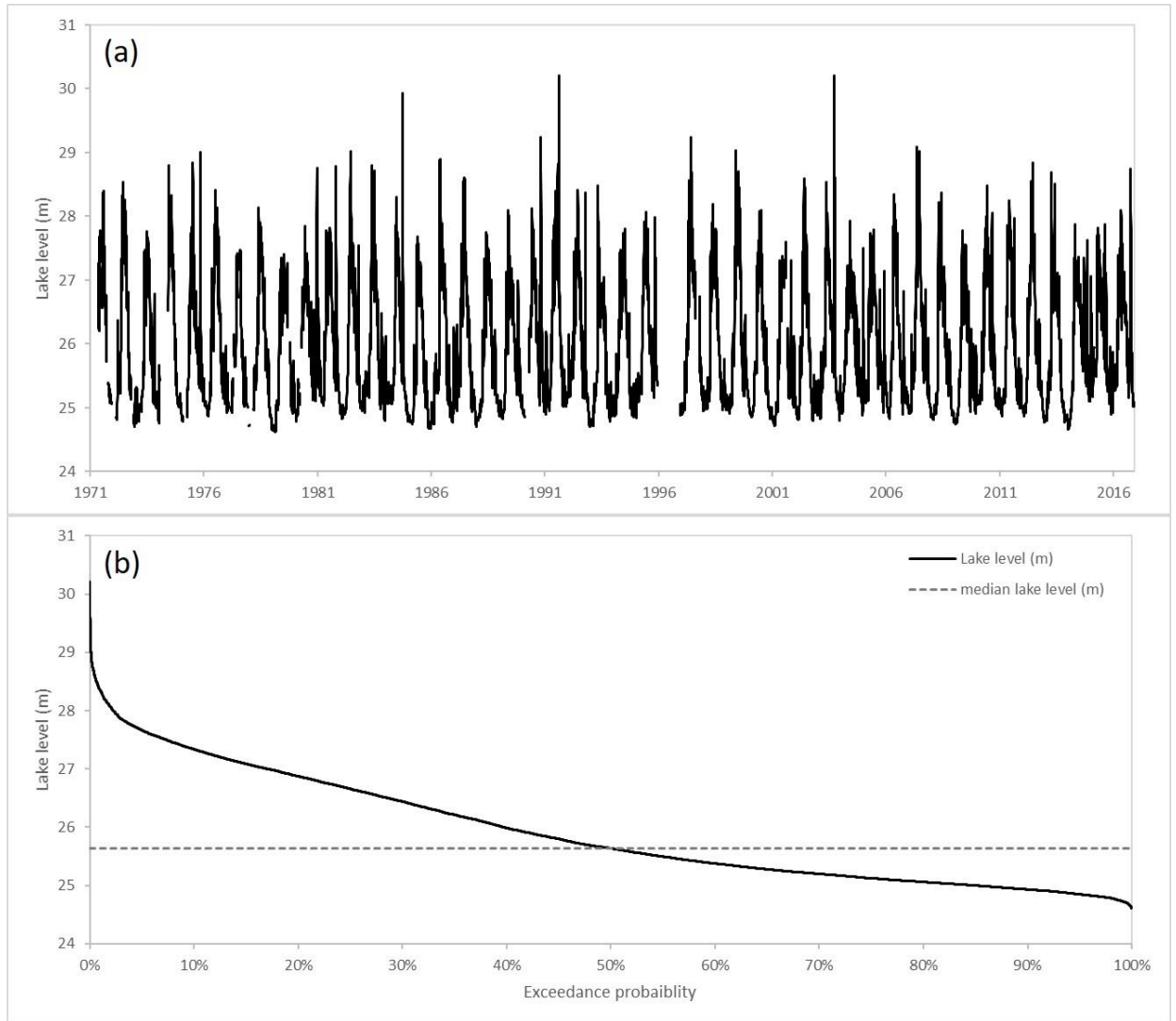


Figure 11: Lillooet Lake water levels recorded from 1971 to 2016 reported by the Water Survey of Canada gauge 08MG020. Panel (a) shows the daily lake level from 1971-2016. Panel (b) shows the duration curve for daily water levels. The median water level in the lake is 25.63 metres, shown by the dotted line. Water levels are recorded to an assumed datum and have not been referenced to a geodetic datum.

3.6.3 Lillooet Lake thermal stratification

Lillooet Lake is either a monomictic lake (if it does not freeze) or a dimictic lake (if it freezes, Gilbert, 1975). Gilbert (1975; Figure 12) reported that the structure of the lake forms three distinct layers. The lake is thermally stratified, when the upper layer (epilimnion) is approximately 10 to 13°C in summer and when the bottom-most layer

(hypolimnion) is colder than 6°C (Gilbert, 1975). These two layers are separated by a middle-layer (metalimnion) which Gilbert (1975) found to be less than 10 m thick and exist approximately 40 m below the surface of the lake. Thermal mixing of Lillooet Lake can occur because of powerful inflow or from the onset of autumn cyclonic storms (Gilbert, 1975). The lake will exist isothermally over winter until warmer inflow reinitiates thermal stratification in the spring (Gilbert, 1975).

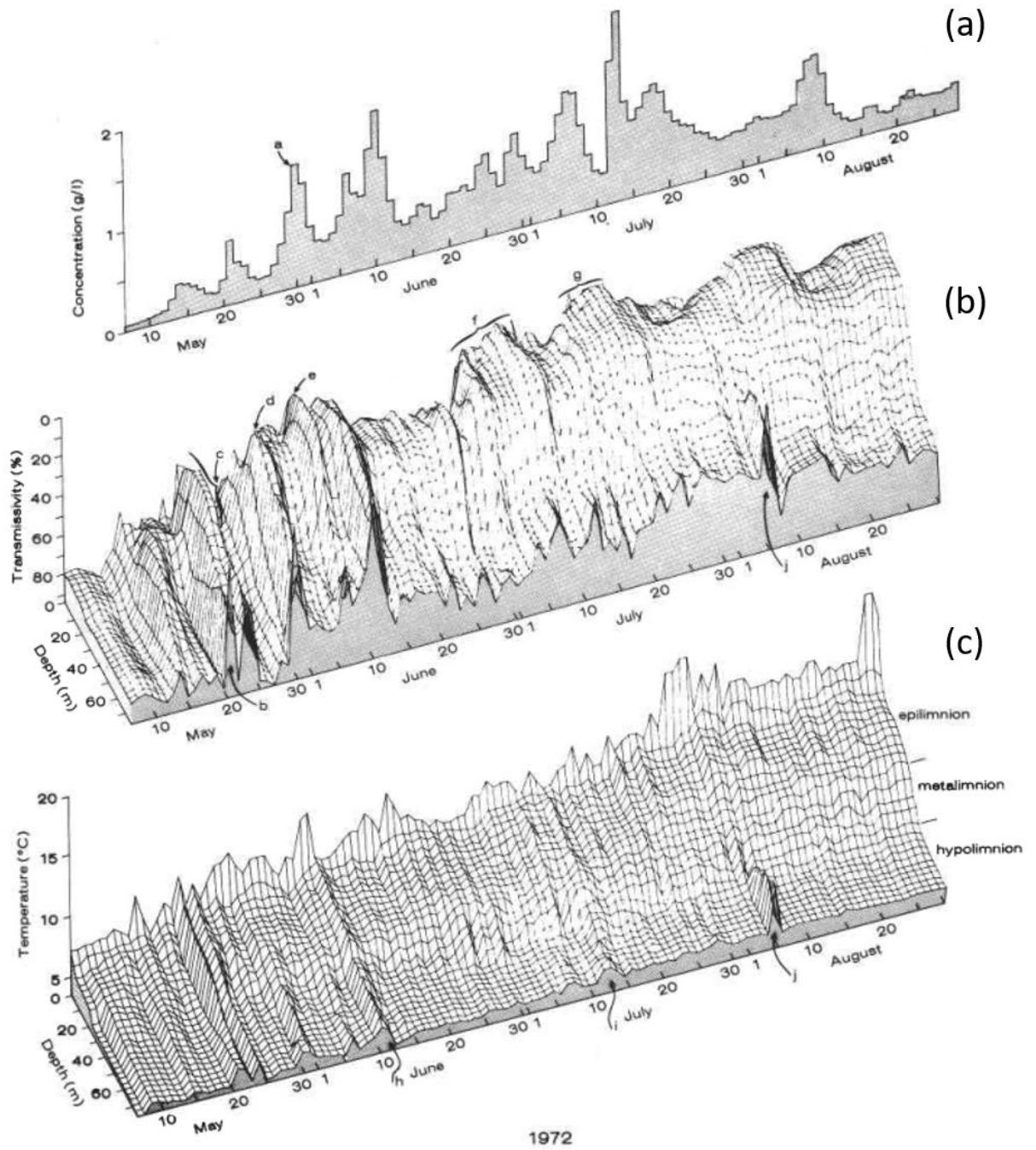


Figure 12: Panel (a): SSC in Lillooet River compared to (b) lake water temperature and (c) lake transmissivity measured in the lake 1 km from the delta. Reproduced with permission from Canadian Science Publishing under license number 4553230551874 on 20-Mar-2019 from Figure 6 on page 1702 in Gilbert (1975): Canadian Journal of Earth Sciences, Volume 12.

3.6.4 Character of sediment in Lillooet Lake

SSC in Lillooet Lake is quite high. The lake itself takes on a milky-green colour and the water is not translucent, owing to the small clay particles carried in suspension. SSC measured by Gilbert (1975) in Lillooet lake was as high as 800 mg l^{-1} . The grainsize distribution of bottom sediments in the deltaic region varied from 7.1 to $70 \mu\text{m}$, decreasing in size distally from the delta (Gilbert, 1975). Kostachuk (2005) recorded grain size within turbidity currents in Lillooet lake and found that the D_{50} grainsize was below 30 decreasing with height from the bed. Rates of sediment accumulation in Lillooet Lake throughout the Holocene are much larger than most other lakes in the Canadian Cordillera, except for that of Kluane Lake, YK (Slaymaker et al. 2017). Around 5% of the clastic sediment in Lillooet Lake is transferred to Harrison Lake as washload (Slaymaker et al. 2017). One mechanism for some of these fine particles falling out of suspension is the flocculation (or aggregation) of those particles within Lillooet Lake (Hodder and Gilbert, 2007; Slaymaker et al., 2017).

Turbidity currents are a prominent feature of Lillooet Lake and have been the focus of several studies throughout the years (Best et al., 2005; Kostachuk, 2005; Gilbert 1973; Gilbert, 1975, Gilbert et al., 2006). During summer, when river discharge is usually at its highest, Lillooet-Green River plunges below the surface of Lillooet Lake (Gilbert, 1975). When turbidity currents plunge below the surface of Lillooet Lake, they are not constrained as either underflows or interflows (Best et al., 2005). Turbidity currents have been observed to plunge as underflows to approximately $35\text{-}40$ metres depth before becoming buoyant and flowing along the surface of the metalimnion (Kostachuk, 2005). Overflowing river water has been most commonly observed to occur during winter when

lake water temperature was close to 4°C and inflowing SSC values were low (Gilbert, 1975).

The use of an aDcp on Lillooet Lake has shown that when river water plunges below Lillooet lake there is strong mixing observed at the interface of these two water masses (Best et al., 2005). Kostachuk (2005) also reported a strong counter-current directed towards the Lillooet-Green River delta in the upper water column in compensation of the inflowing river water.

4 Methodology

In order to achieve the research objectives that were set out in Chapter 1, a field monitoring program was established at Lillooet Lake to measure the environmental variables associated with the development and passage of turbidity currents. From the discussion presented in Chapter 2, turbidity currents are formed because of the excess density of river water due to increased suspended sediment concentration. This river water may plunge below the surface of a lake depending on the thermal and chemical characteristics of the lake relative to the inflow. Because of these interconnections, many variables were studied from within Lillooet-Green River and Lillooet Lake that help support the research. As has been suggested in previous monitoring studies the most important data streams for this line of study include inflowing sediment, inflowing discharge, density of inflowing water, vertical density stratification of lake water, and bathymetry of the lake basin (Smith et al., 1980). Several streams of field data were collected over the period from July 22-31, 2015 at Lillooet Lake. The types of data that were collected are shown in Figure 13 and the locations of the fixed monitoring sites used in this study are shown on Figure 14.

The following sections in this chapter describe the methodology that was employed to collect and process the data for analysis and interpretation.

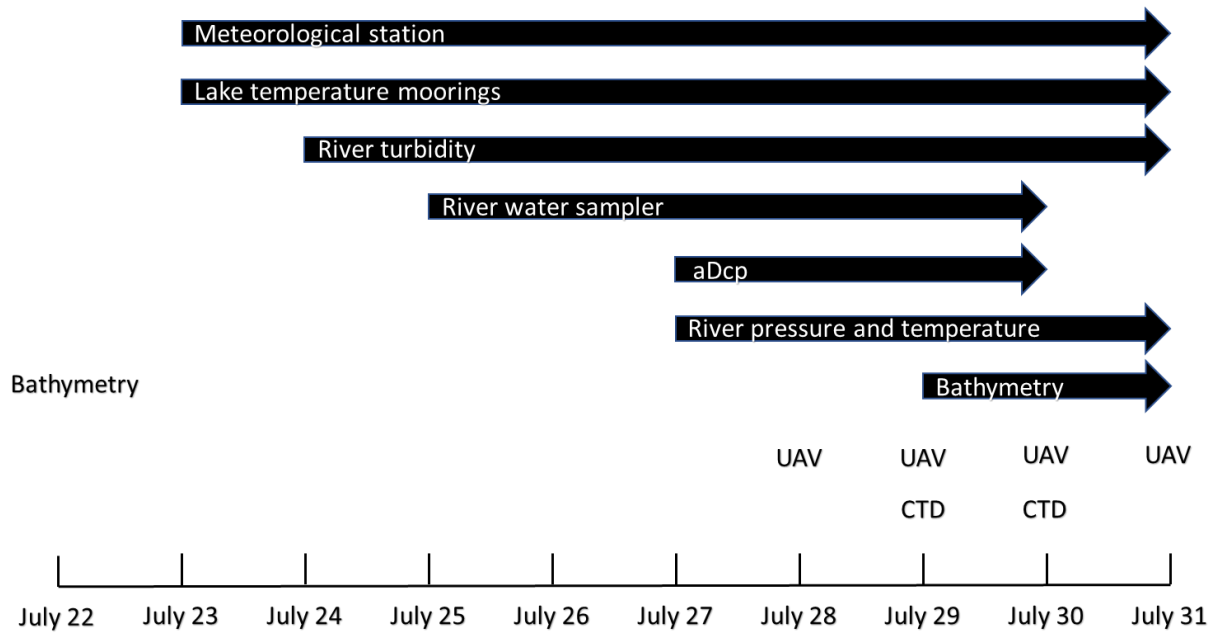


Figure 13: Flow chart showing equipment deployments in Lillooet Lake during the 2015 field campaign. Field data was collected for 9 days from 22-July to 31-July-2015. Due to the remoteness of the field site and small inflatable boat only a limited amount of equipment could be deployed or retrieved each day.

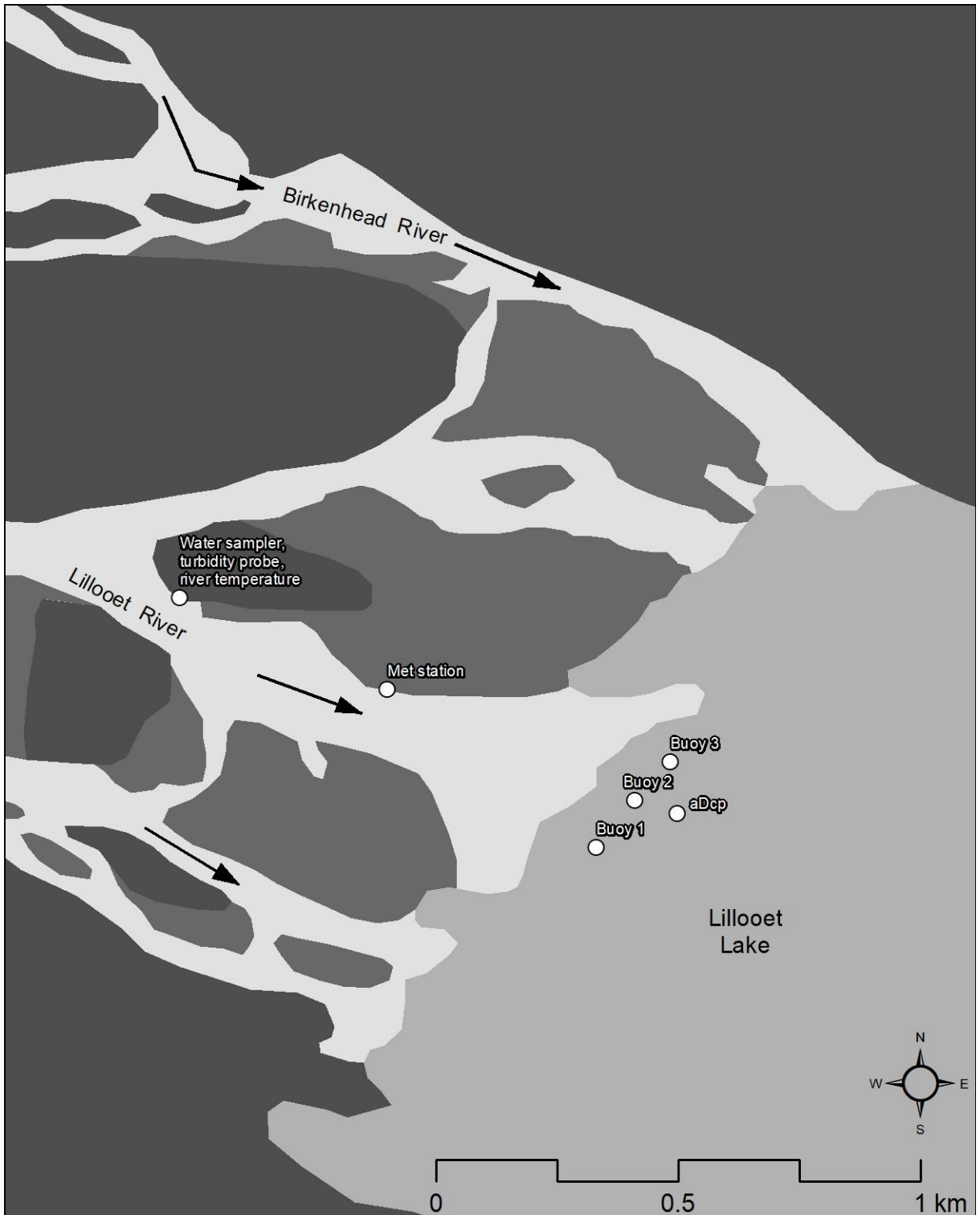


Figure 14: Map showing the fixed equipment deployments at the Lillooet-Green River delta. The Buoys and aDcp were moored at the bottom of the lake with anchors and attached to floats at the surface for retrieval. The background mapping was done manually from Landsat OLI imagery from 01-August-2015 (© USGS).

4.1 Meteorology

Three sources for meteorological data were used in this study. Data from two meteorological stations located at the Pemberton airport were used including air temperature, precipitation, and barometric pressure (Climate ID: 1086082) and wind speed/direction (Climate ID: 1086081). In addition to these MSC stations, an Onset meteorological station was assembled on the Lillooet-Green River delta to record barometric pressure, wind speed and direction, and Solar Radiation with a pyranometer (W m^{-2}). The Onset meteorological station was initially set up on the Lillooet-Green River delta on 23-July-2015. Due to the rapid rate of lateral erosion of the channel banks the station had to be moved by 5 metres on 29-July-2015 to a new location away from the eroding bank on the river. No further concerns for the safety of the meteorological station arose after this time.

4.2 River stage and suspended sediment

To measure suspended sediment in Lillooet River, a Star Log turbidity probe was deployed alongside an Onset pressure and temperature sensor and Teledyne ISCO 6712 automatic water sampler. The instruments were placed immediately adjacent to each other upstream on the Lillooet-Green River delta and fixed to permanent vegetation (Figure 14). Measurement of these parameters in the Lillooet-Green River provides values for sediment transported by Lillooet-Green Rivers and provides a comparison for previous studies of Lillooet Lake where suspended sediment and river discharge were monitored in the river (Gilbert 1973, 1975).

An Onset pressure sensor was used to estimate changes in river stage using the formula $P_s = \rho_a g h$, where P_s is submerged pressure, ρ_a is water density, and h is the height of water above the sensor (depth). Rearranging the above formula for height:

$$h = \frac{\rho_a g}{P_s} \quad (18)$$

For the above formula to work correctly, it must be corrected for atmospheric pressure. This was achieved by converting absolute pressure (P_r) to submerged pressure (P_s) by accounting for atmospheric pressure (P_a):

$$P_s = P_r - P_a \quad (19)$$

The Onset pressure sensor also recorded river temperature, which from previous studies, was expected to be cooler than Lillooet Lake water (Best et al., 2005).

The ISCO water sampler ran for four days (July 25-27 and July 28-30) and collected water samples near the turbidity and pressure/temperature probes. The turbidity probe ran from July 24 to July 31 and the pressure sensor ran from July 27 to July 31 due to missing parts at the beginning of the monitoring cycle.

The ISCO water sampler collected a 1-litre water sample every two hours over the course of 96 hours. In total, 48 samples were collected that represent a range of flow and sediment conditions. In the laboratory, the water samples were analyzed using a desktop LISST (laser in-situ scattering and transmissometry) and a vacuum weighing/filtering method to determine the mass concentration of sediment particles (mg l^{-1} ; method described below). The turbidity probe was used to collect a continuous record of turbidity every 30 seconds. To compare the relationship between turbidity and SSC, instantaneous turbidity and 10-minute averaged turbidity readings were compared to sediment concentration, shown in Figure 15. Water samples with suspended sediment were

processed in three ways to identify that which provided the best relationship with turbidity. The first level of processing (level 1) was by diluting the sample 4:1, the second level of processing (level 2) was a combination of dilution (4:1) and placing the water sample in a sonic bath for 15 seconds to disaggregate flocculated particles, and the third level of processing (level 3) was a combination of dilution (4:1), using a sonic bath, then disaggregating the sample further by using sodium hexametaphosphate (SHMP) using the method described by Folk (1980).

Water samples that were processed at level 2 (Figure 15 c,d) provided the best results when compared to turbidity values. Dilution was required because the SSC was too high and obscured the LISST's field of view. Using SHMP to disaggregate the sediment showed the weakest relationship between concentration and turbidity of all the methods employed. Values that were averaged over a 10-minute period showed better results than instantaneous readings, therefore the time-series of turbidity was transformed into a running 10-minute average before being converted to SSC.

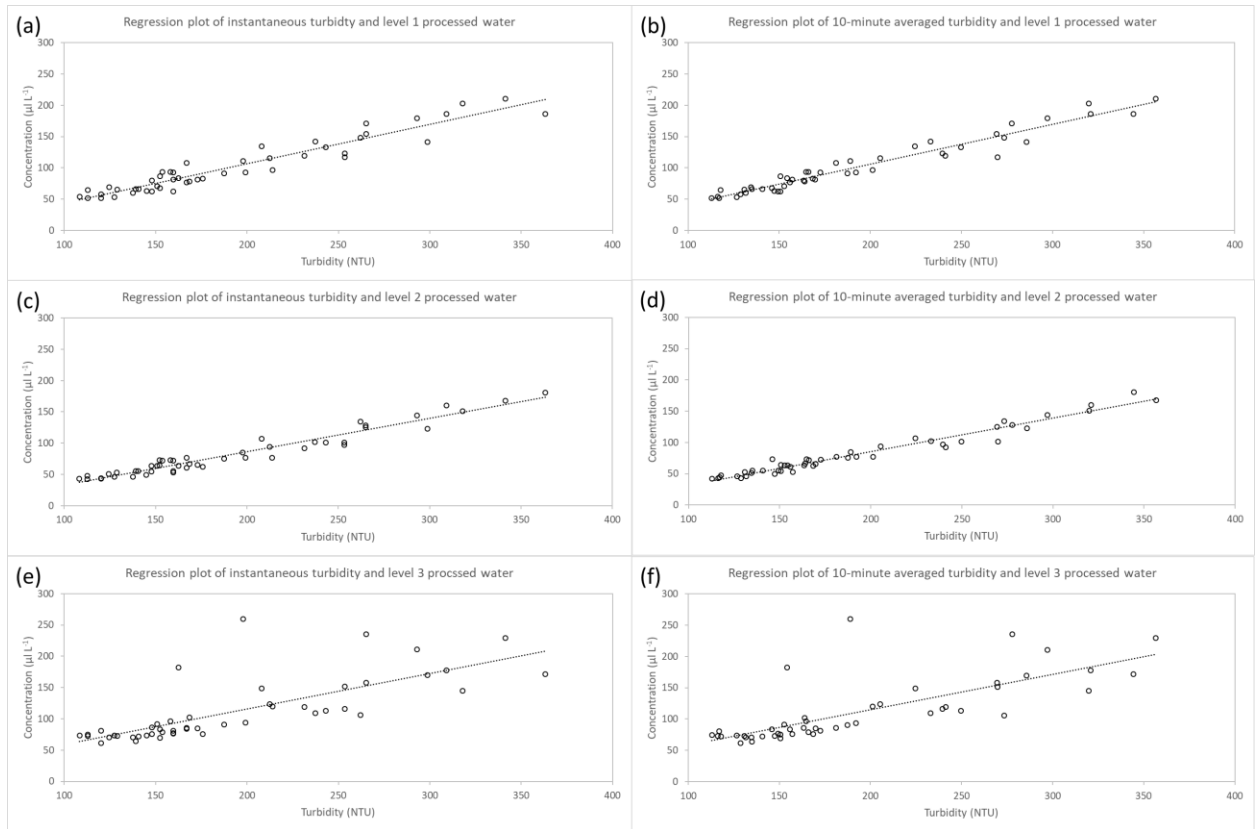


Figure 15: An example of the SSC - Turbidity rating curves used to evaluate the processing of water samples taken during this study. Panel (a) shows instantaneous turbidity measurements compared to level-1 processed water. Panel (b) shows 10-minute averaged turbidity measurements compared to level-1 processed water. Panel (c) shows instantaneous turbidity measurements compared to level-2 processed water. Panel (d) shows 10-minute averaged turbidity measurements compared to level-1 processed water. Panel (e) shows instantaneous turbidity measurements compared to level-3 processed water. Panel (f) shows 10-minute averaged turbidity measurements compared to level-1 processed water. The samples that were diluted and submerged in a sonic bath [level-2 processing, panels (c) and (d)] showed the best relationship to turbidity measurements.

4.2.1 LISST desktop analysis

A Sequoia Scientific LISST was used to analyze the water samples for volume concentration and particle-size distribution. The LISST was used in a desktop configuration to analyze the water samples returned from the field. The LISST is capable of measuring volume concentration of suspended sediment in the water ($\mu\text{l l}^{-1}$) as well as grain-size fractions over 32 logarithmically-spaced bins (Hodder, 2009). Undiluted

samples fouled the sensor. Water samples were then diluted 4:1 (distilled water to water sample) and re-run. Samples were analyzed three times, with each run adding an additional step of sediment processing. The first run only involved diluting the sample by 4:1, the second run introduced an ultrasonic bath that the sample sat in for 15 seconds, in the third run a deflocculant, sodium hexametaphosphate (SHMP), was added to disaggregate the sediment particles (Folk, 1980).

Following the collection of particle-size distribution and volume concentration of suspended sediment, 8 samples were chosen for calculation of mass concentration. Only 8 samples were chosen because this process involves destructive sampling. The results of one sample were flawed due to spillage, leaving only 7 samples for analysis. The conversion to mass concentration involved pre-weighing Millipore 0.45 μm membrane filters in the laboratory and then using a vacuum pump to pull a pre-measured volume of sample through the filter membranes. Filter membranes were dried for at least 48-hours in petri dishes at +22°C before being weighed a second time. The difference in weight represented the dry mass of sediment per unit volume of sample (mg l^{-1}). A comparison of the mass concentration to turbidity time series yielded a strong positive correlation (Chapter 5). Following this step, particle density was estimated by taking the sample mass concentration divided by the volume concentration for each sample.

4.3 Delta front monitoring

To measure the changes in water properties of inflowing turbidity currents, several equipment deployments were made in Lillooet Lake. Water temperature moorings, an aDcp, lake water profiles, UAV imagery, and bathymetric surveys were collected throughout the study period.

4.3.1 Water temperature moorings

In the lake, off the front of the delta, three temperature moorings were deployed (Figure 14). On each mooring, three water temperature sensors (Onset HOBO U22-001) were arranged along its length. As noted by Best et al. (2005), water temperature of Lillooet River can be distinctly cooler than that of Lillooet Lake.

The mooring lengths were 30 metres long to account for depth changes known to occur in Lillooet Lake (range: 5.6 m). The bottom sensor was mounted 2 metres above the bottom of the mooring, the middle sensor was mounted 10 metres above the bottom, and the top sensor was mounted 25 metres above the bottom. The moorings were attached approximately 25 metres in front of the active plunge line in water 21-25 metres deep. There were three moorings spaced approximately 100 metres apart, laterally at the delta front (each containing 3 sensors along its depth). The moorings were kept from moving by being anchored into the sediment and attached to a float. To account for possible changes in the lake level, the moorings were made longer than required so that they could not float away or become submerged should Lillooet Lake levels fluctuate. Recordings were made every 30 seconds from July 23-31. Buoy 3 was snagged by a large tree trunk in suspension sometime between 16:00 on 24-July-2015 and 16:00 25-July-2015 at which time it was unhooked and reset.

4.3.2 Acoustic Doppler Current Profiler

The aDcp was deployed on 27-July-2015 and only kept in the water for 5 days due to inclement weather and logistical challenges of transporting it to the delta. The model of aDcp used is a Sontek Argonaut XR mounted to an upward facing Sea Spider

platform. The aDcp measured total water depth, current velocity and current direction from the bottom of the lake looking upward. The aDcp can measure current velocity in 10 “bins” or cells. Previous research using aDcp’s in Lillooet Lake determined that turbidity currents were found in the bottommost 20 metres of water (Best et al., 2005; Kostachuk et al., 2005); the decision was made to only measure the bottom 20 metres of water using higher resolution cells. The higher resolution cells were chosen to measure the internal structure of passing turbidity currents with higher resolution to visualize internal flow structures. The 10 cells were set to record at 2-metre intervals from the top of the Sea Spider, which was 0.5 m in height (the aDcp also has a blanking distance from 0.5-1.0 metres). Therefore, the cell midpoints for each bin above the bed were: 2, 4, 6, 8, 10, 12, 14, 16, 18, and 20 metres. These cell distances would then enable the aDcp to view the current profiles between 1-21 metres above the bed of Lillooet Lake (Figure 16). The aDcp was deployed in 31 metres of water on the dates of deployment.

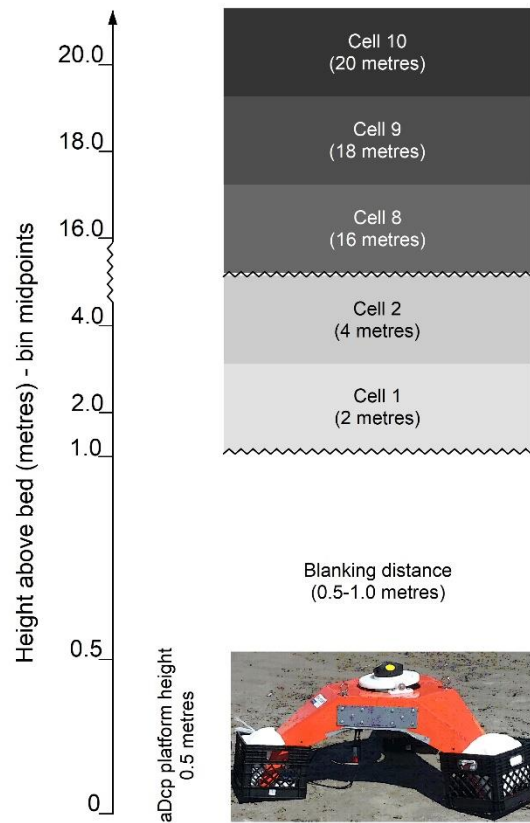


Figure 16: Deployment diagram of the setup of the aDcp mounted on the Sea Spider platform. Each bin records a 2-metre high column of water above the aDcp. The total field-of-view of the 10 bins on the aDcp is 1 to 21 metres above the lake bed.

4.3.3 Water column profiles

Vertical profiles of the water column were taken at several locations throughout Lillooet Lake on 29-July-2015 and 30-July-2015 using a YSI 6600 V2-4. The sonde was deployed over the side of the boat to provide vertical profiles at point locations throughout the lake (Figure 17). At several of these locations water samples were taken using a remote sampling device. These samples were taken to the lab to relate turbidity measurements to suspended sediment concentration (SSC). The sonde was lowered on a rope until it impacted the bottom of the lake before being retrieved. Data collected after

impact showed a large spike in turbidity. The data from the descending profile was used over the data from the ascending profile due to the fouling of the probes during almost every cast. The deployment locations were recorded with a Garmin GPS. The sonde recorded depth below water surface and the physical water parameters were related to depth. Physical water parameters used in this study included water temperature ($^{\circ}\text{C}$), specific conductance ($\mu\text{S cm}^{-1}$), salinity (PSU), and turbidity (NTU), water density was calculated from these parameters to show the “bulk water density” throughout the water column (Lewis, 1980; Chapter 5).

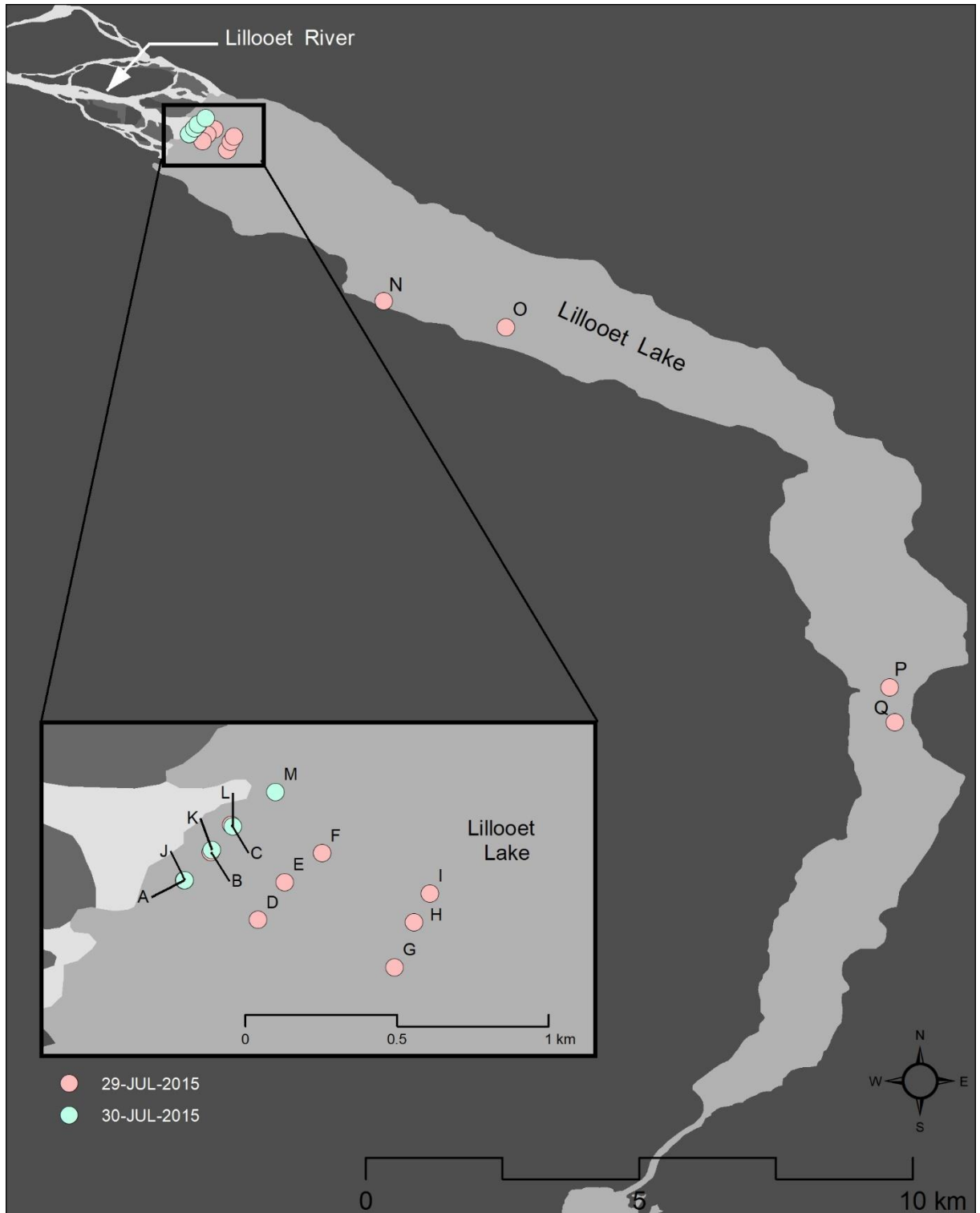


Figure 17: Location for water profiles that were collected on July 29 and July 30, 2015.

4.3.4 Bathymetric data

Bathymetric data was collected with a Garmin EchoMAP 42dv depth sounder, which was mounted to the transom of the inflatable boat alongside the data logger. The data logger used an internal GPS receiver to record location.

Bathymetric data was collected throughout several days at the front of the delta and several locations distally (Figure 18 for the area of bathymetric data collection). The depth sounder recorded points every 2-3 metres in the along-track orientation, however the spacing between transects was often quite wide, on the order of several hundred metres. For each day that bathymetric data was collected it was corrected using known lake levels from the WSC hydrometric gauge on Lillooet Lake (08MG020) to eliminate bias due to changes of lake level. Bathymetric elevations were normalized to 22-July-2015 lake level. A geodetic benchmark has not been established for Lillooet Lake (L. Campo, WSC technician, personal communication, 30-July-2018).

4.4 UAV surveys

An Unmanned Aerial Vehicle (UAV) was deployed to collect imagery and video of the delta. The UAV that was used was a DJI Phantom 2 Vision Plus. The UAV captured several days' worth of imagery and video that could be used to create orthomosaics as well as to provide a unique view of the deltaic environment.

Orthomosaic photos were processed using Agisoft Photoscan Professional 1.4.4. Control points were captured on the delta to register the images to each other. A Garmin 62S was used to collect the control data. To align the photos, all images were georeferenced to a single reference image. This allowed for a more accurate comparison

because of the lack of accuracy of the Garmin GPS (± 3 metres reported). Figure 18 shows the location of the UAV study area.

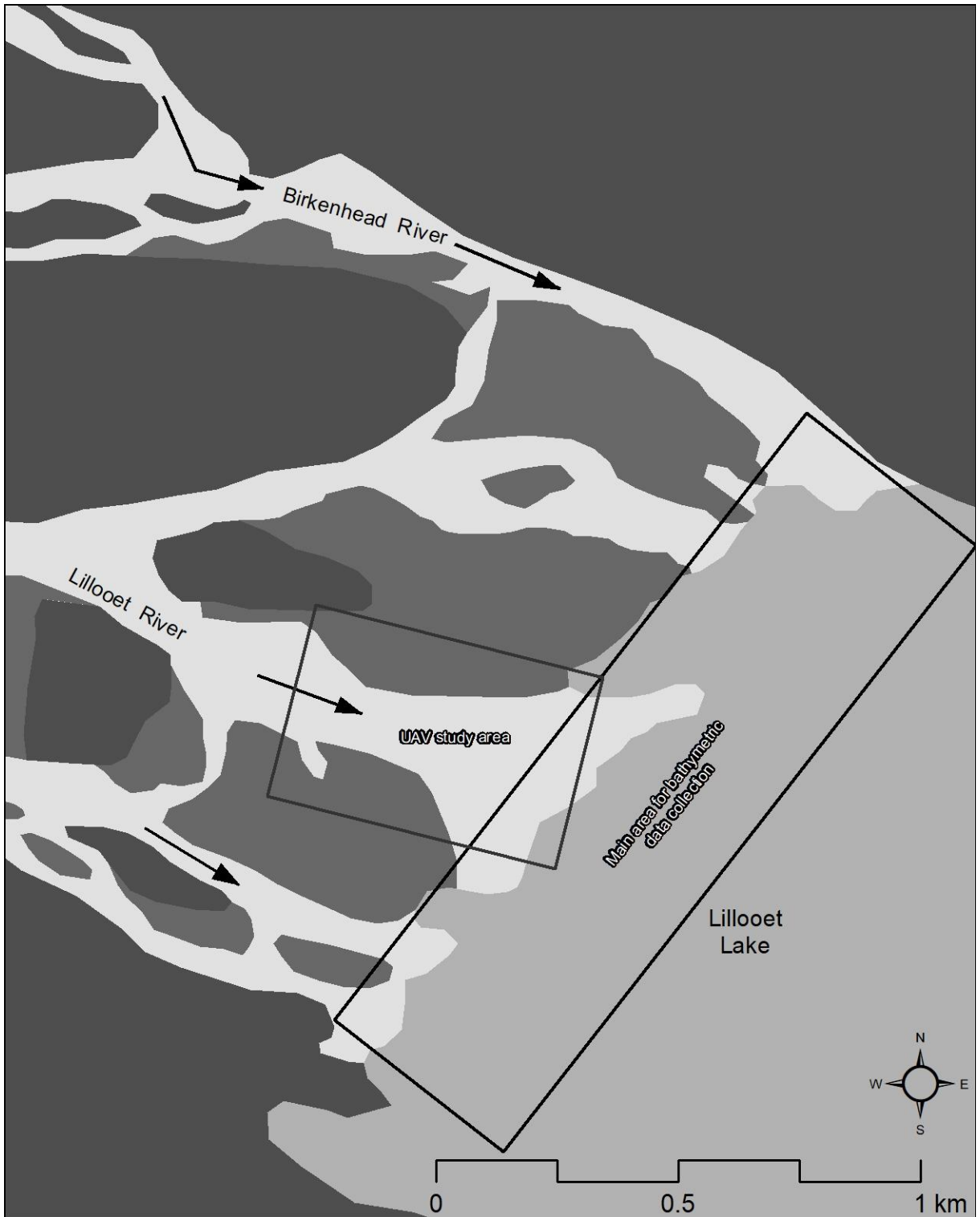


Figure 18: Study areas for remotely sensed data used in this study area. These datasets include UAV imagery and bathymetric transects in the area immediately offshore the delta.

5 Results

5.1 River hydrology and suspended sediment

5.1.1 Flow regime

The average annual daily hydrograph for Lillooet River above Green River (08MG005) shows a single peak rising at the beginning of summer, peaking in the middle of July, then descending at the end of summer, similar to that described by Eaton and Moore (2010) for Lillooet River (Figure 19 a). The maximum annual daily hydrograph for Lillooet River shows that the largest daily peak flows occur in late August through November and do not appear to be related to the traditional glacier-melt regime but rather to large Pacific storms that occur in the autumn (Gilbert, 1975; Gilbert et al., 2006). The largest recorded daily average flow occurred on 18-October-2003 ($1,370 \text{ m}^3 \text{ s}^{-1}$). There is also significantly more variation observed on the maximum annual hydrograph, especially during these fall months. Although the largest daily peak discharge events occur in the fall months (Figure 19 a), the largest number of annual peak-flow events occur in July, followed distantly by June and August (Figure 19 b).

In the 2015 calendar year, Lillooet River reached a peak daily flow of $569 \text{ m}^3 \text{ s}^{-1}$ that occurred on 20-September-2015 (attributed to precipitation). In this same year, Lillooet River had a low discharge rate of $21.6 \text{ m}^3 \text{ s}^{-1}$ which occurred on 31-December-2015. While the primary hydrograph peak occurred in September there were significant secondary peaks that were observed in June, July, August, and October (Figure 19 c). From 22-July-2015 to 01-August-2015, the study period, there was far less discharge on Lillooet River than would typically be expected for this period. During this period, the

highest daily flow was $242 \text{ m}^3 \text{ s}^{-1}$ on 01-August-2015 and the lowest daily flow was $153 \text{ m}^3 \text{ s}^{-1}$ on 26-July-2015. The hydrograph for this period is shown in Figure 19 d, which is compared to the average daily hydrograph and total range of flows recorded between 1914-2016. Most vividly, the flow on Lillooet River during the study period is very low, with the discharge rate on July 27 being the lowest flow ever recorded for any July 27 in the 97-year history of gauged data on Lillooet River. Flows on July 22-26 and July 28-30 were very near the lowest flows ever recorded for those dates as well (Figure 19 d).

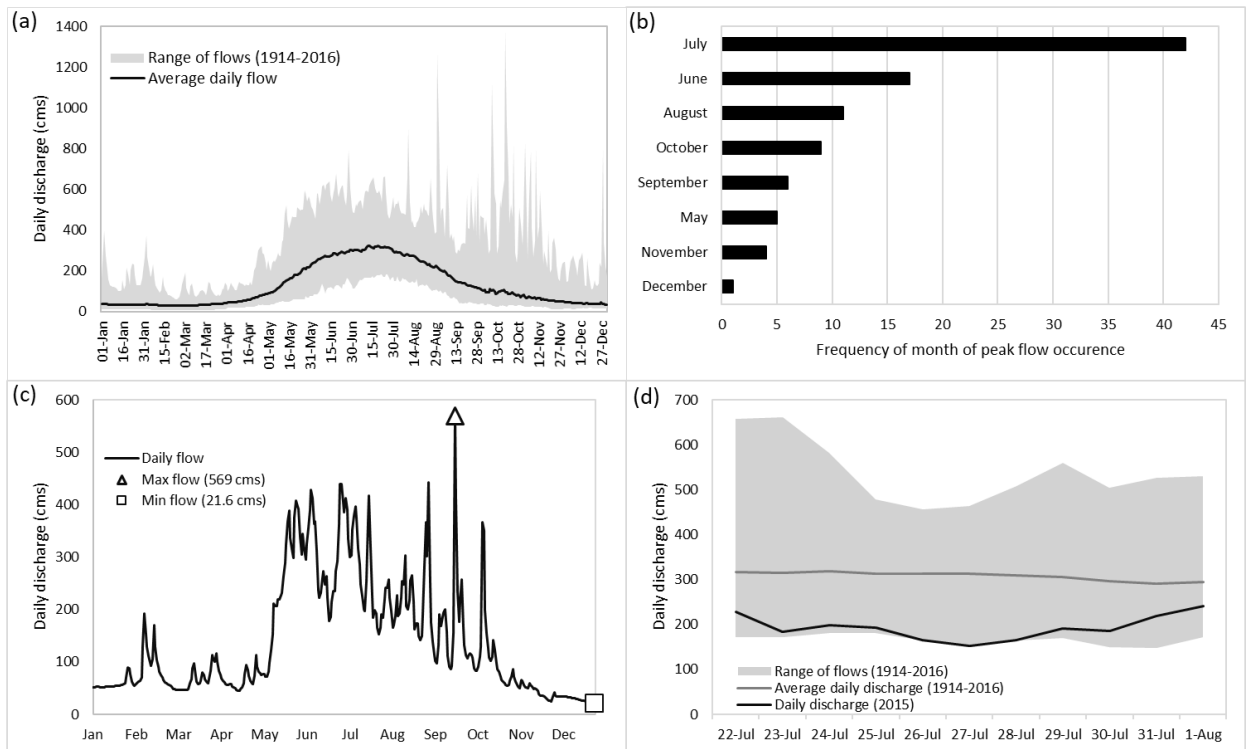


Figure 19: Water Survey of Canada hydrographs of Lillooet River (08MG005). Panel (a) shows the mean, maximum, and minimum daily flows over calendar years 1914-2016. There is significant variation in flow data, especially in the fall months because of infrequent Pacific storms. Panel (b) shows the frequency of which months report the greatest amount of annual peak flow events per calendar year. July is by far the month with the most peak flow values, followed distantly by June and August. Panel (c) shows the daily hydrograph for 2015. In this hydrograph there is significant variability observed, with the peak flow occurring in September. The period between July 21 to August 31 is a large dip in flow activity compared to earlier that summer and the large storm peaks that exist in September and October. Panel (d) shows the average daily discharge from 1914-2016 with the range of observed flows (1914-2016) around it. The

daily discharge values from 22-31 of July 2015 are at the bottom edge of the range box. Flow on 27-July-2015 is the lowest flow reported for that calendar day in the period of 1914-2016.

At the river delta, where field monitoring occurred, a HOBO U20 water level logger was deployed (Chapter 4). Once corrected for atmospheric pressure, water level data was compared to river discharge from the WSC Lillooet River station (08MG005). The comparison shows a significant relationship between daily average river level at Lillooet-Green River delta and daily data from the WSC hydrometric gauge ($r^2=0.99$, $n=5$, $p=0.001$) which indicates that flow from Lillooet River is a good predictor of flow through the Lillooet-Green River delta at a daily scale. At a 5-minute scale the relationship breaks down ($r^2=0.55$, $n=1018$, $p=0.000$) but on a closer inspection, this is due to a hysteretic relationship between the WSC gauge and the Lillooet-Green River gauge with a lag-time of approximately 3 hours. After adjusting for a 3-hour time difference of the peak flow, the relationship between the WSC gauge and water level data significantly increases at the 5-minute scale ($r^2=0.96$, $n=983$, $p=0.000$).

The river temperature measured in Lillooet River ranged from 11.0-13.0°C. Peak daily river temperature precedes the daily peak in discharge by between 1.5-2.5 hours. The lowest daily river temperature also precedes the daily low of discharge by the same amount of time.

At an hourly scale, river pressure shows a consistent diurnal pattern. Peaks occur between 07:00 and 09:00, whereas troughs occur between 20:00 and 23:00. The strong diurnal pattern is typical of a glacial melt regime, which is governed by the energy available for melt at higher elevations in the river basin (Chapter 2).

5.1.2 Hydrometeorology

The pyranometer installed on the Lillooet-Green River delta measures incoming solar radiation. It cannot measure the net effects of shortwave radiation (including outgoing radiation) and it also does not measure the balance of the longwave radiation terms, but it can provide a proxy for glacier melt energy because it records the incoming solar radiation being received from the sun through the atmosphere whose effects directly contribute to glacier melt (Chapter 2). Figure 20 shows those meteorological variables that affect streamflow in Lillooet River.

During the field campaign, low flow was recorded at the WSC Lillooet River gauge (08MG005). Incoming shortwave radiation, observed at the delta, show diurnal swings from 0 W m⁻² each night to a maximum of 908.83 W m⁻² on 28-July-2015. The solar constant that is used in most energy balance equations is 1365-1368 W m⁻², measured at the top of atmosphere (Hock, 2005; Kopp and Lean, 2011). This would indicate that the atmosphere is scattering and absorbing up to 33% of the incoming solar radiation at this location. During the field campaign, smoke from forest fires made the air hazy and reduced visibility. At higher elevations up the valley from Lillooet Lake, two fires actively burned during the study period, reducing visibility and making the sky hazy (BC MFLNRO, 2015). These fires would have reduced the transmissivity of the atmosphere, resulting in a decrease of shortwave radiation at the surface. The net result is less melt energy, resulting in less runoff from Lillooet Glacier flowing into Lillooet River. Figure 21 shows field photos of the atmosphere at different times in the study period.

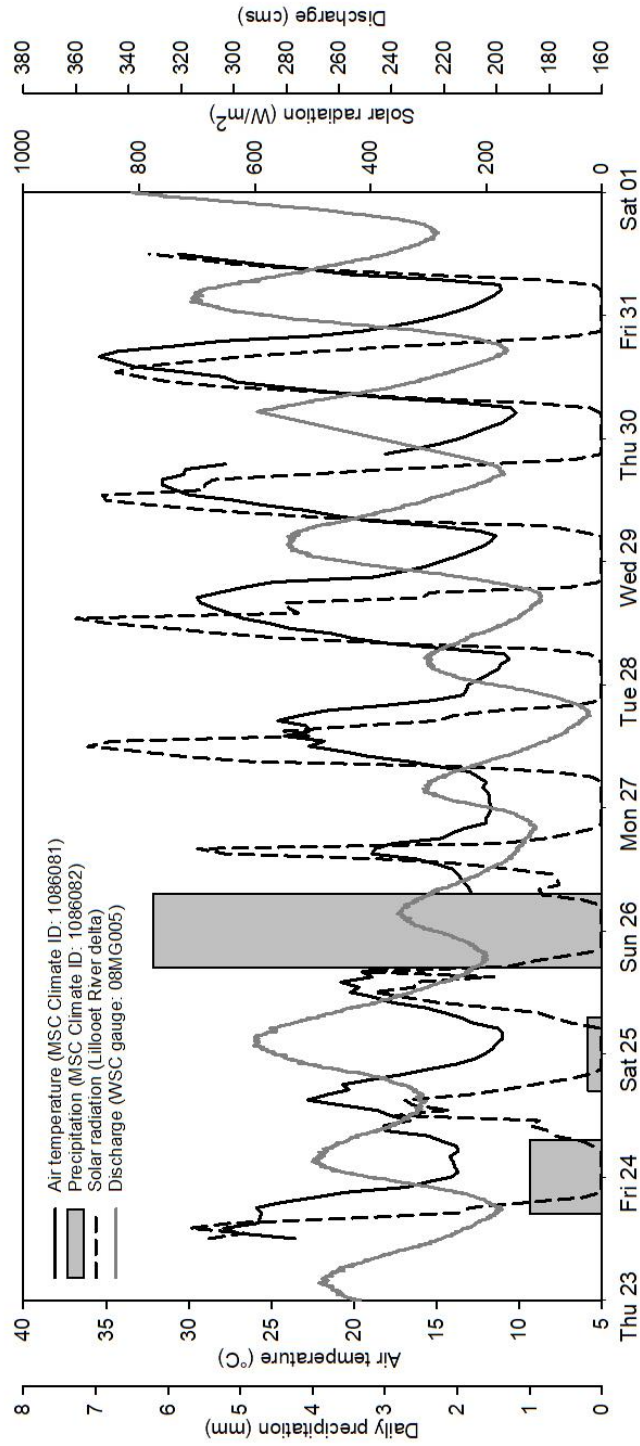


Figure 20: Meteorological variables affecting runoff. Air temperature, solar radiation, and discharge all have very similar wavelengths but different phases of diurnal peaks. This trend is expected as air temperature and solar radiation are contributors to runoff of Lillooet River. The timing of each peak is slightly different with solar radiation peaking first, air temperature peaking after that then discharge peaking early in the AM as a response to those other variables.

Precipitation was recorded for three days; however very little precipitation was recorded, and it appeared to have almost no impact on the response of the hydrograph.



Figure 21: Field photographs showing the amount of haze in caused by the forest fires located higher up in the valley. The photo in the left panel was taken on July 29 and is looking upstream of Lillooet River from the delta. The mountains in the background are shrouded with haze, resulting from forest fires in the region. The right panel was taken on July 30 and is looking down Lillooet Lake from Lillooet River delta. Haze is evident in the distance.

5.1.3 Suspended sediment concentration and grain size

Suspended sediment concentration (SSC) is measured in mass concentration as milligrams of [dry] sediment per litre of water (mg l^{-1}). The time series of turbidity within the river (NTU) was converted to a time series of C (volume suspended sediment concentration) by using linear regression ($r^2=0.96$, $n=48$, $p=0.000$), which was in turn converted to mass concentration by filtering, drying, and weighing the sediment ($r^2=0.95$, $n=7$, $p=0.000$). The volume suspended sediment concentration time series was cleaned up (anomalous values removed) and is shown as Figure 22. Anomalous values were defined as values that were single-period peaks (or troughs) in the data that fall far outside of the trend of the rest of the data.

The mean diameter of the sediment particles within the river ranges from $15.6 \mu\text{m}$ to $72.5 \mu\text{m}$ ($n=48$). The average diameter of sediment particles throughout the entire period is $27.8 \mu\text{m} \pm 11.4 \mu\text{m}$ (1-SD) and the D_{50} (median) is $24.8 \mu\text{m}$. This is similar to

the median sediment diameter reported by Kostachuk et al. (2005) who reported D_{50} values between 1-25 μm , decreasing in size with height above the lake bed in an observed underflowing turbidity current in Lillooet Lake.

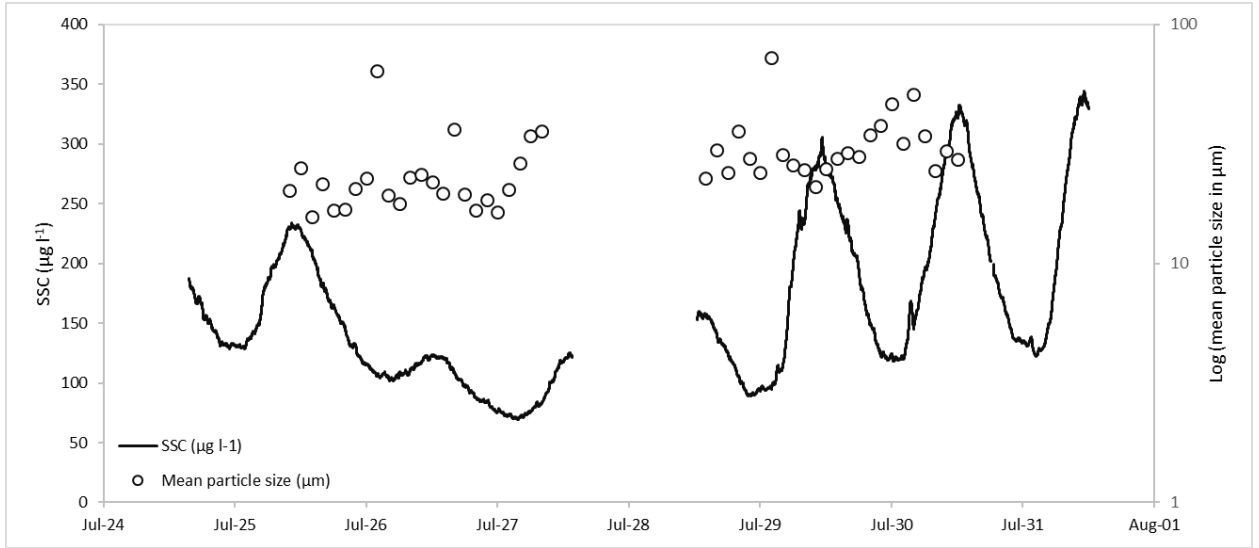


Figure 22: Timeseries of SSC and mean particle size. Mean particle size is shown as well. Mean particle size is plotted on a log-scale and does not appear to follow the same diurnal pattern as SSC. The gap in the middle of the data on July 27-28 is due to changing the batteries on both the water sampler and turbidity probe.

The pattern of C closely resembles the diurnal variation observed in river discharge (above), although there is a distinct offset of the peaks. To help understand this offset between peak flow and peak sediment, Lawler (2006) proposed a hysteresis index for suspended sediment and river discharge. This hysteresis index compares the turbidity and discharge relationship. Because we have SSC and river height (not discharge), we can rewrite the terms of the equation as follows:

$$RH_{mid} = k(RH_{max} - RH_{min}) + RH_{min} \quad (20)$$

Where k is the coefficient for the hysteresis index and denotes the position at which the breadth of the loop is measured in relation to the range in river height; k is most commonly set to 0.5 which is the midpoint of the rising limb of river height. RH_{mid}

is the midpoint of river height, RH_{max} is the maximum river height and RH_{min} is the minimum river height within a single peak hydrograph. After RH_{mid} has been calculated there are two equations that can be used based on the direction of hysteresis. The first equation is used for positive hysteresis and the second equation is used for negative hysteresis. Equation 21 should be used when $SSC_{rl} > SSC_{fl}$ and equation 22 should be used when $SSC_{rl} < SSC_{fl}$ (SSC_{rl} – rising limb, SSC_{fl} – falling limb).

$$HI = \frac{SSC_{rl}}{SSC_{fl}} - 1 \quad (21)$$

$$HI = \frac{-1}{\frac{SSC_{rl}}{SSC_{fl}}} + 1 \quad (22)$$

Equation 2 (above) was used to calculate hysteresis for all cases in this study. The calculated hysteresis values are -1.4 (July 28-29) and -1.6 (July 29-30). These values are like those values that are reported in Lawler (2006) for storm events in a highly urbanized, “mid-land” reach of the Thames River in the United Kingdom. Mao and Carrillo (2017) reported HI values of +0.53 and -1.12 in a glacier-fed basin in the Andes, thus showing both positive and negative hysteresis. Where negative hysteresis was shown in that study it is quite like the values reported here (Mao and Carrillo, 2017).

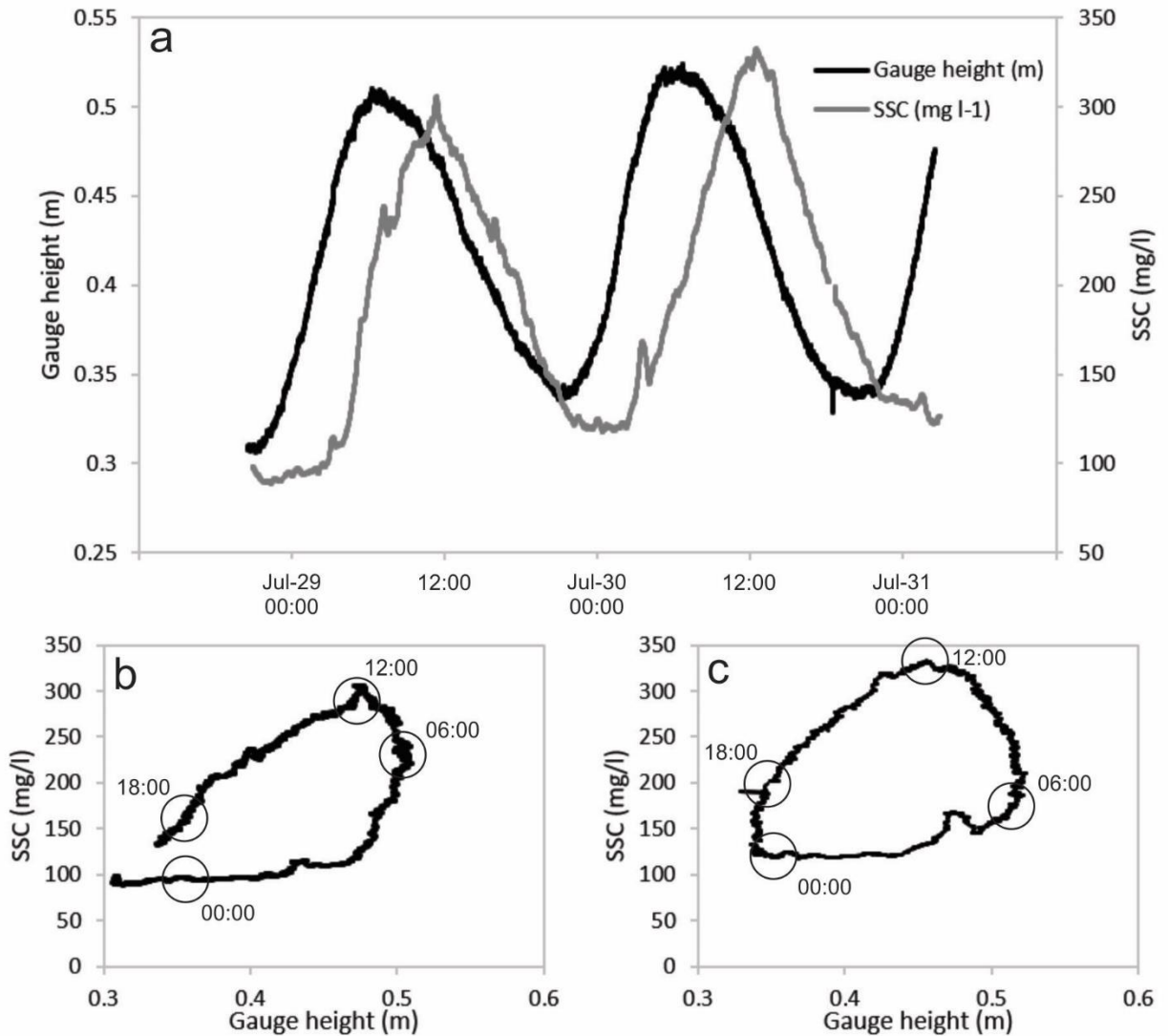


Figure 23: Hysteresis loops of SSC and river height. The top panel (a) shows the time series of SSC and river height in their joint period of record. Each curve exhibits a characteristic diurnal pattern. The bottom panel shows the hysteresis loops from July 28-29 (b) and July 29-30 (c). Both curves have a counter clockwise loop, indicating negative hysteresis.

Grain-size analysis of sediments were taken from Lillooet River (Figure 22), using a Sequoia LISST-ST which uses 32-bins with midpoints distributed logarithmically between 2.5-500 μm (Hodder, 2009). Mean grain size calculated from the water samples was 27.8 μm with two large distinctive spikes of 63.8 μm and 72.4 μm . The pattern of SSC vs grain size shows a general trend of decreasing particle size with increased SSC.

The trend is more apparent at higher SSC flows but at the lower end, it appears to be divergent with a wide spread of values between mean grain size and SSC. When the particle density is compared to mean grain size there is a slight upward trend where larger particle size tends to be associated with larger particle density.

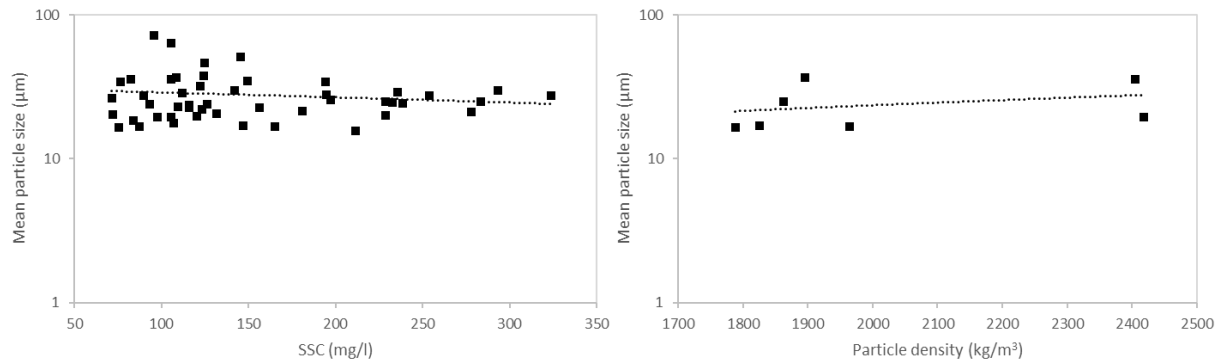


Figure 24: The left pane shows SSC vs mean particle size. There is a slight decreasing trend in mean particle size as SSC increases. This is obscured at the lower end of SSC where a large range of particle size values exist (n=48). The right pane shows particle density vs. mean particle size. There is a slight trend that as particle size is increasing, so too is particle density (n=7).

5.2 Deltaic dynamics

5.2.1 Plunge line

The plunge line is the boundary between incoming river water and ambient lake water where the incoming river water begins to sink below the surface of lake water. The different parcels of water form a distinct boundary that is visible in imagery and from visual observation in the field (Figure 25). Also noted along the north boundary between the inflowing river water and ambient lake water, K-H instabilities (or waves) were observed. K-H instabilities facilitate mixing in the vortices produced at the interface of the two fluid masses.

Observations of satellite imagery from July-August 2015 show the plunge line forms generally perpendicular to the incoming flow of river water. This line developed a lobe on the northeastern end where large debris was observed to collect (Figure 26, Point A). This plunge line appears to be oriented longitudinally from the northern edge of the delta channel. The incoming lake water was observed to have a higher concentration of suspended sediments as observed from the river monitoring data, which explains its distinctive appearance from the ambient lake water. The highly turbid river water flows to the plunge line, at which time it was observed to plunge below the surface. Larger (floating) debris, such as pumice and wood, carried by the river collected at the end of the lobe where they were ejected into the lake. Ambient lake water was also observed flowing back towards the plunge line as a counter-current where it was entrained into the plunging flow.

Observations in the field indicate that the highest river velocities were along the north side, directed towards the lobe. There appeared to be a gradient of velocity at the front of the plunge line with the lobe at the maximum velocity and lesser velocities towards the south bank. Over the course of the study, the plunge line lobe was observed to migrate northwards approximately in line with the eroding surface of the north side of the channel bank. Field observations revealed that the greatest channel velocity was located on this side which is likely what caused both the high rates of erosion along this bank and the lobe extending further out into the lake at this point because higher velocity water will cause inflowing river water to plunge deeper (Lamb et al., 2010). Table 3 shows the change in migration rates between observations made with the UAV, a Garmin handheld GPS, and with low-resolution Landsat 8 imagery from periods within, before,

and after the period of observation. The changes in erosion of the shoreline are shown in Figure 27. These changes were measured at the most lakeward end of the shorelines displayed on the map. The shoreline does not erode continuously or linearly, instead showing more erosion at the lakeward end and at the beginning of the study period than towards the end. It appears to be eroding much like the outer bank of a meander loop in a stream. Field observations suggest that the opposite (south) channel bank is aggrading while the north end erodes. No direct field measurements were made of this aggradation rate and it was not obvious at the time whether water levels were fluctuating to expose more sediment or if this was aggradation of the channel shoreline.

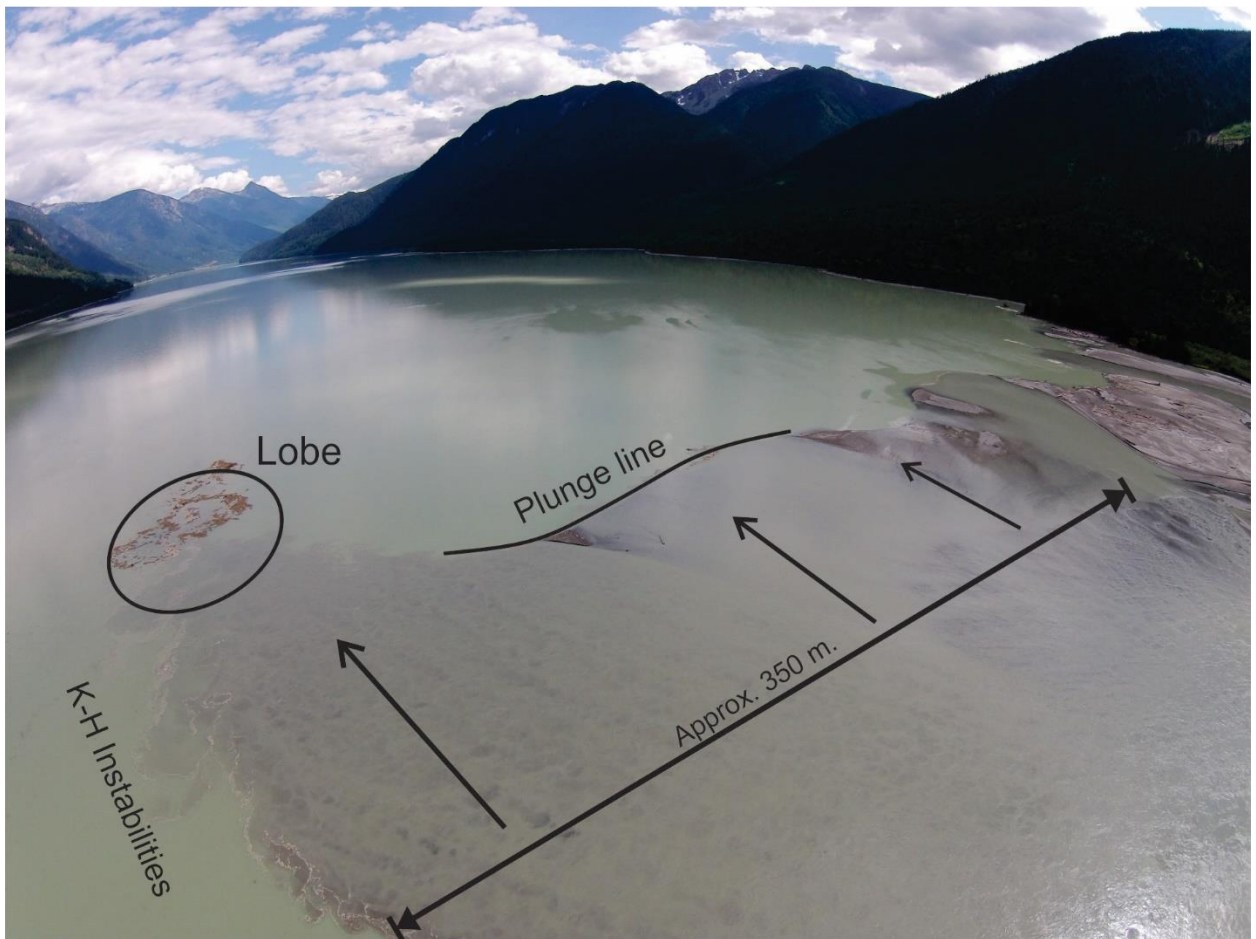


Figure 25: Oblique aerial image of the plunge line and lobe (July 28). The incoming river water is at the bottom of the image. The incoming river water plunges below the surface of the lake at the location of the plunge line. This line is the boundary between incoming river water and ambient lake water. K-H instabilities were observed to form on the north side of the inflowing river water indicating shear stresses at the flow boundary between the two water masses.

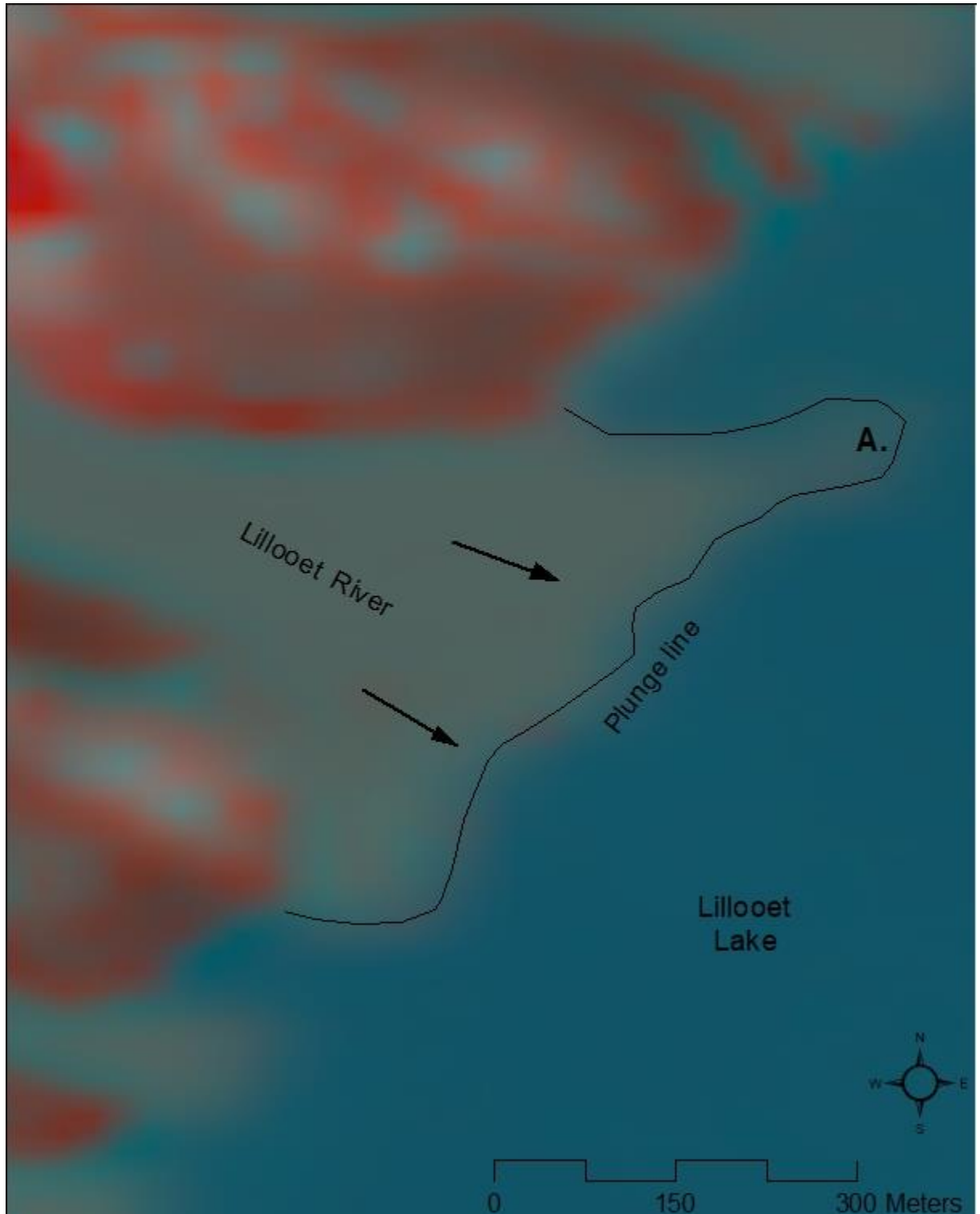


Figure 26: Landsat 8 image showing plunge line on Lillooet-Green River delta (August 1, 2015). The black line is the rough location of the plunge line mapped from the Landsat 8 imagery. Point A shows the lobe that formed on the NE end of the plunge line.

Table 3: Migration of the channel delta bank. The amount of change measured below is the difference between the location of the lakeward end of the mapped shoreline between the first date and the second date listed below. Cumulatively between July 16 and August 9, 2015 a total of 156 metres of lateral migration was observed.

First date	Second date	Amount of Change between dates
July 16, 2015	July 23, 2015	53.9 metres
July 23, 2015	July 25, 2015	39.6 metres
July 25, 2015	July 27, 2015	5.3 metres
July 27, 2015	July 28, 2015	3.9 metres
July 28, 2015	July 29, 2015	17.7 metres
July 29, 2015	July 30, 2015	9.9 metres
July 30, 2015	July 31, 2015	4.3 metres
July 31, 2015	August 1, 2015	9.6 metres
August 1, 2015	August 9, 2015	15.6 metres
Total observed migration at the end of the channel bank		159.8 metres

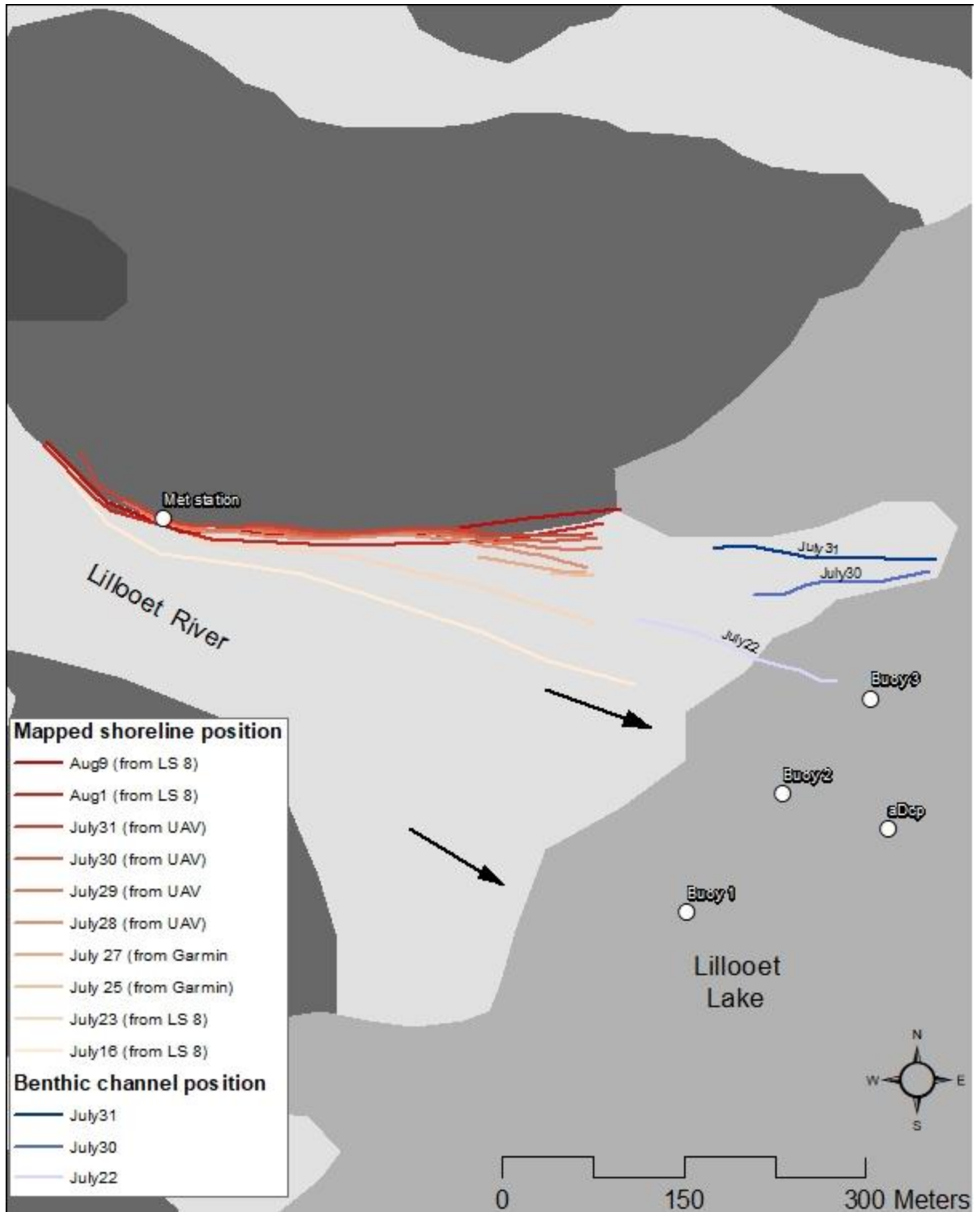


Figure 27: Migration of the channel bank at Lillooet Lake. The shorelines were mapped from either UAV imagery, by a Garmin 62S GPS, or else by Landsat 8 imagery. The changes to the position of the shoreline are not equal across the length of the shoreline and more erosion is observed at the lakeward edge. The benthic channel positions were taken

from the bathymetric surveys that were collected over multiple days in front of the Lillooet-Green River delta. The position and orientation of the apparent benthic channel appear to shift throughout the period of observation.

5.2.2 Bathymetry dynamics

Bathymetric data was collected near the delta front on July 22, 29-31. Due to the scarcity of some data points, only select point data is compared from the 29-30 July surveys. Two cross sections were drawn off the front of the delta and extending 200-250 metres out into the lake as shown on the map in Figure 28. These cross sections show changes in the height and slope of the delta foreset (Figure 29). The most notable change is the height of the bed between the July 22-31 surveys between 60-100 metres on both Profile A-A' and B-B'. The change in depth (e.g. rise in height) at these locations appears to indicate a rapid accumulation of the delta foreset as sediment accumulates rapidly along the slope of the delta. The amount of accumulation reduces beyond 15-20 metres depth. On Cross-section B-B', at 170 metres, the 30-July point appears at a greater depth than that on 31-July. At 200 metres out, the 29-July point also appears lower than both the 30-July and 31-July depths. These phenomena may indicate the passage of a benthic channel, like that described by Gilbert (1973) or Lambert (1988), where the channel was carved at an earlier date then infilled at both these locations by 31-July.

Measurements taken from the cross section indicate that the maximum amount of aggradation seen on Cross-section A-A' is 7.7 metres and the maximum aggradation on Cross-section B-B' is 3.0 metres. These changes represent bulk aggradation rates of 3.5 cm hr⁻¹ at Cross-section A-A' and 1.3 cm hr⁻¹ at Cross-section B-B', assuming a linear rate of accumulation.

It is also observed at these cross-sections that the slope of the delta foreset has increased dramatically. Although there is a large amount of aggradation observed at the front of the delta, the aggradation is not uniform throughout the profile, indicating a steepening of the sediments on the foreset beds. The maximum slope observed on the delta foreset in 22-July is 21% where the maximum slope observed on 31-July is 67% at Cross-section A-A' and on cross-section B-B' the 22-July slope is 24% and the 31-July slope is 33%. It may be assumed that the continual steepening of the delta beds will eventually result in a failure of this slope, the result of which could be a surge-like turbidity current (Chapter 2).

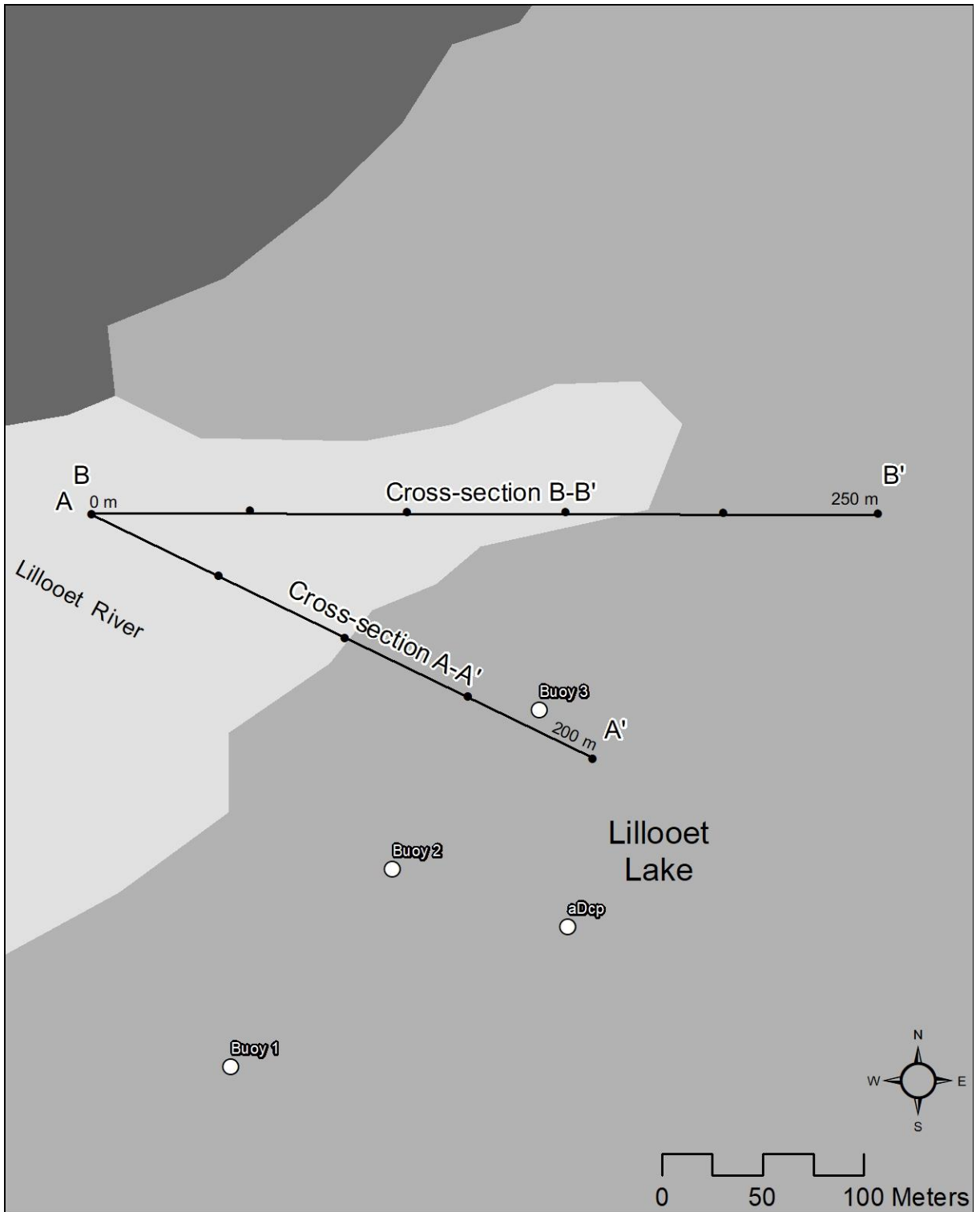


Figure 28: Map showing the locations of the bathymetric Cross-sections A-A' and B-B'. The black points along each cross section represent 50 metre distances along those cross sections. In the background mapping, the plunge line appears at 100 metres along Cross-section A-A' and 160 metres along Cross-section B-B'.

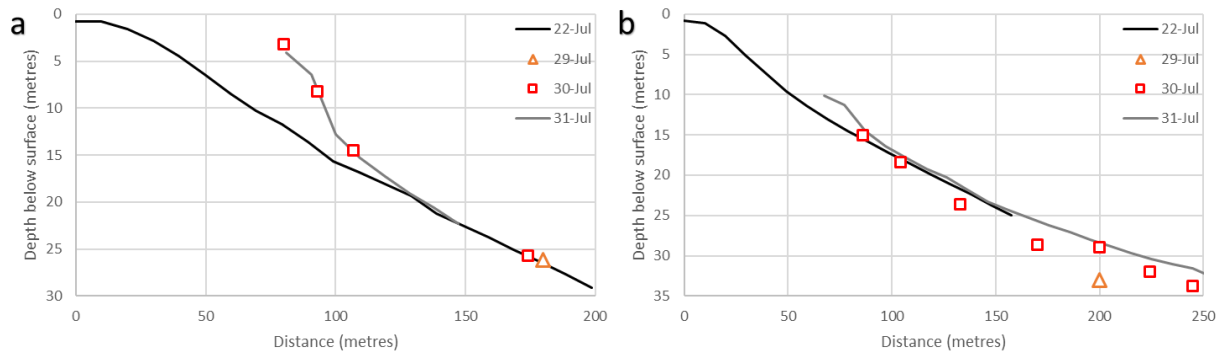


Figure 29: Bathymetric cross sections take at the front of the Lillooet-Green River delta. Cross-section A-A' (panel a) extends from the mouth of the river out into the lake 200 metres in a southeast direction. The depth increases from 0.8 metres to 29 metres. Cross-section B-B' (panel b) extends from the mouth of the river into the lake 250 metres in an east direction. The depth increases from 0.8 metres to 53 metres.

5.3 Lacustrine monitoring

5.3.1 Lillooet Lake Level

During the period of study, Lillooet Lake levels were quite low. Daily lake levels fluctuated between 26.22-26.88 metres (Chapter 2). By comparison, the average lake level for this same time period ranges from 27.14-27.35 metres (1971-2016), which represents 0.47-0.95 metres below average. An analysis of the hydrometric record of Lillooet Lake shows that the lake levels between 24-July-2015 and 01-August-2015 are the lowest recorded lake levels for those dates in the 44-year hydrometric record (08MG020; Figure 30).

The abnormally low lake levels for this time of year coincided with exposure of the delta topset sediments. As was also observed on the delta, rapid lateral migration of the river channels that incise the delta occurred. As Gilbert (1973) explained, this has been noted to occur at very low lake levels.

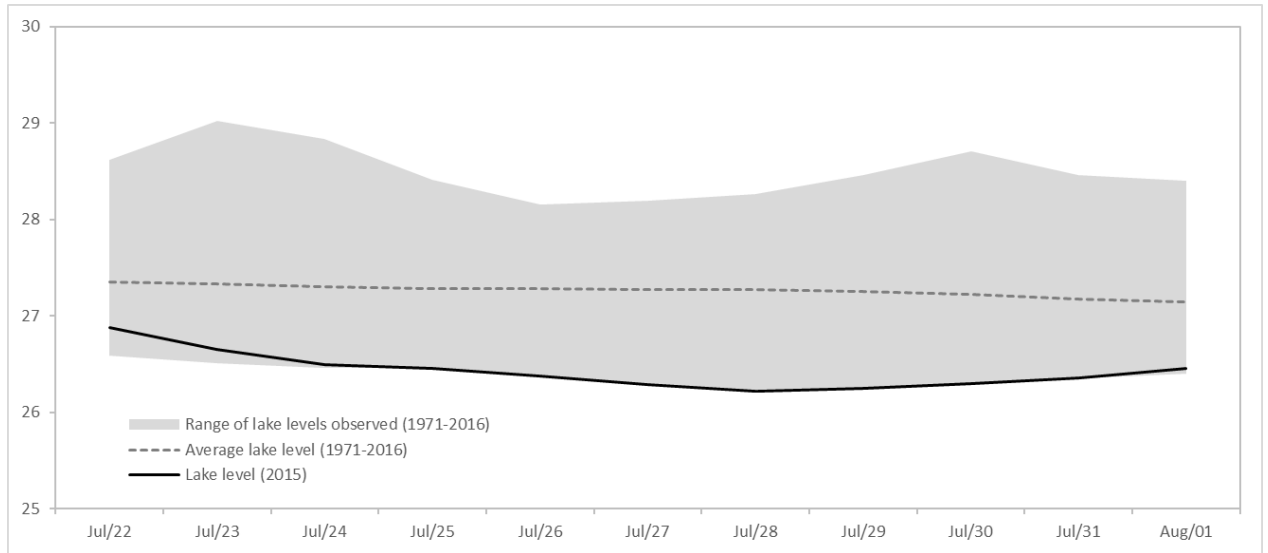


Figure 30: Water Survey of Canada lake level summary data from 22-July to 01-August (WSC gauge 08MG020). The black line represents the lake level data from 2015, while the grey box is the range of lake level data from the period of record (1971-2016). The dark grey line is the average lake level date for each date. Lake level during this period was very low, resulting in a greater exposure of deltaic sediments.

5.3.2 Lake temperature moorings

Three moorings were deployed off the front of Lillooet-Green River delta to measure the temperature of lake water. The anchored moorings were placed in water that was between 21-25 metres deep. The bottom sensors were set so they would be approximately 2 metres from the lake bottom, the middle sensors were set to be approximately 10 metres from the lake bottom and the top sensors were placed so they would be near the surface (25 metres) from the bottom. The location of these moorings is shown in Figure 28. Lake temperature at these sensors appears to respond to diurnal fluctuations, however, their relationship with river temperature is weak. The average water temperature measured by the top sensors is 14.7 °C. The top sensors appear to respond greatest to diurnal fluctuations in temperature. The average water temperature of the middle group is 13.1 °C. The average water temperature of the bottom group is 12.8

°C. The bottom and middle group lake temperature sensors are closest in temperature to the river temperature however, they do not appear to respond to the same diurnal patterns. The thermal characteristics of the water temperature profiles in the lake, especially those in the middle and bottom group are like the water temperatures reported in Lillooet-Green River (Figure 31). This would suggest that density currents that do develop are not the result of temperature-driven density differences because this gradient is so small. The time series of both lake temperature and river temperature sensors is shown in Figure 31.

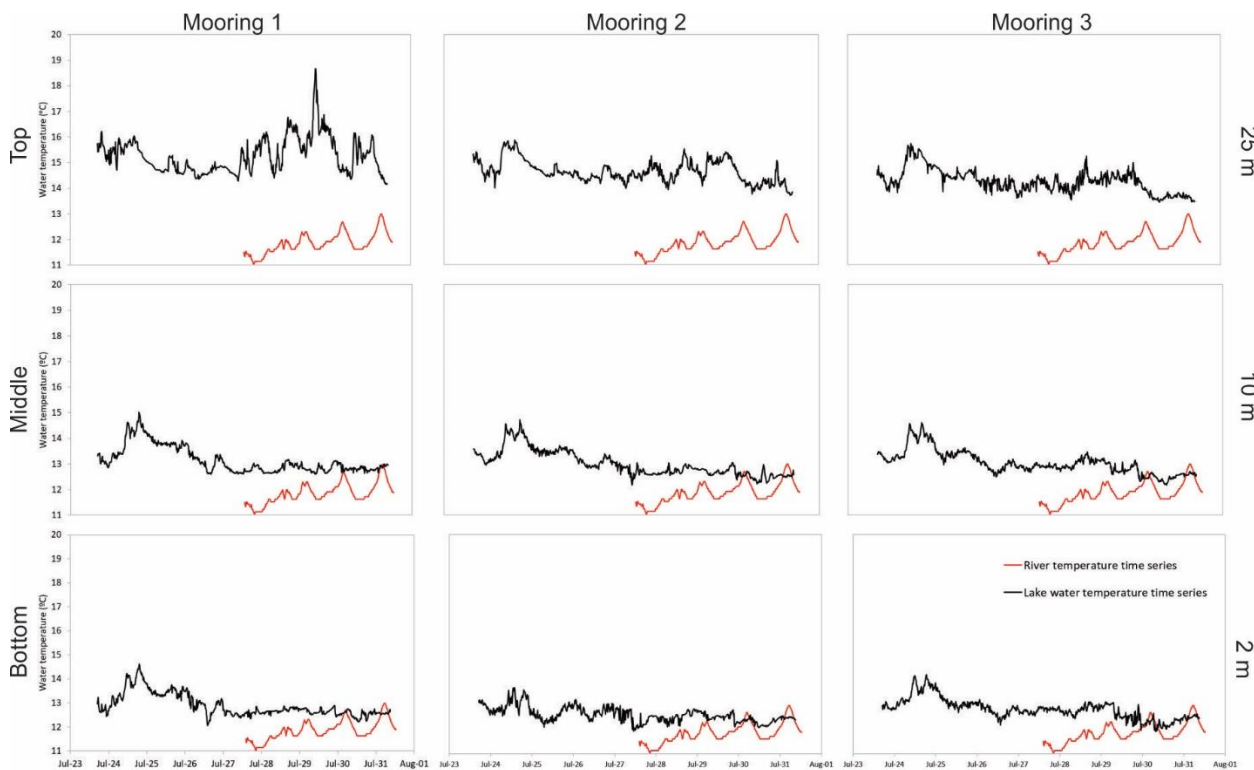


Figure 31: Lake temperature moorings (shown in black) located at the front of Lillooet-Green River delta. Data was averaged over 15-minute period. From left to right are buoy 1, buoy 2, buoy 3 and from top to bottom are the top, middle, bottom sensors (e.g. top left sensor is Buoy 1, Top sensor, bottom right sensor is Buoy 3, Bottom sensor). Lake temperature (, as measured from the nine sensors does not appear to respond to river temperature. This indicates there is not a substantial relationship between any of these sensors and the measured river temperature (shown in red).

A correlation matrix comparing all nine lake temperature sensors shows that there is quite strong correlation among middle and bottom sensors. The top sensors, especially

Top 1 and Top 2 are uncorrelated with the rest of the sensors. Bottom 2 also shows a very poor correlation with the rest of the sensors in the array. The top sensors, especially Top 1 appear to be influenced by diurnal fluctuations, possibly due to diurnal heating. Top 1 has the greatest range of temperature recorded.

Table 4: Correlation matrix between lake temperature sensors deployed into Lillooet Lake. The Top sensors and Bottom 2 sensor show poor correlation to the remaining sensors. Bolded and shaded values depict correlations greater than $r=0.7$.

		Top1	Top2	Top3	Middle 1	Middle 2	Middle 3	Bottom 1	Bottom 2	Bottom 3
Top1	Pearson Correlation	1	0.54	0.27	-0.08	-0.07	0.08	-0.03	0.1	0.06
	Sig. (2-tailed)		0	0	0	0	0	0.001	0	0
	N	1104	1104	1104	11040	11040	11040	11040	11040	11040
Top2	Pearson Correlation	0.54	1	0.74	0.5	0.55	0.64	0.52	0.5	0.57
	Sig. (2-tailed)	0		0	0	0	0	0	0	0
	N	1104	1104	1104	11040	11040	11040	11040	11040	11040
Top3	Pearson Correlation	0.27	0.74	1	0.7	0.73	0.8	0.71	0.52	0.74
	Sig. (2-tailed)	0	0		0	0	0	0	0	0
	N	1104	1104	1104	11040	11040	11040	11040	11040	11040
Middle 1	Pearson Correlation	-0.08	0.5	0.7	1	0.9	0.84	0.94	0.55	0.77
	Sig. (2-tailed)	0	0	0		0	0	0	0	0
	N	1104	1104	1104	11040	11040	11040	11040	11040	11040
Middle 2	Pearson Correlation	-0.07	0.55	0.73	0.9	1	0.87	0.89	0.69	0.8
	Sig. (2-tailed)	0	0	0	0		0	0	0	0
	N	1104	1104	1104	11040	11040	11040	11040	11040	11040
Middle 3	Pearson Correlation	0.08	0.64	0.8	0.84	0.87	1	0.86	0.64	0.93
	Sig. (2-tailed)	0	0	0	0	0		0	0	0
	N	1104	1104	1104	11040	11040	11040	11040	11040	11040

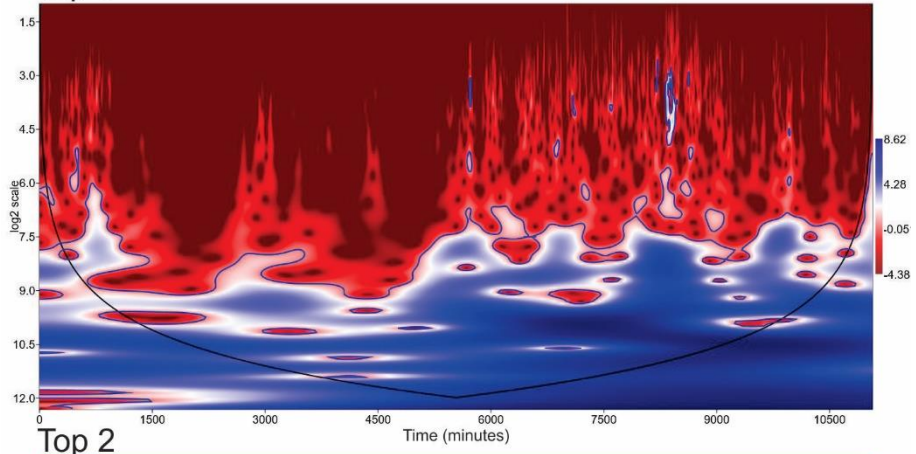
Bottom 1	Pearson Correlation	-0.03	0.52	0.71	0.94	0.89	0.86	1	0.57	0.79
	Sig. (2- tailed)	0.001	0	0	0	0	0		0	0
	N	1104	1104	1104	11040	11040	11040	11040	11040	11040
	N	0	0	0	11040	11040	11040	11040	11040	11040
Bottom 2	Pearson Correlation	0.1	0.5	0.52	0.55	0.69	0.64	0.57	1	0.58
	Sig. (2- tailed)	0	0	0	0	0	0	0		0
	N	1104	1104	1104	11040	11040	11040	11040	11040	11040
	N	0	0	0	11040	11040	11040	11040	11040	11040
Bottom 3	Pearson Correlation	0.06	0.57	0.74	0.77	0.8	0.93	0.79	0.58	1
	Sig. (2- tailed)	0	0	0	0	0	0	0	0	
	N	1104	1104	1104	11040	11040	11040	11040	11040	11040
	N	0	0	0	11040	11040	11040	11040	11040	11040

To further understand the relationships between the water temperature sensors in the lake, wavelet analyses were performed for all 9 lake temperature sensors. The wavelet analysis allowed for the interpretation of shared or unshared variance throughout the time series of each sensor. PAST3 software was used to conduct the Continuous Wavelet Transform (CWT; Hammer et al., 2001). A wavelet transformation can be used to analyze localized variations of power within a time series (Torrence and Compo, 1998). The transformation is a type of band-pass filter that has a uniform shape but varying locations and widths, dissimilar to a traditional Fourier Transformation (Torrence and Compo, 1998). There are several wavelet bases that can be used, the most common of which is a Morlet wavelet (Torrence and Compo, 1998; Hammer et al., 2001). Wavelet Transforms tend to work better than Windowed Fourier Transform (or Short-term Fourier) because the Windowed Fourier Transform requires a time-scalar into the analysis (Torrence and Compo, 1998). Because of the time-scalar, low or high scale frequency components will be missed as the analysis looks at windows of a specific size

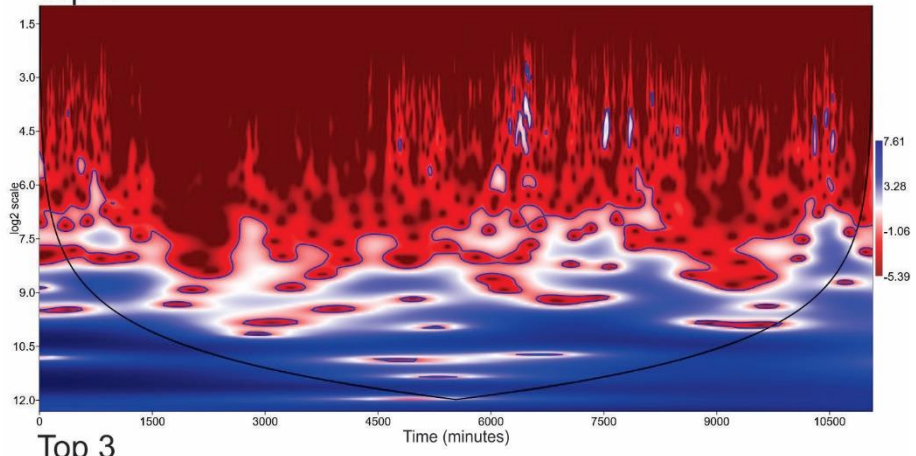
only. A criticism of wavelet analysis surrounds the choice of the wavelet function (Torrence and Compo, 1998).

A wavelet transform analysis was conducted on the lake temperature data using a Morlet wavelet. Figure 32 shows the wavelet transformation on the entire time series of each of the 9 lake temperature sensors. All 9 sensors appear to share common frequency at a scale of $2^{10.5}$ seconds (24-hours) across the entire time-series. This indicates that there is a diurnal temperature pattern apparent in all the temperature sensors even though it may not be visible by eye at the deeper locations.

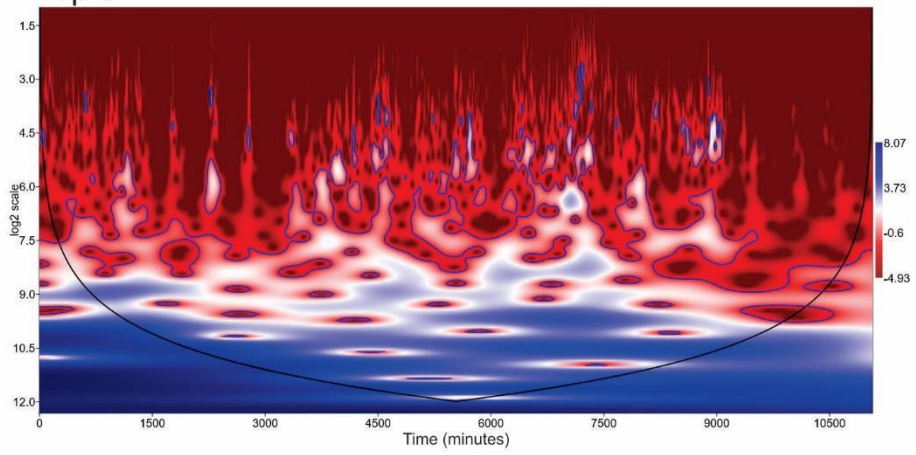
Top 1



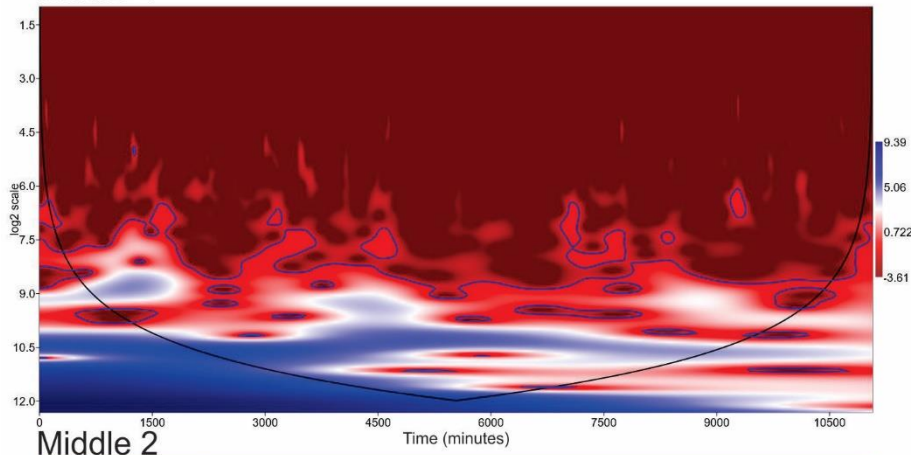
Top 2



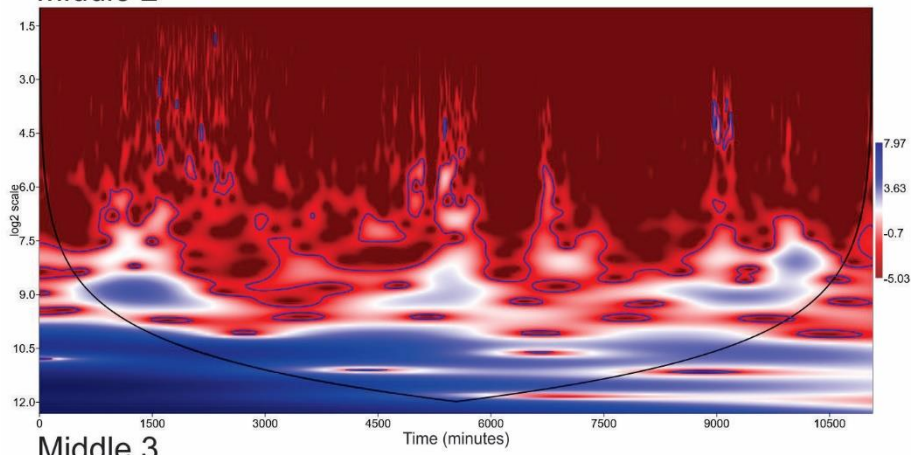
Top 3



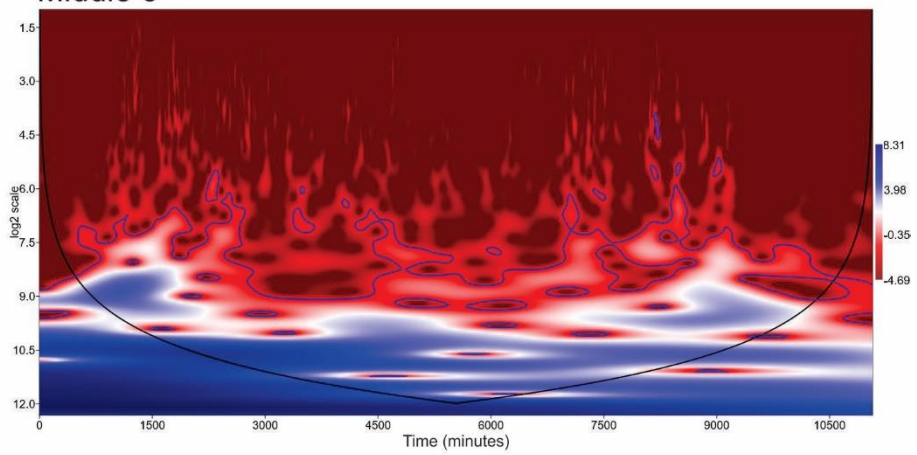
Middle 1



Middle 2



Middle 3



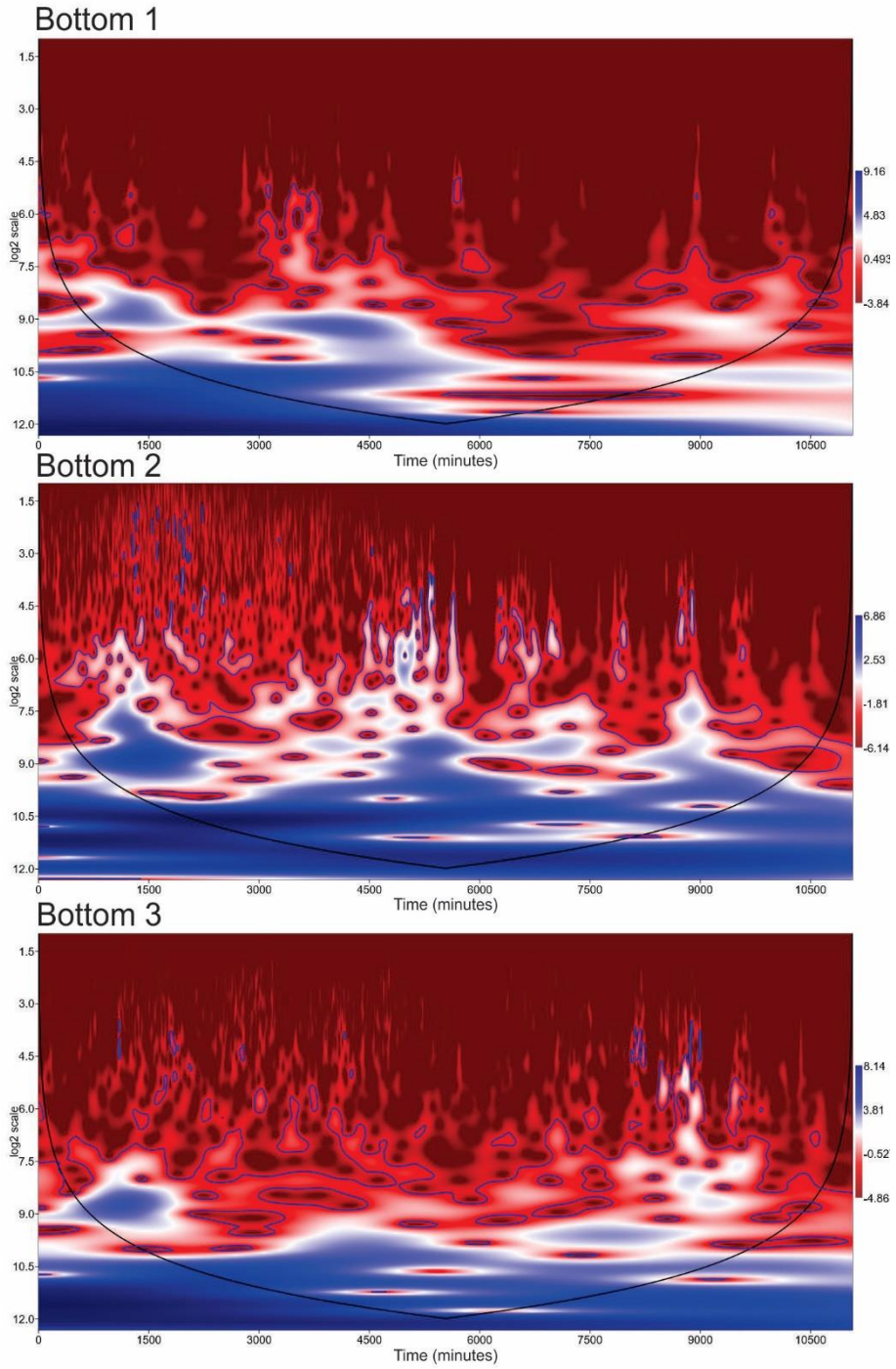


Figure 32: Wavelet transform using the Morlet wavelet on the lake-temperature sensors (Top 1-3, Middle 1-3, Bottom 1-3). Across all sensors there is 24-hour scale shared variance. This indicates that all the temperature sensors are responding, in part, to diurnal changes in water temperature.

5.3.3 Spatio-temporal flow patterns

The aDcp relies on the Doppler effect to measure the velocity and direction of flow within the water column of the lake. It was mounted to a Sea Spider platform and deployed on the lake floor in 31 metres of water. Water temperature at 31 metres depth was approximately 10°C throughout the entire study period. The cells were set up with a field of view (FOV) that spanned the lowermost 20 metres of the water column at intervals of 2 metres. See Chapter 4 provides a full description of the aDcp deployment.

Analysis of the velocity profiles show trends in the data. The most noticeable trend is that higher current velocities are observed at the top of the graph in cell 10, which suggests that turbidity currents were lofted above the bed and flowed above the aDcp as interflows. It is possible that turbidity currents could have also flowed along the bottom of the lake, <1 metre in thickness and below the FOV; however, this would be unusually thin for a turbidity current in Lillooet Lake (Best et al., 2005).

The maximum current velocity recorded was 159 cm s⁻¹ in cell 10, at the very top of the aDcp's field of view (FOV). Cell statistics for the period of observation are shown in Figure 35, which shows box and whisker plots of flow velocity for each of the aDcp cells. Flow velocities observed within each of these cells increase from the bottom of the bed to the top of the FOV.

Flow direction is measured in compass headings (e.g. 0° – N, 180° – S) and flow is referred to from which it is originating from. The prevailing current direction from cells 1-9 (1-19 metres above the lake bed) is from the WSW (236.25° - 258.75°; Figure 34). The prevailing direction of the higher velocity currents in cell 10 (19-21 metres of water)

is from the West ($258.75^\circ - 281.25^\circ$; Figure 34). These higher velocity currents appear to be directed straight off the delta front where incoming river water is directed. Given that the total water depth at this site is approximately 31 metres, this suggests that a turbidity current traveling as an interflow is flowing off the delta, above the aDcp, and into Lillooet Lake. There is a strong counter current between 5 to 16 metres depth directed from the SE along the axis of Lillooet Lake. Generally, the mean flow velocity of water from 1 to 5 metres above the bed is less than 6 cm s^{-1} .

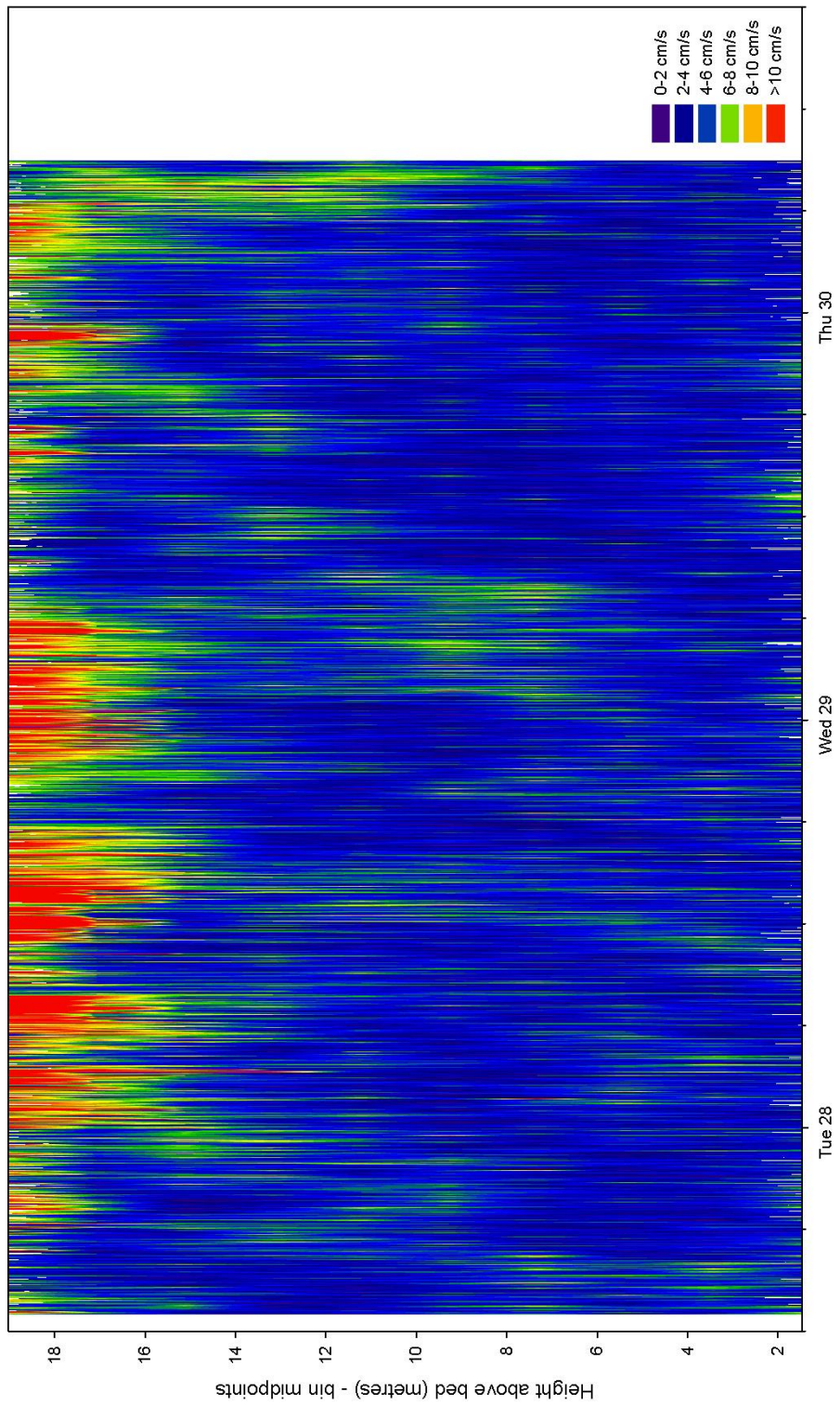


Figure 33: Current velocity measured by a bottom-mounted aDcp in Lillooet Lake. The aDcp was mounted in 31 metres of water and measured water to a height of 20 metres above the lake bed. Each of the 10 cells measured current

direction and velocity in 2 metre bins. A review of the data shows that the aDcp captured the bottom edge of inflowing river currents.

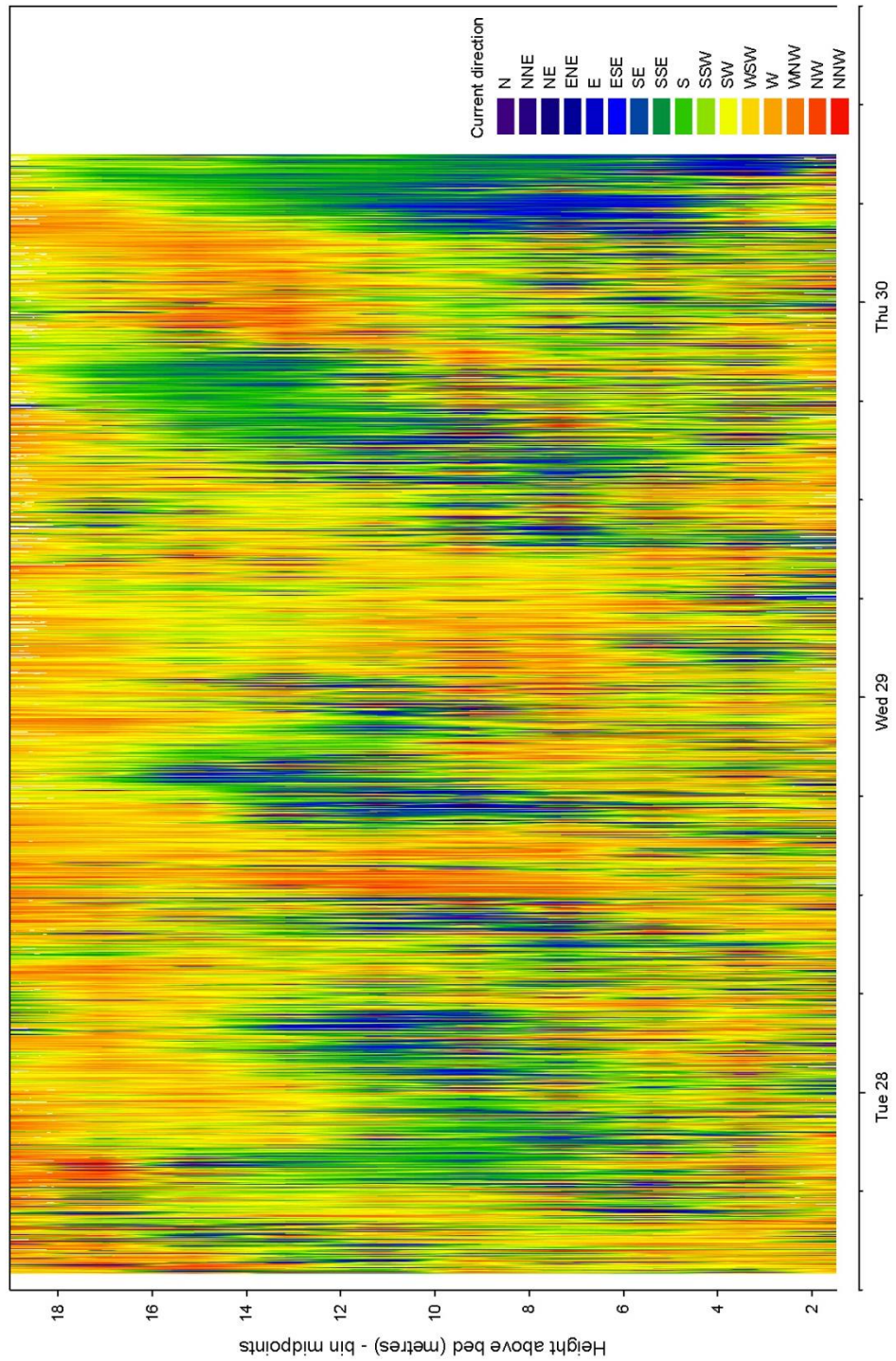


Figure 34: Current direction measured by a bottom-mounted aDcp in Lillooet Lake. The aDcp was mounted in 31 metres of water and measured water to a height of 20 metres above the lake bed. Each of the 10 cells measured current direction and velocity in 2 metre bins. After reviewing the data, it appears as though the aDcp captured the bottom edge of inflowing river currents.

of inflowing river currents. The orange shades show currents that are being directed from the front of the Lillooet-Green River delta. Blue and green currents are directed from down-lake, indicating the presence of counter-currents.

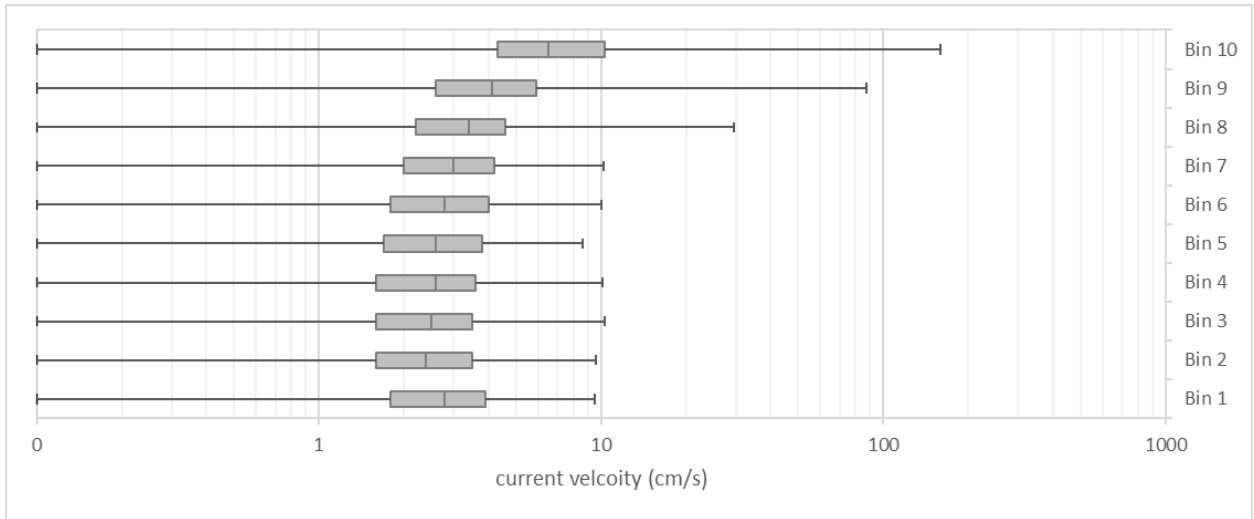


Figure 35: Velocity statistics from the 10 cells in the aDcp. The trend is for current velocity to increase with increasing distance from the bed. The bar is the range between the upper and lower quartiles, with the black line being the median current velocity. The outer bars represent the lowest and highest flow events recorded in those cells.

A comparison of lake current velocity between 19 - 21 metres above the lake bed (Cell 10), river stage data, and river SSC data show no strong trends between aDcp data and the river variables that were monitored (Figure 36). Peaks in river stage do not seem to correspond directly with high or low lake current velocities, nor do peaks in the river SSC data. Several peaks seen in the lake current data occur on the shoulder of increasing and decreasing river stage.

Figure 37 and Figure 38 are example plots of the aDcp data as a colour ramp, classified current direction, and plot of the corresponding Cell-10 current velocity. The plots appear to capture the bottom edge of interflowing turbidity currents as they pass above the aDcp. The bottom edge of the currents extends downward as far as 8-9 metres in some instances in large billows. The plots appear to show a periodicity to the velocity peaks. The peaks observed in the current velocity seem to occur at approximately 3-4-

minute intervals, with some velocity peaks being sustained for 10 minutes or longer. The high velocity flows off the delta front are not always visible in the data, and there are some small counter-currents that interrupt this flow, possibly due to shifting positions of the current, an interruption of the current, or increased buoyancy of the current above the aDcp FOV.

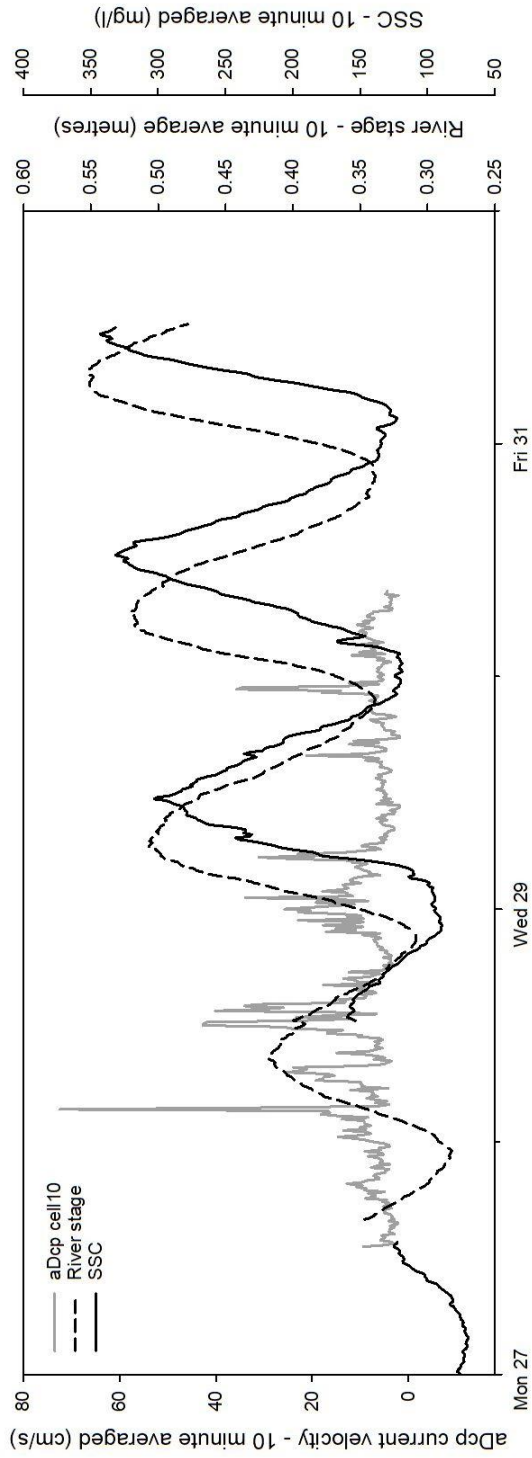


Figure 36: aDcp, river stage, and SSC timeseries. For plotting purposes, all data is averaged per 10 minutes.

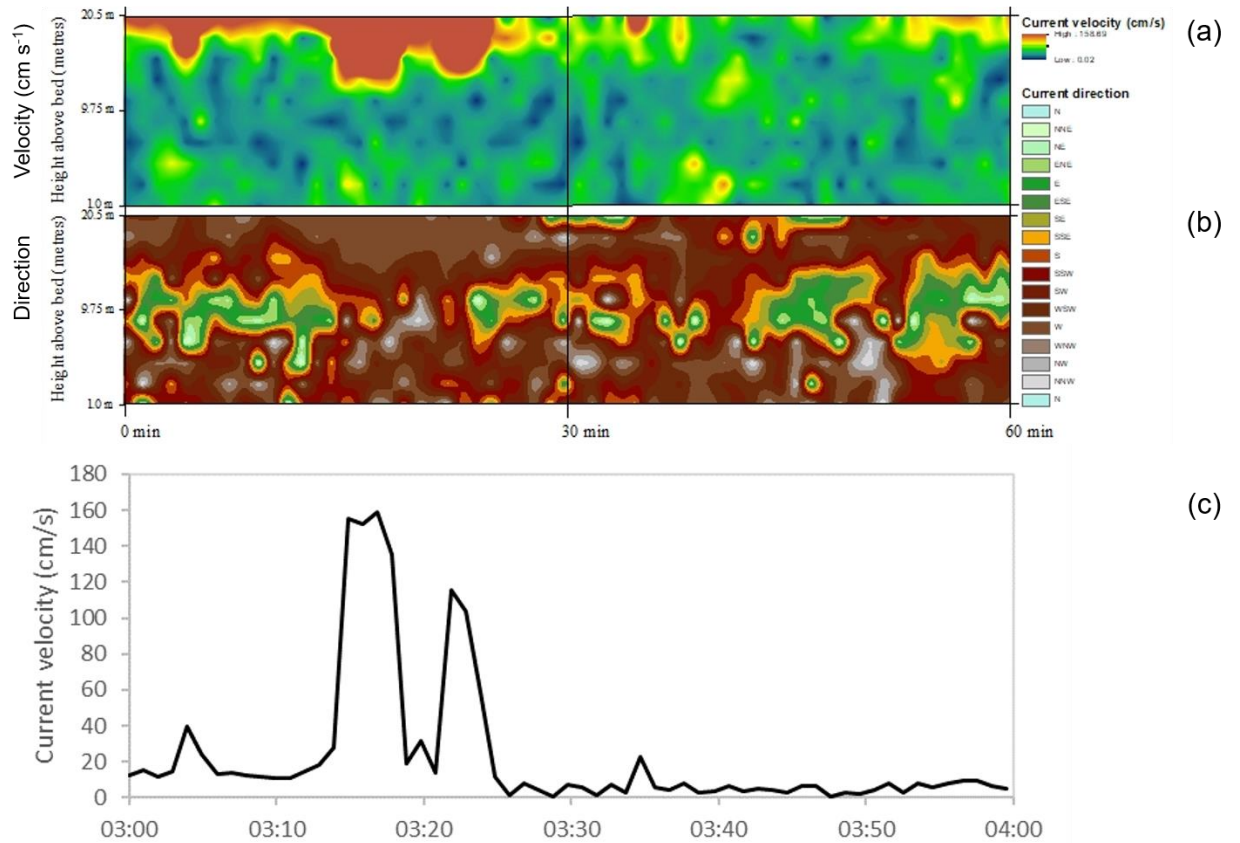


Figure 37: ADCP data from 28-July-2015. Panel (a) shows current velocity of all 10 cells on a hot-cold colour ramp. Panel (b) shows current direction data for all 10 cells by 16-point compass direction. Panel (c) shows the velocity profile of Cell 10 (18.55-20.5 m). The large peak in current velocity beginning at 03:15am is the largest current velocity measured during the period of record. Peaks in current velocity tend to occur at 3-minute intervals. Most peaks last only 1 minute, although the larger peaks were recorded up to 3 minutes in duration. The large peaks in current velocity appear to extend down in the water column.

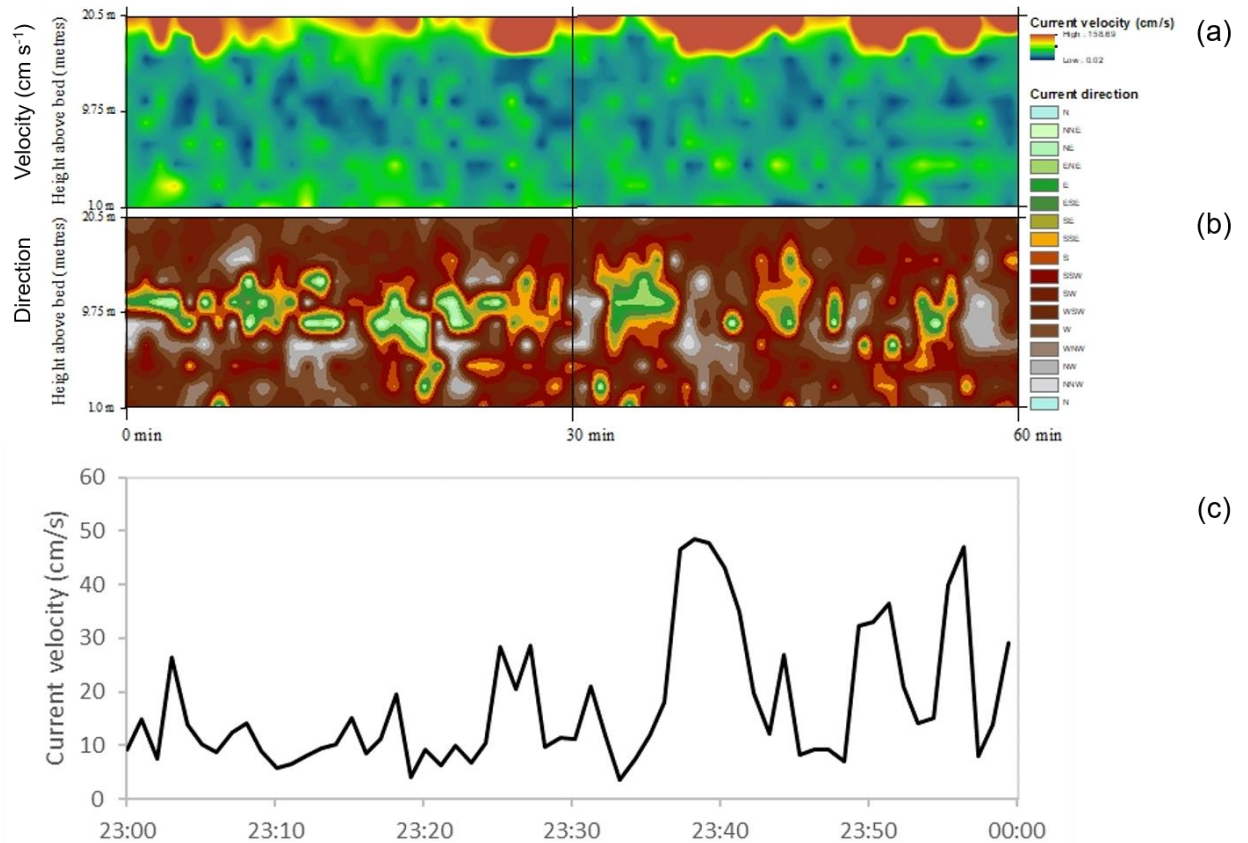


Figure 38: ADcp data from 28-July-2015. The top plot shows current velocity of all 10 cells on a hot-cold colour ramp. The currents at the very top of graph appear to extend down into the water column, some last for several minutes, and this current appears to billow possibly due to turbulence at the interface. The middle plot shows current direction data for all 10 cells by 16-point compass direction. The bottom plot shows the velocity profile of Cell 10 (18.55-20.5 m). Cell peaks appear to occur every 3-4 minutes regularly. The large velocity peak on the bottom plot at 23:35 lasts for 10 minutes before falling again.

Wavelet transformation analysis was conducted on the raw aDcp current velocity data from Cell 10, where the primary current direction was from the delta front. Figure 39 shows both a Morlet wavelet and a DOG-2 (Derivative of Gaussian, 2nd – derivative) wavelet, also known as a Mexican Hat wavelet. The white-red colours bounded by the blue lines represent the areas with highest power. The blue lines are the 95% confidence limit using the white-noise model described in detail in Torrence and Compo (1998) (Hammer et al., 2001). The black line that forms a boundary around the edge of the data

is the Cone of Influence, which shows the boundary between the time-series where edge effects may produce errors within the data (Torrence and Compo, 1998). Both wavelets show the same general trends although they appear quite different. There are global patterns observed in the data with periodicities between $2^{8.5}$ to $2^{10.5}$ minutes (6 to 24 hours). Throughout the time-series there are periods of smaller periodicity that occur between 2^1 and 2^8 minutes (2 minutes to 4 hours). These occur less frequently but are still significant over the time series (as measured by the significance line).

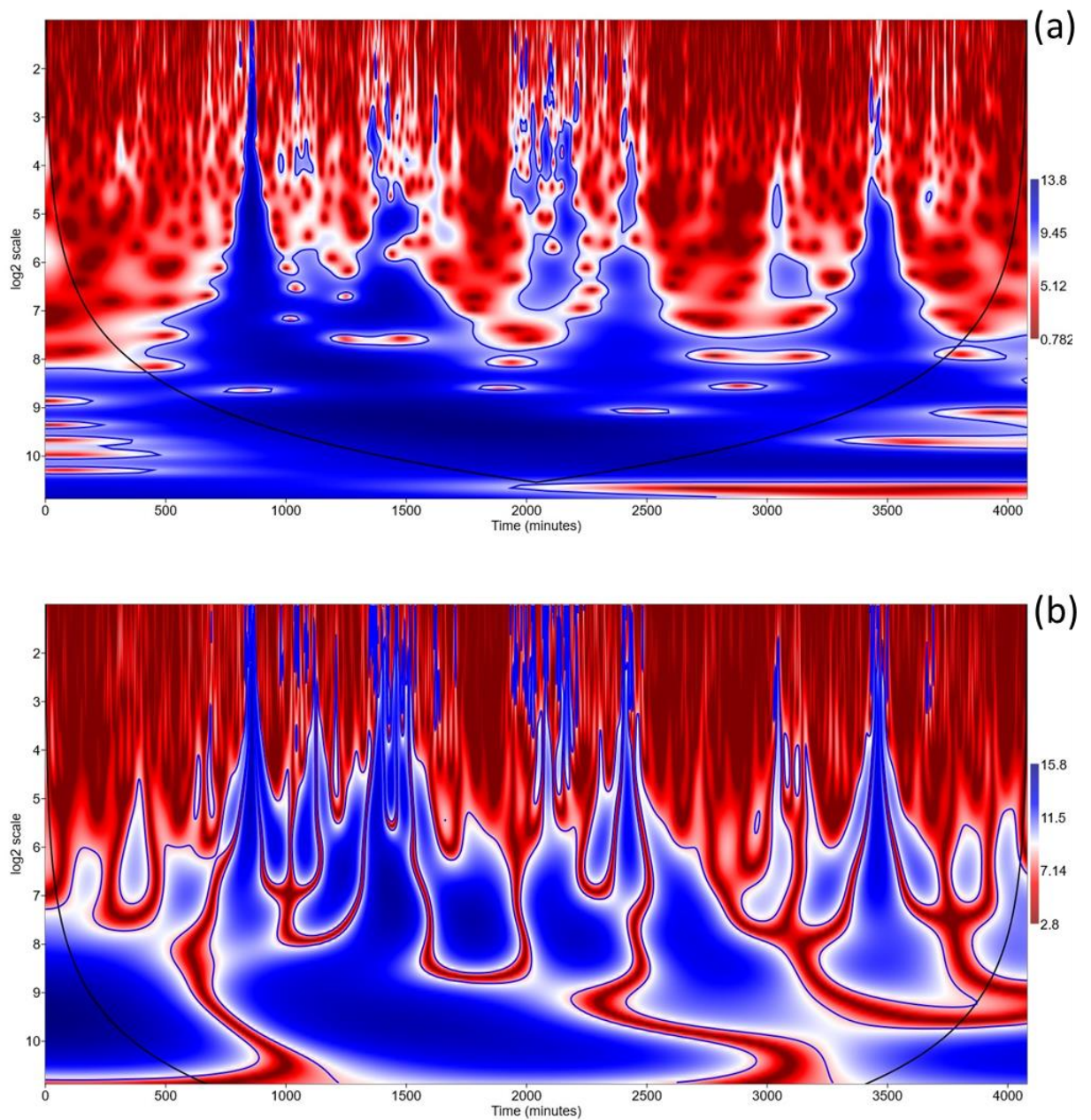


Figure 39: Wavelet analysis of the aDcp cell 10 data. The top graph shows the Morlet wavelet transformation and the bottom graph shows the DOG-2 wavelet transformation. Both graphs show the time series (minutes) along the bottom X-axis and the logarithmic-scale (base 2) on the y-axis. The data show that from a time-scale of $2^{8.5}$ to $2^{10.5}$ minutes there is global periodicity in the data along the entire time series. At smaller time-scales 2^1 to 2^7 there is periodicity that is observed at certain times throughout the data.

5.3.4 Water column properties

Water profile data was collected throughout the proximal basin of Lillooet Lake. Near the Lillooet-Green River delta cast were taken in a regular grid pattern on 29-July and 30-July. On 29-July, 4 additional water column profiles were collected. The location of these profiles is shown in Figure 40. Water profiles were collected using a YSI 6600-v2-4 castable CTD. Data were collected every second as the device was lowered through the water column on its descending path. Once the device landed on the bottom, it was retrieved. Water quality and physical parameters were analyzed from the descending cast to describe the water column. The methodology is further described in Chapter 4. The variables of most interest for the calculation of water density include were depth (pressure), water temperature, salinity, and suspended sediment concentration, which when processed can be used to calculate the bulk density of the water column:

$$\rho_f = \rho_w(Sa|T|P) + C \cdot \rho_s \quad (23)$$

Where ρ_f is the bulk density of water, ρ_w is the density of water as a function of Salinity (Sa), Temperature (T), Pressure (P), ρ_s is the density of suspended particles and C is the concentration of suspended sediment (by volume) within the water. P can be set to 0 then we can solve for ρ_w using Equation 23 (Lewis, 1980; Gil, 1982). The equation calculates water density from water temperature and total salinity. The effects of pressure have been omitted here as they are negligible on density for all but the deep ocean (Gil, 1982).

Salinity can be calculated from a simplified version of the Practical Salinity Scale 1978 which omits pressure (Schemel, 2001). This scale calculates salinity in PPT or PSU

(parts per thousand or practical salinity units) from specific conductance measured in millisiemens per cm ($mS\ cm^{-1}$).

$$Sa = K_1 + (K_2 * S_C^{1/2}) + (K_3 * S_C) + (K_4 * S_C^{3/2}) + (K_5 * S_C^2) + (K_6 * S_C^{5/2}) \quad (24)$$

Where the K variables are coefficients defined as $K_1 = 0.0120$, $K_2 = -0.2174$, $K_3 = 25.3283$, $K_4 = 13.7714$, $K_5 = -6.4788$, $K_6 = 2.5842$, and S_C is the ratio of sample specific conductance at 25°C to that of standard seawater at the same temperature. The CTD also directly measures TDS in PSU which can be used as a sanity check to verify the equation.

Finally, the effects of suspended sediment are added to the density of water to calculate the effects of suspended sediment on water density. The profiles of density, SSC, temperature, and conductance are shown in Figure 41 and Figure 42 and Figure 43 water profile plots.

An analysis of the water profiles A-Q suggests that distinct turbidity currents were only observed on profiles J-M, where the excess suspended sediment is greater than what is observed in the ambient lake water.

Water profiles J-M were taken on 30-July. Profiles J-L were taken in the same position as profiles A-C. Profile M is taken out front of the plunge line on that day. Profiles J-L show a distinct interflowing turbidity current has formed, as seen by the high SSC between 5-15 metres depth, making this flow thickness at these depths 10 metres. Profile M has the highest SSC located near the lake bed. The highest SSC is about 115 $mg\ l^{-1}$ within the plume and located at the very bottom indicating the passage of an underflowing turbidity current at this location.

Other lake profiles (A-I, N-Q) show the thermal stratification of Lillooet Lake. From these profiles, it appears Lillooet Lake has three distinct layers that are well developed. The surface layer, or epilimnion, is characterized by warm water that is well mixed and heated by the atmosphere. Salinity expressed as specific conductance in the epilimnion is quite low and consistent throughout the profile ($40 \mu\text{S cm}^{-1}$). Below this is the metalimnion or transition zone. The bottom layer, or hypolimnion is shown on water profiles that extend below 30 metres depth. This layer seems to be characterized by much colder water, less sediment-rich water that is also much higher in salinity expressed as specific conductance with values of approximately $70 \mu\text{S cm}^{-1}$ throughout the profile of this strata.

Water profiles A-C are the exception to the 3-layer profile. These profiles are in only 20 metres of water, near the front of the delta. The physical characteristics of the profiles at these locations suggests this is epilimnion water based on the lower specific conductance and temperature gradients present. Deeper water profiles also suggest the surface of the hypolimnion is found near 30 metres depth.

Comparison of the data from the aDcp at the time of the CTD casts shows no significant turbidity currents passing during this time. The maximum current velocity was 9.5 cm s^{-1} recorded by the aDcp during the time of the lake profiles. This lends to the idea that the turbidity currents are either breaking up or shifting during these periods.

The thermal structure of the lake shows colder, more dense water underneath warmer water at all profile locations. It also shows an increase in specific conductance in deeper water, which would further add to the density gradient observed. The passage of turbidity currents in Profiles J-M show higher SSC values that intrude into the water

column. At the same depths that the higher SSC values are occurring, lower conductance values are also recorded, which is not seen on the other lake profiles.

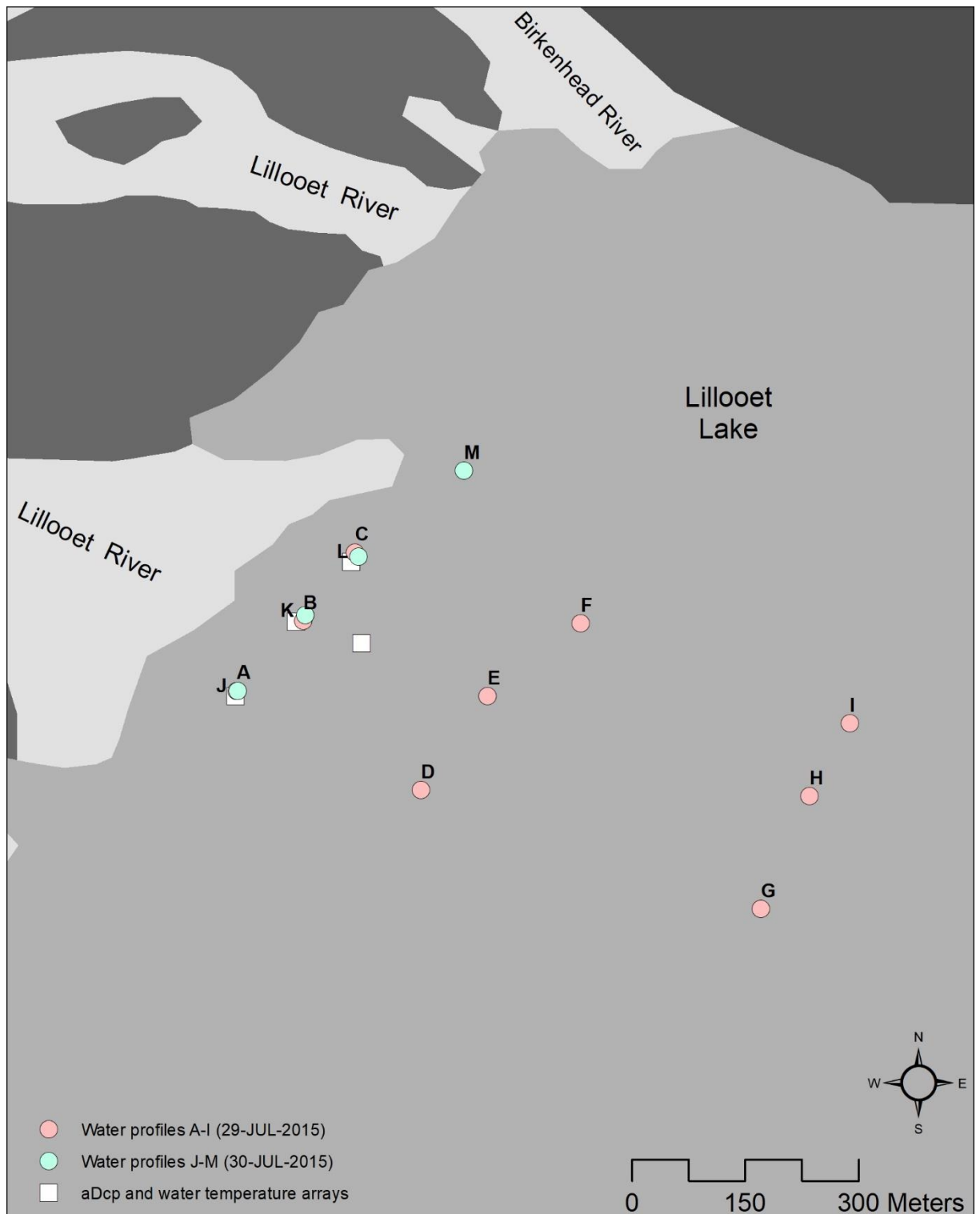


Figure 40: Map showing the location of water profiles collected using a castable CTD. Profiles A-I were collected on July 29. Profiles J-M were collected on July 30. An interflow was observed at profiles J-L and an underflow was observed at profile M.

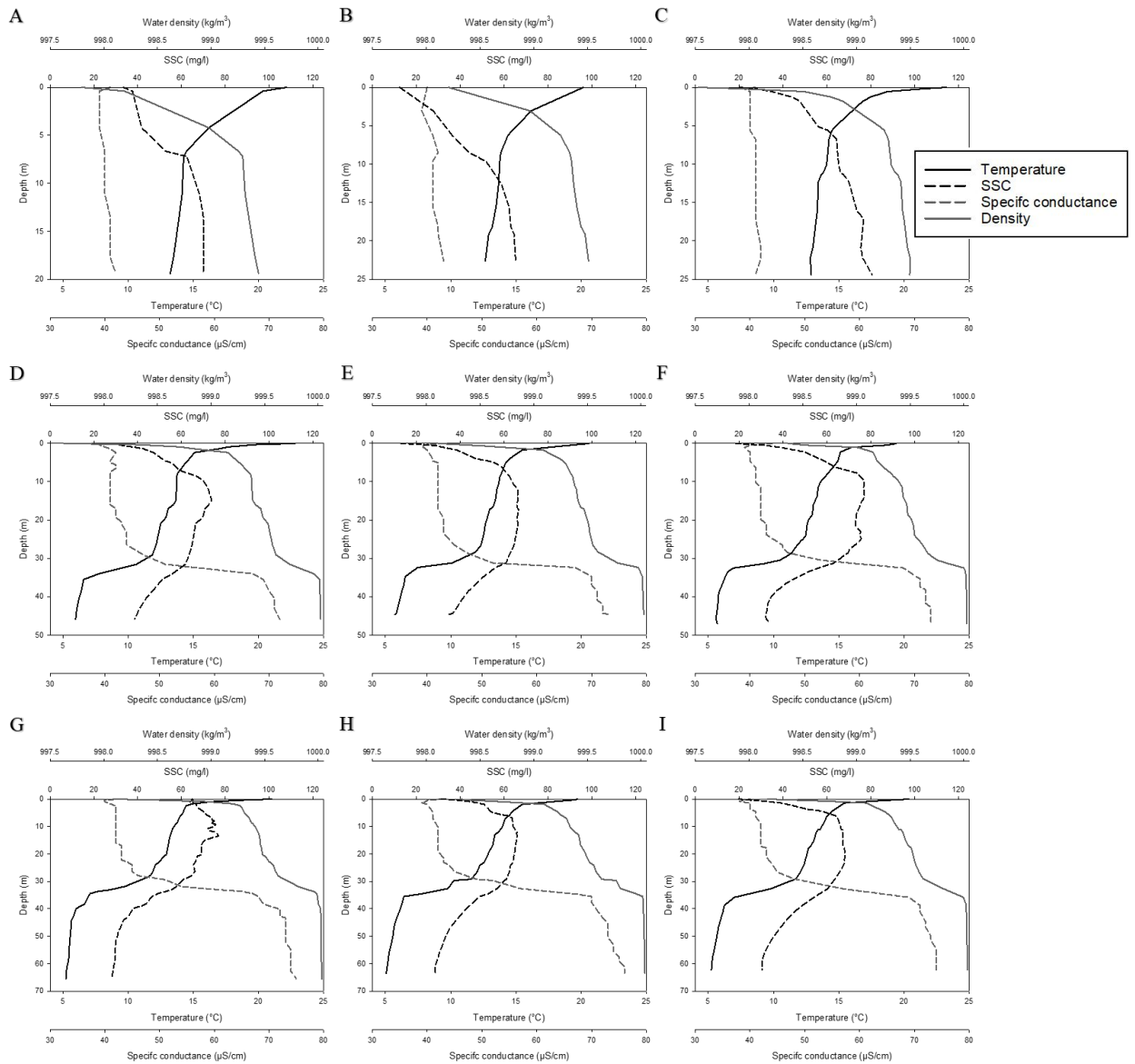


Figure 41: Water profiles from July 29. Profiles A-I are shown. The casts at these locations show no evidence of an intruding underflow or intercurrent entering Lillooet Lake from the delta. The abrupt change observed at 30 metres depth appears to show the stratification of Lillooet Lake, with the warmer metalimnion above and much colder, denser hypolimnion below.

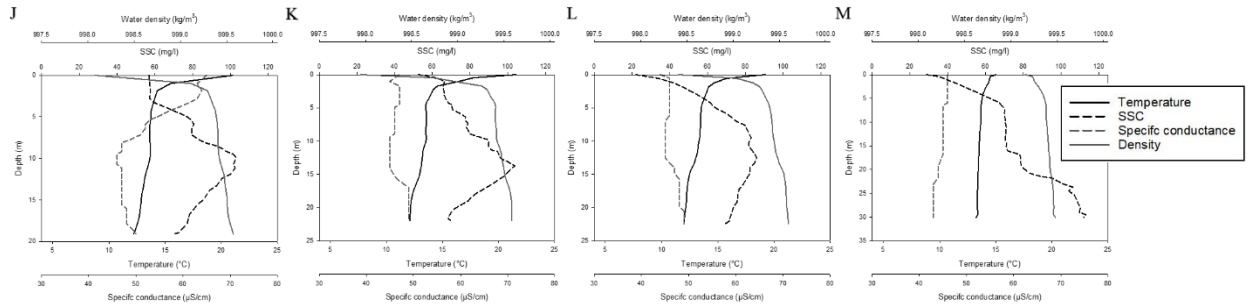


Figure 42: Water profiles from July 30. Profiles J-M shown. These casts appear to show the intrusion of an interflow (J-L) and an underflow (M) entering Lillooet Lake. This flow is characterized by a much higher SSC. The specific conductance and temperature profiles of these flows do not show significant difference from the surrounding ambient water which already have a very low specific conductance and cool temperature profile.

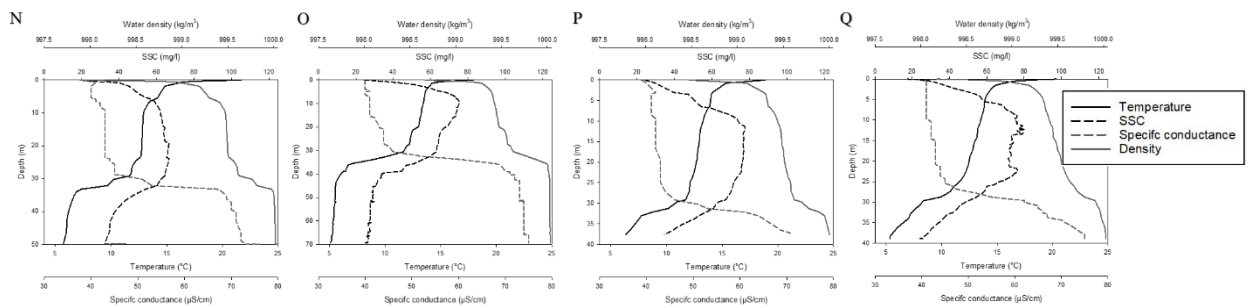


Figure 43: Water profiles from July 29. Profiles N-Q shown. These profiles were taken much further away from the delta than previously reported profiles in much deeper water. The casts show the stratification of Lillooet Lake with a thin hypolimnion at the surface, a 30-metre thick metalimnion and cold, dense hypolimnion that extends to the bottom of the lake.

5.3.5 Froude number calculations

The densiometric Froude number distinguishes between subcritical and supercritical flow (Chapter 2). It can be calculated by the ratio between flow velocity and the square root of inertial and gravitational forces (Equation 10). Subcritical or stable flow has a Froude number < 1 . Supercritical or unstable flow has a Froude number > 1 and is dominated by inertial forces. Froude numbers were calculated for the turbidity currents observed as interflows and underflows seen in Profiles J-M. Flow thickness and

density data were obtained from the CTD water profile data and a range of flow velocity values were obtained from the aDcp from July 29-30.

A mix of subcritical and supercritical flows were calculated based on the range of velocity data observed. The highest flow velocity reported by the aDcp, on July 28, was 159 cm s^{-1} which would produce supercritical Froude values at all locations, with $F_{\text{max}} = 19.8$ and $F_{\text{min}}=4.0$. The results in Table 5 suggest that the flows could range from subcritical to supercritical depending on changes in water velocity. The aDcp data is the only available flow data for turbidity currents in this study and is used as a representative value of currents and may misrepresent the actual flow conditions, especially at Profile M, where an underflow formed. Table 5 shows Froude numbers, flow thickness values, and estimated velocities using the aDcp data at each profile location.

$F_{6.8}$ values were subcritical at all points, but approaching $F=1.0$, or the critical flow value. Critical flow would indicate a transition between supercritical to subcritical flow and would indicate a point of deposition at this location.

Table 5: Water profile properties in front of Lillooet delta. Froude number subscripts refer to corresponding flow velocities in centimeters per second. Flow at higher velocities are supercritical at all water profile locations but with lower velocity ($F_{6.8}$) flow is just barely subcritical indicating a transition to a depositional environment.

Profile location (distance from plunge line)	Flow thickness (metres)	Flow classification	Max. SSC (mg/l)	F₁₅₉	F₄₉	F_{6.8}
J (85 metres)	9	Interflow	103.2	19.8	6.1	0.8
K (65 metres)	10	Interflow	103.9	16.9	5.2	0.7
L (60 metres)	10	Interflow	86.1	14.8	4.6	0.6
M (50 metres)	9	Underflow	113.3	18.8	5.8	0.8

6 Discussion

6.1 Relationship between flow velocity and sediment concentration transportation

During the period of study, discharge on Lillooet River was very low. The flow hydrograph during this time showed that flow was the lowest or near the lowest it has ever been in the period of record from 1914-2016. This unexpectedly low discharge appears to have produced a very non-dynamic environment for the observation and measurement of turbidity currents in Lillooet Lake. The mean flow over the period of study was $192 \text{ m}^3\text{s}^{-1}$, whereas the average mean flow over the period of record for that same period of the year is $308 \text{ m}^3\text{s}^{-1}$, which represents flow that is 46% higher. The low flows that were experienced during this time are thought to be a result of the extensive smoke that covered southwestern BC during this time as a result of forest fires (BC MFLNRO, 2015). Smoke in the atmosphere would have lowered the input of shortwave radiation in the energy balance on the melting ice, resulting in less melting and therefore meltwater availability. The pyranometer that was set up at the Lillooet-Green River delta showed that daily peaks of incoming radiation ranged from 356 W m^{-2} to 908 W m^{-2} . There were two days where cloud cover was observed, and the peak daily radiation during these times were 356 and 407 W m^{-2} . Other than these two days the sky was mainly cloud-free and daily radiation values reached between 699 to 908 W m^{-2} . During these days smoke was visible in the valley. Although the pyranometer was installed on the delta, the glaciers that are responsible for most of the discharge into Lillooet River are located at higher elevations hundreds of kilometers away. Most likely, the effects of smoke were much worse at these locations, which were also much closer to the actively

burning forest fires at the time, making the sky much more obscure than at the Lillooet-Green River delta. This is likely to be the cause of decline in flow values relative to an average year.

Also noted during this period, were three days where rain was reported in Pemberton (Pemberton MSC). The spatial-extent of the rain is unknown but there did not appear to be any corresponding peak in the hydrograph resulting from these rain events. This may indicate that the rain had a very limited spatial effect and that it was not present at higher elevations where rain may have enhanced glacial melting.

At the Lillooet-Green River delta, where a pressure sensor was installed, the river stage had a range of 0.27 metres of height over this time. During the period of coincident SSC measurement, the range of river stage was 0.20 metres. Within this small range of river stage there was a wide range of SSC measured. Suspended sediment concentrations of 89-333 mg l⁻¹ were measured. In comparison to other monitoring studies on Lillooet Lake this is a low concentration of sediment to be transported by Lillooet River. Gilbert (1975) recorded an SSC peak of over 3,000 mg l⁻¹ on 05-August-1971, during that study, which is almost 10x the peak recorded by this study. Other studies of suspended sediment in proglacial alpine lakes show much high peaks of SSC (Table 1). The exception to this was the study by Schiefer and Gilbert (2008) on the meltwater being directly discharged from the Lillooet Glacier into Silt Lake (upstream of Lillooet Lake).

Based on a review of the literature (Guthrie et al., 2012) and by comparing the timing of peak melt to peak flow it appears as though the basin lag time may be estimated at approximately 14±2 hours from the head of the watershed to the Lillooet-Green River delta and the relationship between sediment and flood peaks show counter-clockwise

hysteresis. This relationship shows that peak SSC occurs on the receding limb of the flood wave and that peak SSC lags peak river stage by between 5-6 hours. Using the index proposed by Lawler (2006), HI values of -1.4 and -1.6 were calculated. As has previously been discussed, most hysteresis in glacial basins tends to be clockwise (positive) although there are exceptions. Reasoning for negative hysteresis has ranged from increased sediment concentration from tributary streams on the receding hydrograph flow, upstream bank failures on the receding hydrograph flow, large distances between the gauge and sediment sources, or sediment depletion with the channel (Bača 2008; Landers et al., 2013; Lawler, 2006; Mao and Carrillo, 2017).

There could be several reasons for counter-clockwise (negative) hysteresis observed on Lillooet River. In the Lillooet River basin, much of the sediment supply is believed to be a result of hillslope processes within the drainage basin rather than directly from Lillooet Glacier. Meager Creek contributes a disproportionately high load of sediment into Lillooet River, given its drainage basin size (Bovis, 2000; Friele, 2004). Because of these unconventional sediment dynamics in Lillooet River that may be quite unique to Lillooet River, it could be that the timing of sediment transport from Meager Creek corresponds to the falling limb of Lillooet River. It may also be that after the diurnal peak, bank slumps occur, especially in the debris field of the 2010 Mount Meager landslide (Guthrie et al., 2012). Another possible explanation may be that the river lacked the required capacity to carry larger quantities of sediments than during previous studies and at other times, meaning more sediment may have been deposited in-stream during our observations and that this sediment will have been flushed out once river discharge returns to a more normal level. At Slims River, Yukon, counter-clockwise hysteresis was

noted, and possible explanations by the researcher to account for this ranged from bank slumping or a change in the origin of the meltwater between the rising and falling limbs of the hydrograph (from supraglacial to subglacial; Crookshanks, 2008).

Although bank slumps into the river may account for counter-clockwise hysteresis in some studies, it is likely not the situation at Slims River or in this case at Lillooet River, where bank slumps would have to occur on a continual daily basis to account for the continuous counter clockwise hysteresis. Changes in the origin of meltwater, as proposed at Slims River (Crookshanks, 2008) could account for this; however, sudden regular daily shifts in the melting regime of an alpine glacier have not been reported in the literature and this would require a close study of the mass balance of the glacier.

Past studies have shown that the source of sediment in Lillooet River is diverse, with glaciers, bank slumps, incision of landslide deposits accounting for most of the sediment being transported by the river (Slaymaker et al., 2017). The diversity of sediment supply further tangles the question. In the Lillooet River, a factor that could play an important role in sediment timing dynamics is the relatively recently formed Silt Lake at the terminus of Lillooet Glacier. Silt Lake may have a greater impact on attenuating the sediment peak than the flow peak, which eventually flows into Lillooet Lake. This theory suggests that Lillooet Glacier is responsible for most of the flow and sediment production in Lillooet River, which as has been pointed out may not be the case (Slaymaker et al., 2017). In either case, it appears that the main sources of discharge and sediment in the Lillooet-Green River are decoupled and are not tied to the same processes.

6.2 Changes to the Lillooet-Green River delta

The most visible change to Lillooet-Green River delta is on the surface of the delta where large lateral migration of the main channel was measured. At the outer edge of the delta the amount of erosion measured was 159.8 metres from July 16 to August 9, 2015, which comes to an average rate of 6.4 metres per day. At one point during the field study the meteorological station needed to be moved to avoid collapse in the Lillooet-Green River. As the river channel migrated laterally throughout the course of the study, it was eroding the northern edge of the channel. The erosion was observed to be non-linear, such that it was nearly stationary at the point where the river monitoring sensors were located and showed the greatest migration at the lake-ward edge. The sediment that was eroded was being deposited into the river where it appears to get carried into the lake. Although no sediment samples were taken of the delta material, it is likely that this material represents either bedload or suspended load that has previously been deposited and now remobilized (Gilbert, 1973). This sediment would have added to the suspended sediment load that was being carried by the river being flushed into Lillooet Lake. On the opposite bank the channel edge was seen to be aggrading, although no measurements were taken on this bank.

Observations of UAV and satellite imagery during this time show that the plunge line forms near-perpendicular to the flow of river water entering Lillooet Lake. The plunge line forms a visually distinct boundary between inflowing river water and ambient lake water, where both are entrained and plunge beneath the surface of the lake. At the northern edge of this boundary a single lobe was observed to extend outward from the plunge line, parallel to the flow of river water which is generally in line with the eroding

shoreline. Along the edge of this flow, K-H instabilities were observed. The lobe appears to change position as the eroding channel moves, indicating a direct relationship between the position of the lobe and the lateral migration of the north channel. The lobe that extends further out appeared to collect debris. Water column profiles taken at the end of the lobe showed greater SSC than those in front of the perpendicular plunge line, which would indicate that sediment is being preferentially directed towards this lobe and discharging into the lake as a turbidity current. The extension of this lobe beyond the rest of the plunge line is likely a factor of the higher SSC within it, as previous studies have stated that the plunge line extends further into the lake with increased flow velocity (Lamb et al., 2010). Although no direct measurements were made, observations of the channel indicate flow velocity was also higher on this side than on the far side, which supports the observation that the north bank of the channel is eroding while the south bank is aggrading. This means there is a strong velocity gradient along the longitudinal profile of the plunge line with the maximum energy observed to be at the lobe.

The bathymetric survey uncovered several distinctive features about the bottom of Lillooet Lake. The subaqueous portion of the delta appears to be aggrading at a rapid rate, as indicated by the steepening of the delta slope. Measurements taken from the bathymetric survey show that the top of the slope appears to have aggraded by 3.0 to 7.7 metres between the two cross sections. This level of aggradation is not uniform throughout the slope in an offshore orientation and the slope gradually decreases to no discernible change in bed height by about 100 metres offshore (15-20 metres water depth). While this amount of change on the delta slope is immense, the over-steepening of the delta front cannot continue indefinitely. The slope of the delta foreset increased

from between 21-24% grade from 22-July to up to 33-67% grade on 31-July. This buildup at the head of the slope will undoubtedly induce a slope failure, resulting in this aggraded material being dispersed further down slope and further out into the lake basin. This could result in a large surge-like turbidity current. During this study there was no indication that such a failure occurred, but these types of failures have been observed to occur in other lacustrine environments (Lambert, 1988). It is also interesting to observe that Cross-section A-A' recorded a higher rate of accumulation than Cross-section B-B'. From the discussion above, the highest energy along the plunge line was observed to occur at the approximate location of Cross-section B-B'. The higher aggradation rate at a position of lower energy may indicate that more sediment is being washed out at Cross-section B-B' resulting in lower aggradation rates or else that the lower velocity at these points is resulting in deposition. An alternative answer could be that at some period between the repeat surveys, the slope failed resulting in a surge-like turbidity current and the bed height/slope at Cross-section B-B' on July 31 is the result of sediment reaccumulating.

Observations of the bathymetric data show a small low that is in line with the plunge line lobe. This depression may represent a channel or eroded surface at this location. Gilbert (1973) has previously document the presence of both in Lillooet Lake. Unfortunately, in this study, side-scan sonar was not available, so a more detailed examination of this feature cannot be made. If this is a channel it could indicate an area of preferential flow for water and sediment entering Lillooet Lake or it could indicate an eroded surface. Gilbert (1973, 1975) showed that large lobate mounds formed on the delta front. This feature could represent a trough between two adjacent mounds, although

no other topographic highs or lows were detected by these surveys. The resolution and type of bathymetric survey used did not lend itself to the detection of these small-scale features on the lake bottom.

6.3 Lake currents

The aDcp was deployed in 31 metres of water directly in front of the main channel on 22-July. During this time, it also recorded a consistent water temperature of 10°C. Based on this water temperature, depth, and data from the water profiles the aDcp was placed in the transitional metalimnion strata and therefore could view the bottom of the epilimnion. Unfortunately, due to the lateral shift in channel position, the aDcp was likely not directly in front of the main lobe by the time it was launched. The aDcp was set to record the bottom 21 metres of the water column, and therefore not the whole water column. This decision was based on a previous study of turbidity current monitoring using an aDcp in Lillooet Lake by Best et al. (2005) who found underflows and interflows occurred within the bottom 20 metres of water and that interflows occur at the transition between the epilimnion and metalimnion. The data from July 27-31, 2015 showed that the bottom 15 metres of the water column showed no real passage of an active turbidity current. What was observed, however, was the bottom boundary of the passage of an interflowing turbidity current into the lake. This interflowing current is believed to be the result of a turbidity current because of the limited temperature differential between river and lake water and the lower conductance of river water. The density differential then is most likely attributed to increased suspended sediment (as seen in Profiles J-M) which makes the flow a turbidity current. The aDcp does not appear to capture the top of the interflow therefore changes in flow thickness cannot be

measured. The flow statistics show the highest flow velocities appear at the top of the aDcp's FOV, and a maximum flow velocity of 159 cm s^{-1} was observed. The fast-moving flows at the top of the FOV are directed away from the delta which indicates that the currents are driven by the inflow of river water. This interflow appears to be a semi-permanent feature throughout the period of observation, with only a few small periods of time where the current appears to breakdown or else move outside of the aDcp's FOV. The inflow also appears within the epilimnion and not at the bottom interface which indicates flow is only marginally denser than the water around it. On 30-July, the current begins sinking more so than it has at any other time in the observation, indicating that the flow is gaining density relative to the surrounding water. No noticeable changes were observed in inflowing river water, sediment concentration, or water temperature that accounts for this change.

In a previous study in Lillooet Lake using an aDcp, pulses of the current velocity were observed (Best et al., 2005). These velocity pulses were reported to have a period of 3-12 minutes (Best et al., 2015). Within this study period, velocity pulsations were observed at the lower boundary of the interflowing turbidity current. These pulses occurred around 3-4 minutes when viewed from the graph. The wavelet analysis using both the Morlet wavelet and DOG-2 wavelet did not appear to show this periodicity very well throughout the time series but did show some periodicity between 2 minutes and 4 hours. This may be due to the irregular shapes of the periodicity not matching well with the mother wavelets or else oscillations that were interpreted as background noise. Other studies of inflowing water have commented on instabilities or pulses within the current velocity (Lambert et al., 1976; Wiseman et al., 1976; Smith et al., 1980; Chikita, 1989;

Kneller, 2000; Fer and Lemmin, 2001; Best et al., 2005). Explanations for these pulses range from instabilities observed within the currents (Kneller, 2000), long-period roll waves within thermal undercurrents (Fer and Lemmin, 2000), variations in river discharge and critical flow velocity (Lambert et al., 1976), responses to air temperature, SSC of inflowing water (Chikita, 1989), or dynamic changes caused by wave action, storms, tides, wind-driven circulation, unsteady river discharge, or slope failures (Best et al., 2005). Within this study, velocity pulses were observed on the lower boundary of the observed interflow. This lends some credence to the idea these observed pulses are due to shearing with the ambient lake water causing turbulent vortices (e.g. K-H instabilities). Whole-flow velocity pulsations, like those observed by Best et al., (2005) were not observed in this study, mainly because the whole flow was not observable.

The water profiles that were taken on 29-July and 30-July show that the lake has distinct strata. Profiles A-M were made in parallel lines at the front of the delta to show spatial variability in the water column. Profiles A-I show two distinct layers beginning to form as water deepens. The epilimnion transitions into the metalimnion at approximately 30 metres depth, marked by the sudden cooling of the water, increase in specific conductance, and decrease in suspended sediments. From profiles A-I it does not appear as though a distinct underflow or interflow is occurring at these profile sites, which should be seen by an intrusion of sediment rich water into the epilimnion. Review of the aDcp data shows that during the profile casts (29-July), the interflow appears to break down or else move outside of the FOV. Profiles A-I do show the sediment-rich epilimnion (SSC ~ 60-80 mg l⁻¹) that does not appear to decrease significantly in sediment concentration throughout its thickness, even at much further and deeper

locations (profiles N-Q). It may be that at these locations and at this time that the sediment plume coming off the delta is being mixed into the ambient lake water, although no sediment plume extending further into the lake was observed outside of the plunge line and lobe.

On 30-July, the water profiles appear to show the passage of a turbidity current. This is seen as an interflowing turbidity current at Profiles J-L and an apparent underflowing current at Profile M. The differences observed in Profiles J-L compared to A-B is a thinner, much more sediment-rich layer of water that is intruding into the epilimnion at J-L. This intrusion is distinct from the rest of the water column and taken as the passage of a turbidity current along with its distinct lowering of specific conductance. Interestingly, the water temperature does not show any inflection which indicates that thermal characteristics are not as important during this time. At Profile M, a distinct underflow is occurring. This profile is taken in front of the plunge line lobe and is the only evidence of an underflow observed during this period of study.

6.4 Process connections

Several important observations were made that had an impact on the overall study and data that was collected for the study of turbidity currents. The first major observation appears to be the significance in the lack of flow observed on Lillooet River during this period. Turbidity currents in Lillooet Lake are driven by inflowing river water from Lillooet River and therefore the influence that Lillooet River has on the turbidity currents cannot be understated. Within past studies underflows and interflows were observed in Lillooet Lake. During these times, river discharge was reported to be significantly higher than at this time. The amount of river discharge is important for two reasons. First, higher

river discharge will bring a higher quantity of sediment into Lillooet Lake proportionally than lower discharge given the same volume of suspended sediment per unit of water (capacity). The second, probably more important point is that higher discharge is associated with a higher flow velocity and therefore more competence for sediment transportation. This would lead to a greater suspended sediment load being entrained within the river that would then be transported into Lillooet Lake. This shortage of flow and therefore sediment is likely to be influenced by local forest fires that reduced the energy available for melting glacier ice in the upstream valleys. The unfortunate result of the forest fires was that it provided for abnormally low discharge in the Lillooet-Green River and therefore reduced sediment delivery into Lillooet Lake.

The other very important environmental variable which was not considered and likely had a great impact on the outcome of this study was the lateral migration of the channel being studied. When the equipment was deployed, initially the river channel was in a far different spot than it was towards the end of the study (Figure 27). A difficult decision was made to not reposition the equipment throughout the course of study. The result was that the data collected may not actually represent the direct inflow of river water flowing off the delta. The plunge line dynamics observed both visually and through equipment deployments seems to indicate that the largest volumes of sediment are being directed to this lobe and not uniformly distributed across the plunge line. This was because higher rates of river velocity and erosion of the lateral bank were observed in-line with the lobe than at other spots along the plunge line. Inflowing river water from this plunge line is likely experiencing greater mixing with ambient water than that directed from the lobe which reduces the density of the current. While this should not be

surprising that faster flow was being preferentially directed at a specific point, it was not expected to have had such a great impact on the condition of turbidity current flow properties or differences in bathymetric properties. There has also not been any significant discussion of this within the literature. The discussion of the lateral variation of velocity rates along the plunge line is not discussed in turbidity current literature and is a topic of great interest arising from thesis work because it appears to have a significant impact on the development of the currents forming off of Lillooet-Green River delta.

While no meandering of the turbidity currents was observed during this study, the shifting of the channel within the delta has a direct impact on the location of the plunge line lobe and therefore the direction and location of the main turbidity current flow. This type of meandering is not necessarily expected but does highlight a very real limitation of point source measurements within such an environment. The point source instruments (water temperature moorings and aDcp) were deployed at a spot where the most active segment of the turbidity current no longer resided. Even if the sensor had been placed within this segment of the turbidity current, it may only have resided here for only a few hours to days before it was outside of the region of highest flow due to the rapid observed migration of the plunge line lobe. This is an issue that past studies have avoided due to their much shorter study period of at most several hours.

7 Conclusions

In summary, this study was initiated with three study objectives regarding the dynamics of river-sediment delivery and turbidity current flow in an alpine, glacial lake.

The research objectives are:

- | | |
|---|---|
| To document the relationship between suspended sediment and discharge rates in Lillooet-Green River | 1 |
| To document the variability of flow properties of turbidity currents in Lillooet lake. | 2 |
| To understand how bathymetric properties of turbidity currents are influenced by or influence the passage of turbidity currents at the front of Lillooet-Green River delta. | 3 |

To study these research objectives a field monitoring study was established at Lillooet Lake. During the period of study, discharge from Lillooet River was abnormally low, producing lower than expected flow rates and volumes of suspended sediment. Where an underflowing turbidity current was expected to occur regularly, intermittent interflows were observed. These factors presented obstacles to answering the three research objectives. While definitively answering the research objectives may not be possible given the field realities, it is possible to comment on each objective and draw conclusions based on those field observations.

During the period of incident river stage and river suspended sediment concentration, counter-clockwise hysteresis was observed. Counter-clockwise hysteresis is a relationship between river discharge and sediment concentration where peak flow occurs before the peak in suspended sediment. This phenomenon has been observed by

previous research but tends to be uncommon, especially in glacial lakes. In previous studies, the factors that account for counter-clockwise hysteresis tend to be oversimplistic and little evidence is given for the mechanisms behind it. The source of sediment entering Lillooet Lake is poorly understood but appears to be quite complex as Meager Creek and the MMVC deposits may represent a comparatively large amount of sediment that is entrained in Lillooet-Green River.

In this study, pulses within the current velocity were observed to occur at the lower boundary of the observed turbidity currents as they entered Lillooet Lake. When velocity pulses were observed, they occurred with a period of 3-4 minutes. Unfortunately, because we were not able to capture the whole flow field, comments on velocity pulsing within the whole body of the current cannot be made. From these observations of the velocity data it appears that these pulsations impact the lower boundary of the turbidity current. They may be the result of K-H instabilities at this boundary layer. The pulses, therefore, may be billows and eddies created by this turbulent mixing at the boundary. A fuller understanding of the velocity pulsation within the turbidity current was hampered by the fact that only part of the current fell within the field-of-view of the aDcp during the time of study.

The third objective was to understand how the bathymetric properties influenced the passage of turbidity currents. During multi-day passes with the sonar, the delta foreset beds appeared to increase in both height and slope, resulting in aggradation and progradation of the delta front. The increased slope also had the effect of steepening the delta foreset beds. The result of the increased slope is likely to be a collapse, which would cause a surge-like turbidity current to form. This type of turbidity current was not

observed in this study but could have the potential to carry large amounts of coarser bed-load material further out into the lake basin. Also noted in front of the delta were channels, or topographic lows that aligned with the plunge line lobe that developed off the north bank of the main channel in the delta. This low is believed to be an incised channel that has been eroded by strong underflows at this location.

Low lake water levels experienced during this time of study also gave me an opportunity to map the edge of the main channel throughout the course of the study. The mapping of the channel showed that it was eroding at a very significant rate but that the outer edge of this channel aligned well with both the plunge line lobe and the apparent benthic channel that developed. These linkages indicate non-uniform, preferential flow path of the inflowing river water and turbidity currents.

7.1 Recommendation for future work

The remoteness of the study site provided significant challenges. The only access to the site was by boat for over 10 km, which resulted in inaccessibility on unfavourable weather days. To help combat this issue, a longer-term program should be considered, which would also help to eliminate some of the large gaps in the data that were part of this study.

With the goal of this study being to collect whole-field monitoring of turbidity currents in order to visualize and identify physical properties of them, it is rather lucky that the equipment seemed to be outside of the main path of flow. The amount of sediment accumulation that was seen in the bathymetric comparisons, could have buried our equipment resulting in significant data (and equipment) loss. As was the case during

equipment retrieval, one temperature sensor buoy was significantly stuck within the sediment and almost lost. This also seems to indicate that bottom mounted equipment, especially this close to the front of the delta, may not be a good idea when monitoring a highly energized environment such as Lillooet Lake.

Future studies of turbidity currents in Lillooet Lake should build on knowledge gained from this study and explore the dynamics of the plunge line properties and bathymetry. One of the most interesting observations made was that the leading bank of the channel, plunge line lobe, and the benthic channel appear in-line. This dynamic likely indicates a preferential for underflows being directed into Lillooet Lake. A longer-term study of these processes could verify whether turbidity currents are transporting sediment preferentially into the lake along this path. Although it should be noted, evidence of interflowing turbidity currents existed across the entire plunge line.

The apparent velocity gradient along the lateral edge of the plunge line is also an important feature and likely has implication for particle transport and development of the delta foreset beds. A longer term (season-long) study should be considered when conducting this type of field work so that unexpected variability can be monitored at a longer term than was done here. This characteristic, while not unsurprising, was not expected to occur based on the literature. No previous studies have considered the horizontal variability in plunging water or the development of turbidity currents within lakes. This is especially true in laboratory experiments of plunging flow, where flume boxes are set up in cross-section of the flow only showing the X, Y dimensions.

During the field study, it was not fully understood what the hydrologic conditions on Lillooet River and Lillooet Lake were like in context to what would normally be

expected. Discharge and lake levels were abnormally low, so much so that they were now represent the lowest rates in the hydrometric record for that period. This lower energy environment appeared to be less dynamic than was expected for peak glacial-melt season and this had the result of producing less dense inflowing river water.

8 Literature Cited

- Akiyama, J., and Stefan, H.G. 1984. Plunging flow into a reservoir: Theory. *Journal of Hydraulic Engineering*, 110: 484-499.
- Allaby, M. 2008. *Oxford Dictionary of Earth Sciences*. Edited by M. Allaby. Oxford University Press, Oxford, UK. pp. 596.
- Bača, P. 2008. Hysteresis effect in suspended concentration in the Rybarik basin, Slovakia. *Hydrological Sciences Journal*, 53: 224-235. DOI: 10.1623/hysj.53.1.224.
- Barrett, D.C. 2014. The prevalence of bacteria-sediment associations and their effect on sediment settling velocities in aquatic environments of agricultural Saskatchewan and alpine British Columbia. M.Sc. Thesis, Department of Geography, University of Regina, Regina, Saskatchewan.
- Barrett, D.C., and Hodder, K.R. 2018. Bacteria-sediment associations in an alpine, freshwater environment and their effects on particle size, density and settling velocity. *Earth Surface Processes and Landforms*, 43: 2232-2242. DOI: 10.1002/esp.4389
- Bedient, P.B., and Huber W.C. 2002. *Hydrology and floodplain analysis*. Third edition. Prentice Hall, 763 pp.
- Benn, D.I., and Evans, D.J.A. 1998. *Glaciers and glaciation*. Arnold, London, UK, 734 pp.

- Bennet, M., Glasser, N. 2009. Glacial geology: ice sheets and landforms. Second edition. Wiley-Blackwell, Oxford. 385 pp.
- Best, J., Kostaschuk, R.A., Peakall, J., Villard, P.V., and Franklin, M. 2005. Whole flow field dynamics and velocity pulsing within natural sediment-laden underflows. *Geology*, 33: 765-768.
- Bhutiyani, M.R. 2000. Sediment load characteristics of a proglacial stream of Siachen Glacier and the erosion rate in Nubra valley in the Karakoram Himalayas, India. *Journal of Hydrology*, 227: 84-92.
- Boehrer, B., and Schultze, M. 2008. Stratification of Lakes. *Reviews of Geophysics*, 46: 1-27.
- Bogen, J. 1996. Erosion rates and sediment yields of glaciers. *Annals of Glaciology* 22:48-52.
- Bovis, M.J., and Jakob, M. 2000. The July 29, 1998, debris flow and landslide dam at Capricorn Creek, Mount Meager Volcanic Complex, southern Coast Mountains, British Columbia. *Canadian Journal of Earth Science*, 37: 1321-1334.
- British Columbia Ministry of Forests, Lands, and Natural Resource Operations. 2015. Progress made on Elaho and Boulder Creek wildfires. Available online: https://archive.news.gov.bc.ca/releases/news_releases_2013-2017/2015FLNR0217-001219.htm [Accessed: 23 December 2018].
- Chikita, K.A. 1989. A field study on turbidity currents initiated from spring runoffs. *Water Resources Research*, 25: 257-271.

- Chikita, K.A., Smith, N.D., Yonemitsu, N., and Perez-Arlucea, M. 1996. Dynamics of sediment-laden underflows passing over a subaqueous sill: glacier-fed Peyto Lake, Alberta, Canada. *Sedimentology*, 43: 865-875.
- Chough, S.K., and Hesse, R. 1976. Submarine meandering thalweg and turbidity currents flowing for 4,000 km in the northwest Atlantic mid-ocean channel, Labrador Sea. *Geology*, 4: 529-533. DOI: 10.1130/0091-7613(1976)4<529:SMTATC>2.0.CO;2
- Collins, D.N. 1979. Sediment concentration in melt waters as an indicator of erosion processes beneath an alpine glacier. *Journal of Glaciology*, 23: 247-257.
- Comeau, L.E.L., Pietroniro, A., and Demuth, M.N. 2009. Glacier contribution to the North and South Saskatchewan Rivers. *Hydrological Processes*, 23: 2640-2653.
- Crookshanks, S. 2008. High-energy sedimentary processes in Kluane Lake, Yukon Territory. M.Sc. thesis, Department of Geography, Queen's University, Kingston, Ontario.
- Crookshanks, S., and Gilbert, R. 2008. Continuous, diurnally fluctuating turbidity currents in Kluane Lake, Yukon Territory. *Canadian Journal of Earth Sciences*, 45: 1123-1138.
- Cuffey, K.M. and Patterson, W.S.B. 2010. *The physics of glaciers*. Fourth Edition. Butterwoth-Heinemann, Burlington, MA. 693 pp.
- De Cesare, G., Boilat, J.L., and Schleiss, A.J. 2006. Circulation in stratified lakes due to flood-induced turbidity currents. *Journal of Environmental Engineering*, 132: 1508-1517.

- Desloges, J.R. 1994. Varve deposition and the sediment yield record at three small lakes of the Southern Canadian cordillera. *Arctic and Alpine Research*, 26: 130-140.
- Desloges, J.R., and Gilbert, R. 1994. Sediment source and hydroclimatic inferences from glacial lake sediments: the proglacial sedimentary record of Lillooet Lake British Columbia. *Journal of Hydrology*, 159: 375-393.
- Eaton, B., and Moore, R.D. 2010. Chapter 4: Regional Hydrology. In: Pike, R.G., T.E. Redding, R.D. Moore, R.D. Winker and K.D. Bladon (editors). 2010. *Compendium of forest hydrology and geomorphology in British Columbia*. B.C. Min. For. Range, For. Sci. Prog., Victoria, B.C. and FORREX Forum for Research and Extension in Natural Resources, Kamloops, B.C. Land Manag. Handb. 66.
https://www.for.gov.bc.ca/hfd/pubs/docs/lmh/Lmh66/LMH66_ch04.pdf
- Fer, I., Lemmin, U., and Thorpe, S.A. 2001. Cascading of water down the sloping sides of a deep lake in winter. *Geophysical Research Letters*, 28: 2093-2096.
- Ferrer-Boix, C., Martín-Vide, J.P., and Parker, G. 2015. Sorting of a sand-gravel mixture in a Gilbert-type delta. *Sedimentology*, 62: 1446-1465.
- Folk, R.L. 1980. *Petrology of Sedimentary Rocks*. Hemphill Publishing Company, Austin. 184 pp.
- Francalanci, S., Paris, E., and Solari, L. 2013. A combined sampling-modelling approach for computing sediment transport during flash floods in a gravel-bed stream. *Water Resources Research*, 49: 6642-6655.

French HM, Slaymaker O. 1993. Canada's Cold Environments. McGill-Queen's Press.
368 pp.

Friele, P.A., and Clague, J.J. 2004. Large Holocene landslides from Pylon Peak,
southwestern British Columbia. *Canadian Journal of Earth Science*, 41: 165-182.
DOI: 10.1139/E03-089.

Gilbert, R. 1973. Observation of lacustrine sedimentation at Lillooet Lake, British
Columbia. Ph.D. Thesis, Department of Geography, University of British
Columbia, Vancouver, British Columbia.

Gilbert, R. 1975. Sedimentation in Lillooet Lake, British Columbia. *Canadian Journal of
Earth Sciences*, 12: 1697-1711.

Gilbert, R., and Butler, R.D. 2004. The physical limnology and sedimentology of
Meziadin Lake, Northern British Columbia, Canada. *Arctic, Antarctic, and Alpine
Research*, 36: 33-41.

Gilbert, R., Crookshanks, S., Hodder, K.R., Spagnol, J., and Stull, R.B. 2006. The record
of an extreme flood in the sediments of montane Lillooet Lake, British Columbia:
implications for paleoenvironmental assessment. *Journal of Paleolimnology*, 35:
737-745. DOI: 10.1007/s10933-005-5152-8.

Gilbert, R.G. and Shaw, J. 1981. Sedimentation in proglacial Sunwapta Lake, Alberta.
Canadian
Journal of Earth Sciences, 18: 81-93.

Gill, A. 1982. *Atmosphere-Ocean Dynamics*. Academic Press, New York. 662 pp.

- Gippel, C.J. 1989. The use of turbidimeters in suspended sediment research. *Hydrobiologia*, 176/177: 465-480.
- Guthrie, R.H., Friele, P., Allstadt, K., Roberts, N., S.G. Evans, Delaney, K.B., Roche, D., Clague, J.J., and Jakob, M. 2012. The 6 August 2010 Mount Meager rock slide-debris flow, Coast Mountains, British Columbia: characteristics, dynamics, and implications for hazard and risk assessment. *Natural Hazards Earth System Science*, 12: 1277-1294.
- Hammer, Ø., Harper, D.A.T., and P. D. Ryan, 2001. PAST: Paleontological Statistics Software Package for Education and Data Analysis. *Palaeontologia Electronica* 4(1): 9pp.
- Hay, A.E. 1987. Turbidity currents and submarine channel formation in Rupert Inlet, British Columbia: 1. Surge Observations. *Journal of Geophysical Research*, 92: 2875-2881.
- Heideman, M. 2013. Flood Hazard and Risk in Lillooet River Valley, British Columbia, Canada. Ph.D. Thesis, Department of Earth Sciences, Simon Fraser University, Burnaby, British Columbia.
- Heideman, M., Menounos, B., and Clague, J.J. 2015. An 825-year long varve record from Lillooet Lake, British Columbia, and its potential as a flood proxy. *Quaternary Science Reviews*, 126: 158-174. Available from: <http://dx.doi.org/10.1016/j.quascirev.2015.08.017>.
- Hock, R. 2005. Glacier melt: a review of processes and their modelling. *Progress in Physical Geography*, 29: 362-391.

- Hodder, K.R. 2009. Flocculation: a key process in the sediment flux of a large, glacier-fed lake. *Earth Surface Processes and Landforms*, 34: 1151-1163.
- Hodder, K.R., Gilbert, R., and Desloges, J. 2007. Glaciolacustrine varved sediment as an alpine hydroclimatic proxy. *Journal of Paleolimnology*, 38: 365-394.
- Johnson, R.C. 1992. Towards the design of a strategy for sampling suspended sediments in small headwater catchments. *Erosion and Sediment Transport Monitoring Programmes in River Basin in Proceedings of the Oslo Symposium, August 1992*, IAHS Publ. no. 210. 225-232.
- Jordan, P., and Slaymaker, O. 1991. Holocene sediment production in Lillooet River basin, British Columbia: A sediment budget approach. *Geographie Physique et Quaternaire*, 45: 45-57. DOI: 10.7202/032844ar.
- Klein, H.M. 1984. Anti-clockwise hysteresis in suspended sediment concentration during individual storms: Holbeck Catchment; Yorkshire, England. *Catena*, 11: 251-257. 10.1016/0341-8162(84)90014-6.
- Kleinhans, M.G. 2005. Grain-size sorting in grainflows at the lee side of deltas. *Sedimentology*, 52: 291-311. DOI: 10.1111/j.1365-3091.2005.00698.x
- Kneller, B., and Buckee, C. 2000. The structure and fluid mechanics of turbidity currents: a review of some recent studies and their geological implications. *Sedimentology*, 47: 62-94.

- Kopp, G., and Lean, J.L. 2011. A new, lower value of total solar irradiance: Evidence and climate significance. *Geophysical Research Letters*, 38, L01706: 1-7. DOI: 10.1029/2010GL045777
- Kostaschuk, R., Best, J., Villard, P., Peakall, J., and Franklin, M. 2005. Measuring flow velocity and sediment transport with an acoustic Doppler current profiler. *Geomorphology*, 68: 25-37.
- Lamb, M.P., and Mohrig, D. 2009. Do hyperpycnal-flow deposits record river-flood dynamics? *Geology*, 37: 1067-1070.
- Lamb, M.P., McElroy, B., Kopriva, B., Shaw, J., and Mohrig, D. 2010. Linking river-flood dynamics to hyperpycnal-plume deposits: Experiments, theory, and geological implications. *GSA Bulletin*, 122: 1389-1400. DOI: 10.1130/B30125.1.
- Lambert, A. and Giovanoli, F. 1988. Records of riverborne turbidity currents and indications of slope failures in the Rhone delta of Lake Geneva. *Limnology and Oceanography*, 33:458-468.
- Lambert, A.M., Kelts, K.R., Marshall, N.F. 1976. Measurements of density underflows from Walensee, Switzerland. *Sedimentology*, 87-105.
- Landers, M.N., and Sturm, T.W. 2013. Hysteresis in suspended sediment to turbidity relations due to changing particle size distributions. *Water Resources Research*, 49: 5487-5500. DOI: 10.1002/wrcr.20394.

- Lawler, D.M., Petts, G.E., Foster, I.D.L., and Harper, S. 2006. Turbidity dynamics during spring storm events in an urban headwater river system: The Upper Tame, West Midlands, UK. *Science of the Total Environment*, 360: 109-126.
- Lee, H-Y., and Yu, W-S. 1997. Experimental study of reservoir turbidity current. *Journal of Hydraulic Engineering*, 123: 520-528.
- Leeder, M.R. 2011. *Sedimentology and Sedimentary Basins: from Turbulence to Tectonics*. Blackwell Science, Oxford. 768 pp.
- Lewis EL. 1980. The Practical Salinity Scale 1978 and its antecedents. *IEEE Journal of Oceanic Engineering* OE-5(1):3-8.
- Lewis, W.M. 1983. A revised classification of lakes based on mixing. *Canadian Journal of Fisheries and Aquatic Sciences*, 40: 1779-1787.
- Mao, L., and Carrillo, R. 2017. Temporal dynamics of suspended sediment transport in a glacierized Andean basin. *Geomorphology*, 287: 116-125.
- Meteorological Survey of Canada. Archived Meteorological Data.
<<http://climate.weather.gc.ca/>>. Last accessed 23 December 2018.
- Middleton, G.V. 1993. Sediment deposition from turbidity currents. *Annual Review of Earth Planet Science*, 21: 89-114.
- Mulder, T., and Alexander, J. 2001. The physical character of subaqueous sedimentary density flows and their deposits. *Sedimentology*, 48: 269-299.
- Normark, W.R., and Dickson, F.H. 1976. Man-made turbidity currents in Lake Superior. *Sedimentology*, 23: 815-831.

- Ross, J., and Gilbert, R. 1999. Lacustrine sedimentation in a monsoon environment: the record from Phewa Tal, middle mountain region of Nepal. *Geomorphology*, 27: 307-323.
- Sawada, M., and Johnson, P.G. 2000. Hydrometeorology, suspended sediment and conductivity in a large glacierized basin, Slims River, Yukon Territory, Canada. *Arctic*, 53: 101-117.
- Schemel, L.E. 2001. Simplified conversions between specific conductance and salinity units for use with data from monitoring stations. *IEP Newsletter*, 14, 17–18.
- Schiefer, E., and Gilbert, R. 2008. Proglacial sediment trapping in recently formed Silt Lake, Upper Lillooet Valley, Coast Mountains, British Columbia. *Earth Surface Processes and Landforms*, 33: 1542-1556. DOI: 10.1002/esp.1625.
- Schiefer, E., Menounos, B., and Slaymaker, O. 2006. Extreme sediment delivery events recorded in the contemporary sediment record of a montane lake, southern Coast Mountains, British Columbia. *Canadian Journal of Earth Sciences*, 43: 1777-1790. DOI: 10.1139/E06-056.
- Simpson, J.E. 1997. *Gravity currents in the environment and laboratory*. Second Edition. Cambridge University Press. Cambridge, UK. 244 pp.
- Slaymaker, O., Clague, J.J., Gilbert, R., Friele, P.A., Jordan, P., Menounos, B., Schiefer, E. 2017. Lillooet-Harrison drainage basin: variable landscapes within the Coast Mountains. In: *Landscapes and Landforms of Western Canada, World Geomorphological Landscapes*. Slaymaker, O. (Ed.) Springer International Publishing, Cham, 303-320.

- Smith, N.D. 1978. Sedimentation processes and patterns in a glacier-fed lake with low sediment input. *Canadian Journal of Earth Science*, 15: 741-756.
- Smith, N.D., Vendl, M.A, Kennedy, S.K. 1980. Comparison of sedimentation regimes in four glacier-fed lakes of western Alberta. In: *Research in Glacial, Glacio-Fluvial, and Glacio-Lacustrine Systems*. Edited by R Davidson-Arnott, W. Nickling, B.D. Fahey. In *Proceedings of the 6th Guelph Symposium on Geomorphology*, 1980. 203-238 pp.
- Straub, K. 2007. Quantifying turbidity current interactions with topography. Ph.D. Thesis, Department of Earth, Atmospheric and Planetary Science, Massachusetts Institute of Technology. Cambridge, Massachusetts.
- Torrence, C. & G.P. Compo. 1998. A practical guide to wavelet analysis. *Bulletin of the American Meteorological Society* 79:61-78.
- Walling, D., and Webb, B. 1982. Sediment availability and the prediction of storm-period sediment yields. *IAHS-AISH Publication*, 137: 327-337.
- Walling, D.E., and Webb, B.W. 1981. The reliability of suspended sediment load data. *Erosion and Sediment Transport Measurement in Proceedings of the Florence Symposium*, June 1981, IAHS Publ. no. 133.
- Walling, D.E., Owens, P.N., Waterfall, B.D., Leeks, G.J.L, Wass, P.D. 2000. The particle size characteristics of fluvial suspended sediment in the Humber and Tweed catchments, UK. *The Science of the Total Environment*, 251/252: 205-222.

Water Survey of Canada. Archived Hydrometric Data. <<https://wateroffice.ec.gc.ca/>>.

Last accessed 23 December 2018.

Weatherly, H., and Jakob, M. 2014. Geomorphic response of Lillooet River, British Columbia, to meander cutoffs and base level lowering. *Geomorphology*, 217: 48-60.

Weirich, F.H. 1985. Sediment budget for a high energy glacial lake. *Geografiska Annaler*, 67A: 83-99.

Wells, M.G. 2007. Influence of Coriolis forces on turbidity currents and sediment deposition. In *Particle Laden Flow: From Geophysical to Kolmogorov Scales*. Edited by B.J. Geurts, H. Clercx, and W. Uijtewaal. In *Proceedings of the EUROMECH colloquium on particle-laden flow held at the University of Twente*. 331-343 pp.

Wetzel, R.G. 2011. *Limnology: lake and river ecosystems*. Third edition. Elsevier Academic Press. 1006 pp.

Willis, I.C., Richards, K.S., Sharp, M.J. (1996). Links between proglacial stream suspended sediment dynamics, glacier hydrology and glacier motion at Midtdalsbreen, Norway. *Hydrological Processes*, 10: 629-648.

Wiseman, W.M.J., Wright, L.D., Rouse, L.J., Coleman, J.M. (1976). Periodic phenomena at the mouth of the Mississippi River. In: *Contribution in Marine Science*, Volume 20. Wohlschlag, D.E. (Ed.) The Port Aransas Marine Laboratory, University of Texas, 11-3.

